UNIVERSITÀ DEGLI STUDI DI MILANO BICOCCA

SCUOLA DI DOTTORATO
UNIVERSITÀ DEGLI STUDI DI MILANO-BICOCCA

Dipartimento di
Scienza dei Materiali

Dottorato di Ricerca in Scienza e Nanotecnologia dei Materiali Ciclo XXX

Curriculum in Scienza dei Materiali

STRAIN-DEPENDENT SPIN PHENOMENA IN GE-BASED LOW DIMENSIONAL STRUCTURES

Cognome VITIELLO Nome ELISA

Matricola 725941

Tutore: PROF. EMANUELE GRILLI

Supervisor: DOTT. FABIO PEZZOLI

Coordinatore: PROF. MARCO BERNASCONI

ANNO ACCADEMICO 2016/2017

To Stefano

Table of contents

1 Introduction **7**

2 Bulk Germanium **11**

2.1 Structural properties 11
2.2 Optical properties of bulk Ge 13
2.3 Spin properties of bulk Ge 15
2.4 Optical spin orientation 19
2.4.1 Spin-selection rules for the indirect transition 22

3 Band Structure Engineering **25**

3.1 Strain 25
3.1.1 Strain engineering 28
3.1.2 Ge epitaxially grown on Si 30
3.1.3 Optical properties of strained Ge 33
3.1.4 Spin properties of strained Ge 34
3.2 Quantum Confinement 35
3.2.1 SiGe alloys 36
3.2.2 Band Alignment 37
3.2.3 Spin properties of Ge QWs 39

4 Germanium on Silicon **41**

4.1 Sample structure 41
4.2 Optical properties of Ge-on-Si 43
4.3 Spin properties of Ge-on-Si 44
4.3.1 Tight-binding calculations 46
4.3.2 Doping effect on spin polarization 49
4.3.3 Temperature effect on spin polarization 52

5 Ge/SiGe Quantum Wells **57**

5.1 Heterostructure and band alignment 60
5.2 Optical properties 62
5.3 Spin properties of Ge/SiGe MQWs 66
5.3.1 Polarized-resolved CWPL 66
5.3.2 Spin-relaxation time by polarized-resolved TRPL . . . 67
5.4 Comparison between ESR and TRPL 71

5.4.1 g factor of conduction electron in Ge/SiGe QWs 75

6 Conclusions **79**

Appendices

A Methods **83**

A.1 Continuous-wave PL 83

A.1.1 InGaAs array line 85

A.1.2 Single-channel extended InGaAs line 85

A.2 Time-resolved PL 86

A.3 ESR technique 88

A.3.1 Spin-relaxation time 90

B Samples **93**

B.1 Low Energy Plasma Enhanced CVD 93

B.2 Ge-on-Si 94

B.3 Ge/SiGe MQWs 95

C Stokes analysis **97**

Acknowledgments **103**

Bibliography **105**

1 Introduction

Strain offers an effective degree of freedom for tailoring the band structure of semiconductor materials, opening up to interesting physical phenomena and advanced application perspectives [1, 2]. In an era of rapidly changing technology, strain is a relatively old topic in semiconductor physics, yet its tangible effects on the band structure and carrier transport have spurred a renewed interest [3]. The controlled application of strain in crystalline semiconductors can be used to modify their basic physical properties, eventually enhancing the performance of devices. The underlying idea is that the electronic band structure of a semiconductor crystal, which determines its key measurable properties, depends not only on the chemical nature of the constituent atoms but also on their spatial arrangement, which in turn is directly modified by the presence of strain. Strain can be used to lift degeneracies in the band structure at high symmetry points of reciprocal space, thereby suppressing intervalley and interband scattering. Indeed, the modification of the energy band curvature changes the effective masses, which are relevant to electronic transport. These ideas have already been widely applied to group-IV semiconductors (including Si as well as Ge and SiGe) to produce significant carrier mobility enhancements, leading to improved performances in metal oxide semiconductor field effect transistors (MOSFET) [4, 5].

Moreover, strain effects on the band structure offer great potential for enhancing the performance of photonic and optoelectronic devices, *e.g.*, by modifying wavelength, gain, linewidth and quantum efficiency of the emission. In optoelectronics, Ge is already a well-established photodetector material used for on-chip data distribution [6], thanks to its strong interband absorption at near-infrared optical communication wavelengths and to its direct compatibility with the Si microelectronic platform [7]. Additional applications within the emerging field of group-IV photonics, including

light emitters [8] and lasers [9] are also under wide investigation.

Particularly remarkable for Ge, an indirect-band gap semiconductor with conduction band four-degenerate minima at the L points, is that strain can also be used to modify the nature of its fundamental energy band gap. As a result, through application of tensile strain, the local conduction band minimum, which exists at the Γ point, can be lowered in energy relative to the L valleys, until, at about 2% biaxial strain, Ge becomes a direct-band gap material [10]. This modification leads to a dramatic change in the optical radiative properties, by increasing the interband radiative efficiency and allowing population inversion and optical gain [11–13]. In germanium, tensile strain can be conveniently obtained *via* epitaxial growth of a Ge layer on Si, spontaneously induced in the epitaxial layer thanks to the difference in the thermal expansion coefficients between Ge and the Si substrate. This strain, albeit very small, *i.e.* 0.2%, is nevertheless useful: various Ge-based LEDs and photodiodes were successfully fabricated on Si [14–17], eventually achieving optically [9], as well as electrically [18] stimulated lasing action. Despite such advances, several questions remain unanswered, such as the impact of non-radiative recombination on carrier dynamics and optical gain [19].

Beside its applications in photonics, Ge might have a unique potential also in the field of spintronics [20]. The main goal of spintronics is to encode digital data in the electron spin, eventually overcoming the limitations of conventional charge-based electronics in terms of power consumption and processing speed, while preserving the large-scale and cost-effective production offered by the microelectronic foundries [21]. With this aim, research effort in spintronics has been focused on materials which possess highly desired features, such as long spin lifetimes and large diffusion lengths.

As group-IV material, Ge centrosymmetric crystal structure guarantees intrinsically long spin lifetimes, as it prevents spin relaxation due to the Dyakonov-Perel mechanism. The latter is important in the direct gap III-V systems [22, 23]. In addition, the natural abundance of zero-spin nuclear isotopes further reduces hyperfine interactions and lengthens the spin coherence time [24]. As opposed to Si, the pseudo direct-gap behaviour of Ge offers also the unique possibility to efficiently orient spin polarized carriers by the absorption of circularly polarized light through the direct-gap transition. By exploiting the coupling between the angular momentum of circularly polarized photons and the electronic spin state, the polarization of the emitted luminescence can be used to gather information about the physical mechanisms governing non-equilibrium spin dynamics. The multivalley conduction band (CB) of Ge [25] and the sizeable spin-orbit interaction [26] thus offer non-trivial and intriguing spin physics. The mentioned properties, together with the feasible monolithic integration in the microelectronic technology, recently put forward the potential of Ge in bridging the

gap between spintronic concepts and semiconductor device physics.

In the context of spin physics, strain can be exploited to lift degeneracies in the band structure, thus modifying relaxation mechanisms and spin lifetimes [23, 27, 28]. In particular, the zone-center removal of light- and heavy-hole valence band degeneracy can significantly improve the generation of non-equilibrium spin populations *via* optical orientation [23]. The transfer of photon angular momentum to a material near the limit of complete spin polarization has been indeed demonstrated in strained III-V semiconductors, achieved through resonant absorption of circularly polarized light at an excitation energy that matches the fundamental strain-split transition [23, 29], but a similar demonstration is still missing for group-IV materials.

The present work is a fundamental study about spin properties of electrons in strained Ge heterostructures, with the aim of understanding the effect of strain on carrier and spin kinetics. This is of both fundamental interest and central importance for applications in spintronics and photonics. In particular, we employ polarization-resolved photoluminescence (PL) to investigate the spin physics of Ge-based systems. One of the main advantages of this all-optical technique is to avoid spin depolarization arising from interfaces between ferromagnetic and semiconductor materials, which affects electrical measurements and the determination of the intrinsic spin lifetime [30]. In this thesis we focus on the optical generation of spin polarized carriers and on the PL polarization of two notable systems. First, we exploit strain effects on the PL polarization of the direct-gap emission in tensile strained Ge layers epitaxially grown on Si substrates. Then we focus on the PL polarization decay of the indirect emission in compressively strained Ge quantum wells embedded in Ge-rich $Si_{1-x}Ge_x$ barriers. In this way, we provide a direct measurement of the spin lifetime in this heterostructure.

The work is organized as follows: in Chapter 2 we report the properties of bulk Ge, underling its key features for possible implementation and convergence of spintronics and photonics concepts on the microelectronics platform. Then we present the physical principles behind the spin optical orientation technique, pointing out the potential of this tool to study spin relaxation mechanism in semiconductors. In particular, we linger on spin selection rules for both direct [23] and indirect transitions [28], highlighting the rich spin and carrier dynamics offered by the multivalley nature of the CB in Ge. In Chapter 3, we address the effects of strain on optical and spin properties in Ge, reporting also the main research efforts in strain engineering of Ge for photonic applications. In particular, we discuss the thermal-induced tensile strain in Ge epitaxially growth on Si substrates, whose spin properties are addressed in Chapter 4. A further Section in Chapter 3 is devoted to a thorough description of the effects of quantum confinement on Ge properties. Ge/SiGe multiple quantum wells (MQWs)

heterostructures have been demonstrated to provide the possibility to tailor the optical transition energies by means of both confinement and strain induced by epitaxial growth [31, 32]. We first provide details about the SiGe alloys, namely structural properties and band structure, then we discuss Ge/SiGe MQWs band alignments as a function of alloy concentrations. Finally, we linger on the effect of strain, confinement and band alignment on the Ge/SiGe spin properties.

The fourth Chapter is devoted to the spin properties of tensile-strained Ge epitaxially growth on Si (Ge-on-Si). After briefly presenting its optical properties, we focus on polarized emission of direct recombination, addressed by means of polarization-resolved continuous-wave PL (CWPL). Data on the polarization of the direct-gap emission from low to room temperature for samples with different dopant content are presented. In particular, we are able to resolve the radiative recombinations involving strain-split transitions, thanks to the different spin-dependent optical selection rules [33]. By combining our experimental results with tight-binding calculations, we provide a description of electron spin dynamics in Ge CB under tensile strain.

In Chapter 5, we focus on the spin properties of Ge/SiGe MQWs heterostructures. In particular, polarization-resolved CWPL and time-resolved PL (TRPL) is exploited to experimentally evaluate the spin relaxation time T_1. In particular, by measuring T_1 as a function of the photoinjected carrier density, we address the role of electron-hole exchange interaction mechanism in determining spin relaxation in Ge quantum structures [34]. In the last part of Chapter 5, we compare our results with electron spin resonance (ESR) data of conduction electrons in Ge MQWs [34]. Moreover, we present ESR results on the Landé g-factor of CB electrons and its dependence on the well width [34].

In the Conclusions, the main results reported in this thesis is summarized. In the Appendix, we describe the experimental set-ups, the samples growth technique, and the light polarization analysis technique used in Chapter 4.

2 Bulk Germanium

2.1 Structural properties

Ge is a group IV material with a diamond-like structure, which consists of two interpenetrating face-centred cubic Bravais lattices, displaced along the diagonal of the cubic cell by one quarter of the length of the same diagonal. The two atoms of the basis occupy respectively the (0,0,0) and ($a/4, a/4, a/4$) positions, where a is the lattice parameter of the cubic cell. At room temperature (RT), a = 0.566 nm [35]. The cubic unit cell contains eight atoms and each atom is bounded to four nearest neighbours in a regular tetrahedron, as sketched in Figure 2.1a.

Ge is a semiconductor with an indirect band-gap, as shown in Figure 2.1b. The top of the valence band (VB) is located at the centre of the first Brillouin (FB) zone in the reciprocal space (Γ-point). The four-fold degenerate absolute minima in the conduction band (CB) are located at the edges of the FB zone along the <111> direction, namely L-point, at the energy of 0.662 eV above the top of the VB at RT. The CB has other relative minima, which are at the Γ-point and along the <001> directions (Δ valleys), higher in energy by about 136 meV and 200 meV at RT with respect to the L-point absolute minima, respectively [36].

The temperature dependence of the bandgaps follows the behaviour described by the Varshni's law [37]:

$$E(T) = E(0) - \frac{\alpha T^2}{\beta + T} \tag{2.1}$$

where the E(0), α and β values for direct gap (E_Γ) and indirect gaps ($E_L = E_g$ and E_Δ) are reported in Table 2.1. In particular, by increasing the temperature, the indirect and direct bandgaps shift to lower energies.

This multivalley nature of the CB of Ge provides a non-trivial dynamics of conduc-

Bandgap	E(0) (eV)	α (10^{-4} eV/K)	β (K)
$E_L = E_g$	0.744	4.774	235
E_Γ	0.892	7.25	433
E_Δ	1.105	4.730	636

Table 2.1: Varshni's parameters in Equation 2.1 for fundamental indirect gap E_L (E_g) and relative gap in Δ and Γ valleys (E_Δ and E_Γ) in Ge [38].

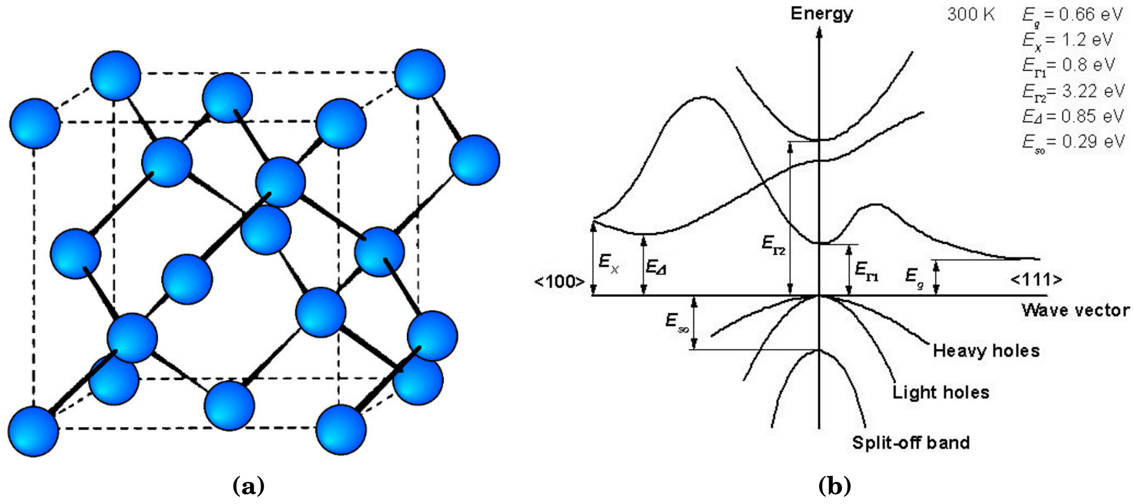

Figure 2.1: Diamond-like crystal structure (a) and band structure (b) of Ge.

tion carriers which is the root of the intriguing properties of Ge, as is described in the following Sections.

The top of the VB originates from *p*-like orbitals, with angular momentum L=1. This results in a total angular momentum $J = L + S = \frac{3}{2}$, where S is the spin momentum. Hole bands are split into heavy (HH) and light holes (LH) bands (with $J = \frac{3}{2}$) and a split-off band (SO) with $J = \frac{1}{2}$. HH and LH bands are degenerate in the Γ-point and have two different curvatures: HH has larger effective mass with respect to LH, and consequently a smaller curvature, as illustrated in Figure 2.1b. In Ge, the energy separation between the SO band and the topmost HH and LH bands is of about Δ_{SO} = 296 meV at the Γ-point [39]. This separation is higher than the splitting in Si (Δ_{SO} = 44 meV), thanks to the stronger spin-orbit interaction in Ge due to the heavier atomic mass [40].

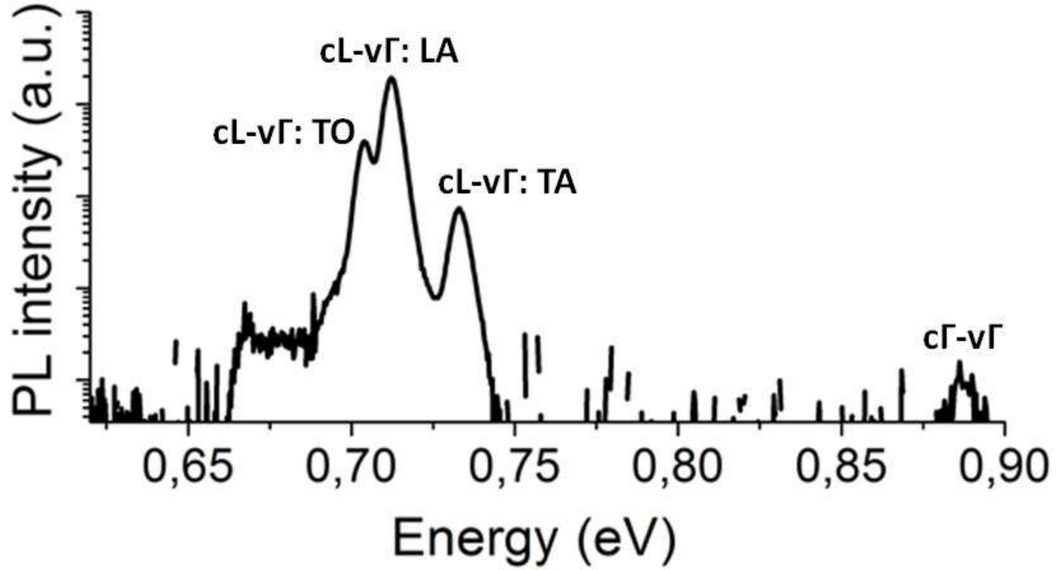

Figure 2.2: PL spectrum obtained from a nominally intrinsic bulk Ge sample measured at T=4 K under 1.165 eV laser excitation with a power density of about 4.5 kW/cm^2. Phonon mediated indirect ($cL - v\Gamma$) and direct ($c\Gamma - v\Gamma$) transitions are shown [42].

2.2 Optical properties of bulk Ge

The optical properties of bulk Ge, in particular absorption and emission of photons *via* photoluminescence (PL), are described in this section.

Upon optical excitation, a photon is absorbed by the crystal, thus creating an electron-hole pair, which can then radiatively recombine [41]. After excitation, the whole process leading to PL signal consists of carriers thermalization, diffusion and radiative recombination.

The PL spectrum of bulk Ge at the temperature of 4 K under 1.165 eV excitation is shown in Figure 2.2. The close proximity of the direct ($c\Gamma - v\Gamma$) and indirect ($cL - v\Gamma$) transitions, occurring at different photon energies, points out the Γ-to-L proximity which allows for Ge a remarkable quasidirect behaviour. With the excitation energy of 1.165 eV, which is larger than the energy difference between VB and CB at Γ (i .e. $\hbar\omega > E_\Gamma$), electrons (holes) are photogenerated near the Γ-point with an excess energy with respect to the CB minimum (VB maximum). The use of this near infrared excitation allowed us to exploit the large absorption coefficient of the direct gap interband transitions (10^4 cm^{-1}) [43].

In Ge, the lifetime of electrons excited within the Γ-valley, τ_Γ, is dominated by their ultrafast scattering towards satellite Δ- and L-valleys, lying in the regime of hundreds of femtoseconds [44, 45]. These energy relaxation *via* satellite valleys is the most efficient thermalization process from the Γ-valley [25], due to the weak deforma-

Transition	Transition energy (eV)	Phonon energy (meV)
$cL - v\Gamma : TA$	0.733	8
$cL - v\Gamma : LA$	0.712	28
$cL - v\Gamma : TO$	0.704	36

Table 2.2: Energies of the phonon mediated indirect $cL - v\Gamma$ transitions and of the <111> phonons in bulk Ge at T=4 K [46].

tion potential interaction between long-wavelength optical phonons and CB electrons. Moreover, in the doped samples, the energy relaxation of photoexcited electrons is governed by Coulomb collisions with the background carriers. This energy relaxation channel is effective in the Δ and L valleys but not in the Γ valley. This difference stems from the effective mass: when the photoexcited electron is in the Γ valley, its much smaller effective mass compared with the one of the background carrier renders the binary collision process ineffective in relaxing the photoexcited electron towards the bottom of the valley, and intervalley phonon-induced relaxation mechanisms become dominant [25]. The binary process is more effective in the L and Δ valleys where the effective masses are comparable with those of the background carriers. Most of the electrons will thus suffer scattering towards the absolute minimum of the L-valley, where they exhibit a long lifetime: τ_L values are expected to be between tens and hundreds of μs at RT [41]. The lifetime of electrons in the L valley is governed by non-radiative recombination channels across the indirect band gap [25].

Simultaneously with the thermalization process, the concentration gradient due to excitation causes carrier diffusion within the sample. In fact, immediately after absorption at normal incidence, the depth-dependent density of photogenerated carriers G(z) can be described by the Beer's law:

$$G(z) = [1 - R(\hbar\omega)] \cdot \alpha(\hbar\omega) \cdot I(0) \cdot e^{-\alpha(\hbar\omega)\cdot z} \tag{2.2}$$

where z is the coordinate normal to the sample surface, R($\hbar\omega$) is the surface reflectivity of the sample, I(0) is the incident photon density and $\alpha(\hbar\omega)$ is the absorption coefficient at the excitation energy. This gradient causes carrier spatial diffusion within the sample during the long lifetime in the L valleys and, thanks to the high carrier mobility [47], carriers can diffuse for hundreds of μm.

After thermalization and diffusion, electrons are distributed in the CB and only a small fraction of photoexcited carriers experiences radiative recombination *via* photon emission. The PL spectrum, which is due to the product between the joined density of states and the carrier population, represents the radiation intensity emitted by

the sample as a function of the energy. It is worth noting that the PL peak maxima intensity does not correspond to the band gap energy. In particular, the PL peak of the direct emission si blue-shifted by an amount of $\frac{1}{2}k_BT$ with respect the bandgap E_Γ [48].

In low temperature spectrum shown in Figure 2.2, the PL features related to indirect $cL - v\Gamma$ transition are found in the low energy range, between 0.65 eV and 0.75 eV. We observe that the $cL - v\Gamma$ transition is mainly mediated by three phonons [46], namely trasverse optical (TO), longitudinal and transverse acoustic (LA and TA) phonons. The phonon energies are reported in Table 2.2. At 0.662 eV, the spectra of all the samples show a structure about 500 times lower intensity with respect to the previous lines. Lieten et al. [46] attributed this feature to radiative recombination assisted by two phonons: a <111> LA phonon and a TO phonon at the Γ point of the Brillouin zone. The less intense PL peak related to the direct-gap emission is found at the high energy side of the spectrum, at about 0.88 eV (Figure 2.2).

2.3 Spin properties of bulk Ge

Spin physics in semiconductors has been widely investigated in the last century, with the aim to understand the physical principles underlying the generation, dynamics and transport of spin-polarized carriers [23].

Once the carriers are spin oriented, they interact with the environment usually through phonons [49], relaxing to the ground state by flipping their spin. The characteristic time for this process is called spin relaxation time T_1. Moreover, the interactions among carriers can influence the phase of their spins. The time in which spins loose information on its initial phase is called spin decoherence time T_2.

Four mechanisms for spin relaxation and dephasing of conduction electrons have been found relevant in semiconductors: (i) relaxation *via* ordinary momentum scattering [50, 51] (such as by phonons or impurities), *i.e.* the Elliott-Yafet mechanism; (ii) spin relaxation due to spin-orbit coupling in systems lacking inversion symmetry (Dyakonov-Perel mechanism) [52], (iii) through scattering by holes, accompanied by spin exchange, [53] in the Bir-Aronov-Pikus mechanism, which is effective in *p*-doped semiconductors, and (iv) the magnetic interaction between the magnetic moments of electrons and nuclei in hyperfine-interaction mechanisms [54].

Group IV semiconductors, such as Ge, are promising materials for spintronics because of the centrosymmetric crystal structure, which prevents the Dyakonov-Perel spin relaxation mechanism [23]. In addition, the natural abundance of spinless isotopes, listed in Table 2.3, and the possibility of isotopic refinement reduce the hyperfine

Isotopes	Percentage	Nuclear Spin
^{70}Ge	20.57%	0
^{72}Ge	27.45%	0
^{73}Ge	7.74%	9/2
^{74}Ge	36.50%	0
^{76}Ge	7.73%	0

Table 2.3: Natural abundance of Ge isotopes and their nuclear spin values [24].

interaction with nuclear spins [24], thus providing a longer electron spin lifetime (T_1) [42] and offering the clean environment required for spin transport.

The spin relaxation of conduction electrons in Ge is mainly driven by electron scattering due to Elliott-Yafet mechanism [51], and has been widely discussed from the theoretical point of view [49, 55]. Ref.[49, 55] demonstrate that both intervalley and intravalley electron scattering provide an important contribution to the spin relaxation in the multivalley CB of Ge. In particular, theory shows that the intrinsic spin relaxation is governed by the intervalley electron-phonon scattering over a wide temperature range (T > 30 K) [55]. This dominating mechanism involves shortwave phonon modes whose wavevector connects centers of different L valleys (*i.e.*, phonon modes along <001> direction, near the X-point) [22, 23]. Dominant contributions result from these phonons, characterized by an energy of about 30 meV [49].

In a work by Li *et al.* [49], it has been calculated that the electron-phonon interaction results in an extremely long conduction electron spin lifetime at low temperatures (about 10 ms at T=10 K). In this temperature regime, the population of the X-point phonon modes is negligible and, thus, the intravalley spin relaxation rate exceeds the intervalley one [49]. In Figure 2.3 we compare the main results reported in the literature. Empty (full) symbols are experimental data obtained by electrical (optical) methods, while the solid and the dashed lines represent the intrinsic value of T_1 calculated in Ref. [49] and Ref. [55], respectively. The latters refer to intrinsic relaxation mechanisms, as a function of the temperature, of electrons in the L valleys taking into account the depolarization effects due to electron-phonon scattering.

Electrical spin injection measurements [30, 56–58] provide values that are shorter than 1 ns over the whole temperature range, and their discrepancy with the theory at low temperature drastically diverges by several orders of magnitudes. This observation is in line with the argument that at low temperatures a rapid spin relaxation channel can be provided by scattering from ionized impurities in the heavily doped region of the device [30] as well as with the crossover from spin accumulation into interface states to spin injection into the CB [56]. In contrast to the electrical meth-

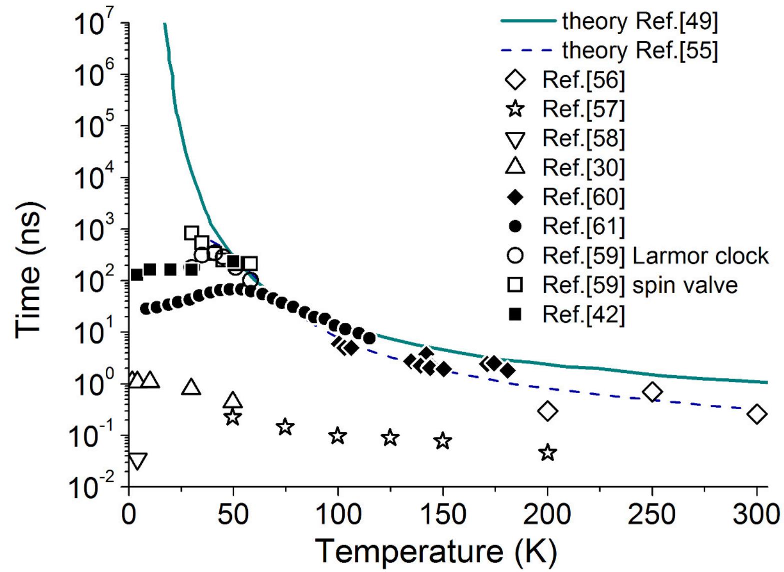

Figure 2.3: Electron spin lifetime as a function of the temperature [42]. Solid [49] and dashed [55] lines result from theory. Empty symbols are values obtained by electrical measurements [30, 56–59] and full symbols are values obtained by optical measurements.[42, 60, 61]

ods, optical-based techniques generally are less prone to measurements artefacts. The same applies to the transport data acquired under the ballistic regime, which do not rely on spin accumulation at the interfaces [59]. Indeed, above 50 K, T_1 is in the tens-of-ns range and the theory agrees well with the estimation of the spin relaxation provided by magneto-optical measurements (full symbols) [60, 61] and by hot electron devices (open circles and squares) [59].

Below 50 K, data obtained in Ref. [42] (black squares) show spin relaxation times are hundreds of ns long. Noticeably, in this temperature regime the results of Ref. [42] demonstrate an increase of almost one order of magnitude over the longest time previously reported by Faraday rotation experiments [61]. Nevertheless, T_1 is still far from the theoretical prediction [49]. The reasons for such discrepancy may be due to further spin relaxation mechanisms that play a significant role in the low temperature regime [42].

Another important characteristic of Ge is due to the heavier atomic mass, with respect to Si, which provides a larger spin-orbit coupling resulting in a highly anisotropic g factor [62]. This feature constitutes an efficient tool for the manipulation of the carrier spin.

In solids, the g factor deviates from the free electron value (g_e = 2.0023) due to spin-orbit interaction [26]. Theoretical investigations predicted in Ge a highly anisotropic g factor [62]. The reason of this is that the fundamental minima of the CB are at

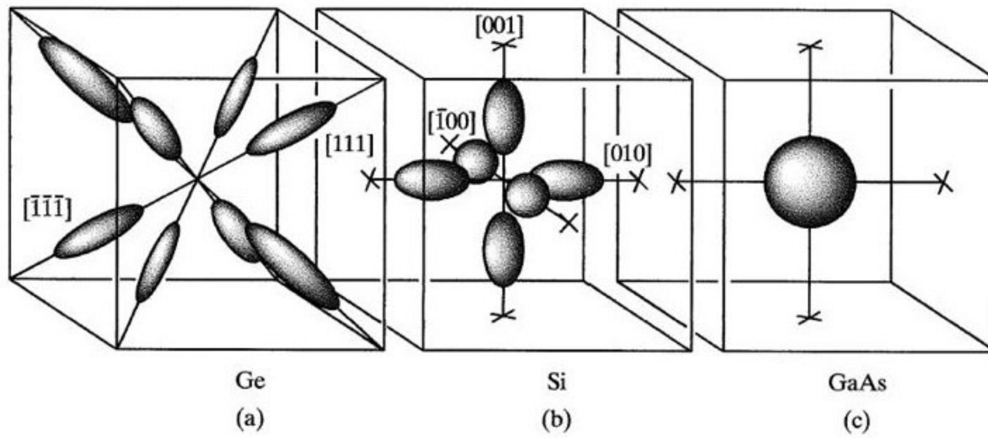

Figure 2.4: Constant energy surfaces of conduction band for (a) Ge, (b) Si and (c) GaAs [36].

the L points of the Brillouin zone, and their constant energy surfaces are ellipsoidal, as sketched in Figure 2.4a. In contrast, the CB minimum in Γ valley, like in III-V semiconductors, has a spherical shape as illustrated in Figure 2.4c, which results in isotropic g factor. Actually, also the fundamental minima of the Si CB, which lie in the Δ valleys are anisotropic, but the eccentricity of the ellipsoidal surfaces is much less pronounced, as shown in Figure 2.4b [63]. This ellipsoidal shape in Ge provides different longitudinal and transverse effective masses and it result in a highly anisotropic g-factor [63].

Finally, thanks to the quasi-direct behaviour, the Ge band structure provides an effective means [64] to overcome the shortcoming due to indirect nature of the bandgap, opening up the possibility to perform optical investigations of the spin properties also in group IV semiconductors. In particular, Ge offers the possibility to fully exploit the coupling between the angular momentum of circularly polarized photons and the electronic spin states. On one hand, carrier spins can be efficiently oriented by the absorption of circularly polarized light through the direct gap, and on the other hand, the polarization of the emitted photons provides information on the spin orientation of carriers when they recombine radiatively. Since the direct and the indirect gap recombination are characterized by different decay times, the detection of both emissions provides the possibility to investigate different time scale dynamics of the carrier spins. This technique, known as optical orientation of spin, is detailed in the following Section.

2.4 Optical spin orientation

Optical orientation of spin allows the generation of an unbalanced spin distribution within the semiconductor by means of absorption of circularly polarized light [65], which has angular momentum $L_z = \pm\hbar$ along the light propagation direction (from now define as z axis). Photons possessing momentum $m_p = +1$ (-1) are defined right- (left-) handed circularly polarized. In Ge, the absorption of these photons with energies above the direct bandgap generates a non-equilibrium distribution of spin-polarized carriers, which depends on the optical selection rules and the oscillator strength of the transitions at the Γ-point. The model used in the following to describe the polarized absorption process is schematically shown in Figure 2.5, and is valid for the Γ-point transitions in direct bandgap III-V compounds [23]. Giving that Ge behaves like a quasi direct-gap semiconductor [23], this model can be applied also to transitions at the Γ-point proximity in Ge. We assume now right-handed helicity (σ_+) of the exciting light ($m_p = +1$). From the selection rules in the electric dipole approximation, we get $\Delta m = m_{j_f} - m_{j_i} = 1$, where m_{j_i} and m_{j_f} represent the initial and final projection of the total angular momentum (J) of carriers along the light propagation direction (z), respectively. Under these conditions, the allowed transitions ($|J, m_{j_i}\rangle \longrightarrow |J, m_{j_f}\rangle$) is thus:

$$\begin{aligned} HH &: \left|\frac{3}{2}, -\frac{3}{2}\right\rangle \longrightarrow CB : \left|\frac{1}{2}, -\frac{1}{2}\right\rangle \\ LH &: \left|\frac{3}{2}, -\frac{1}{2}\right\rangle \longrightarrow CB : \left|\frac{1}{2}, \frac{1}{2}\right\rangle \\ SO &: \left|\frac{1}{2}, -\frac{3}{2}\right\rangle \longrightarrow CB : \left|\frac{1}{2}, \frac{1}{2}\right\rangle \end{aligned} \tag{2.3}$$

Therefore, immediately after light absorption, both photoexcited holes and electrons are spin polarized. As a result from Eq. 2.3, photoexcited electrons from the HH and LH states populate opposite spin sublevels in the CB, as schematically shown in Figure 2.5.

For $E_\Gamma \leq \hbar\omega < E_\Gamma + \Delta_{SO}$, only LH and HH sub-bands provide contributions to the absorption process, resulting in a net electron spin polarization defined as:

$$P_0 = \frac{n_\uparrow - n_\downarrow}{n_\uparrow + n_\downarrow} \tag{2.4}$$

where $n_\uparrow$ ($n_\downarrow$) stands for the density of electrons spin-up (down) polarized.

By calculating the square of the matrix elements for transitions involving HH and LH states, it results that the former is three times larger than the latter. Thus, un-

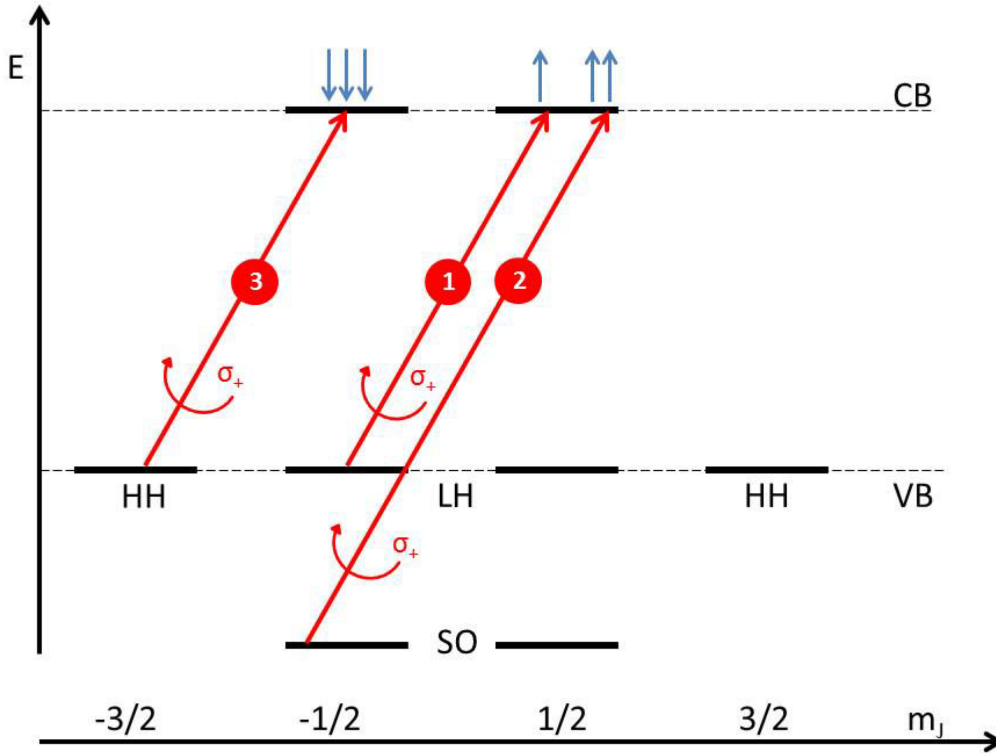

Figure 2.5: Schematic representation of states in valence (VB) and conduction band (CB) involved in the optical orientation process near the Γ-point. Along the y-axis the arbitrary energy scale (E), while along the x-axis the projection m_j of the total angular momentum J on the direction of light propagation z of heavy-hole (HH), light-hole (LH) and split-off band (SO). Arrows indicate the allowed transitions upon σ_+ laser excitation. The oscillator strength of the transitions are indicated in the circles.

der σ_+ excitation conditions, we have $n_\uparrow : n_\downarrow = 1:3$, and from Eq. 2.4 it follows that $P_0 = -\frac{1}{2}$. In this case, the net spin-polarization is oriented oppositely with respect to the light propagation direction. It is worth noting that, if we consider excitation energy involving also transitions from the SO band (i. e. $\hbar\omega \geq E_\Gamma + \Delta_{SO}$), the net electron spin polarization is null ($P_0 = 0$). Indeed, the square of the matrix element for SO transitions is two times larger than the one for transitions involving LH states.

In the recombination process, the PL circular polarization degree is defined as [66]:

$$\rho = \frac{I_+ - I_-}{I_+ + I_-} \tag{2.5}$$

where I_+ (I_-) represents the intensity of σ_+ (σ_-) polarized light. It is well known that, in bulk, the holes depolarization is very fast compared to the one of the electrons. A value of $T_1^{holes} \sim 1$ ps has been reported [67], hence the spin states of the VB are

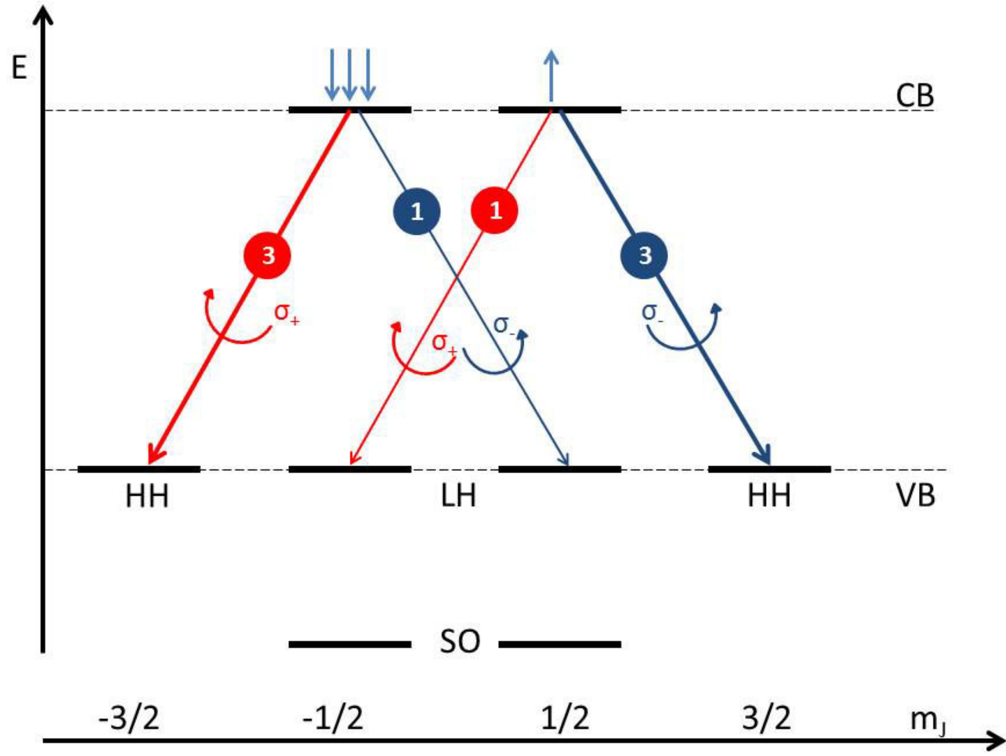

Figure 2.6: Schematic representation of states in valence (VB) and conduction band (CB) involved in the optical orientation process near the Γ-point. Along the y-axis the arbitrary energy scale (E), while along the x-axis the projection m_j of the total angular momentum J on the direction of light propagation z of heavy-hole (HH), light-hole (LH) and split-off band (SO) Thick (thin) arrows indicate the recombination of electrons in the CB with unpolarized holes in HH (LH) states. The oscillator strength for each transition is indicated in the circles.

equally occupied. In this case, only the spin polarization of electrons contributes to the polarization of the PL signal, as shown in Figure 2.6, and I_+ (I_-) only depends on the occupation of spin states in CB and on the relative transition probability. Thus, for $E_\Gamma \leq \hbar\omega < E_\Gamma + \Delta_{SO}$, from Eq. 2.5 we get:

$$\rho_0 = \frac{(n_\uparrow + 3n_\downarrow) - (3n_\uparrow + n_\downarrow)}{(n_\uparrow + 3n_\downarrow) + (3n_\uparrow + n_\downarrow)} \tag{2.6}$$

where ρ_0 indicates that we are not considering spin depolarization mechanisms. Thus, in bulk, a $E_\Gamma \leq \hbar\omega < E_\Gamma + \Delta_{SO}$ excitation, with an initial spin polarization in the CB of $P_0 = -\frac{1}{2}$, yields a polarization degree of the emitted light $\rho_0 = -\frac{1}{4}$.

It has to be considered, however, that in a semiconductor the photoexcited electrons and holes exist for a time τ before the recombination [23]. During this time, carriers can lose their spin orientation *via* different spin relaxation mechanisms. As a result,

the measurable PL polarization is [27]:

$$\rho = \frac{\rho_0}{1+\tau/T_1} \tag{2.7}$$

where τ and T_1 are the electron lifetime [48] and spin relaxation time [23], respectively.

As a consequence, also the non-equilibrium spin polarization is related to spin relaxation mechanisms [23]. From Eq. 2.7 we can derive the same relation for P:

$$P = \frac{P_0}{1+\tau/T_1} \tag{2.8}$$

The steady-state polarization is thus lower than the initial polarization P_0 by an amount depending on the ratio τ/T_1.

It should be noted that the optical orientation process described above is valid at the zone centre, where Ge mimics the behaviour of III-V compound semiconductors. The multi-valley nature of the Ge CB, however, allows carriers to experience intervalley scattering towards the Δ and L valleys. This property, together with the aforementioned pseudo-direct band structure of Ge, makes spin dynamics richer than in direct-gap III-V compounds.

2.4.1 Spin-selection rules for the indirect transition

In indirect gap semiconductors, optical transitions are mediated by electron-phonon interactions. This coupling mechanism has to be considered to properly describe the relation between the spin polarization of electrons and the circular polarization degree of the indirect transition luminescence [28, 68]. This can be done by taking into account the symmetry irreducible representation of all the states involved in the transitions [28, 68]. Phonon-assisted optical transitions in bulk Ge are shown in Figure 2.7a. The vertical arrows correspond to the radiation-matter interaction and the arrows between L and Γ correspond to the interaction of electrons with zone-edge phonons near the L point. according to group theory, the top edge of the valence band is two-fold degenerate and located in the zone centre (indicated by Γ_8^+). The bottom edge of the non-degenerate conduction band is indicated by L_6^+, and the Γ valley in CB is Γ_7^-.

A transition from an initial to a final state can proceed *via* several virtual paths. LA modes can be involved in the $L_6^+ \rightarrow \Gamma_7^- \rightarrow \Gamma_8^+$ optical transition (solid arrows in Fig. 2.7a). As shown in the PL spectrum of Fig. 2.2, one can also find a weak spectral peak from TA modes, in spite of the fact that edge-to-edge optical transitions with the TA mode are forbidden [28]. However, higher order transitions between states near

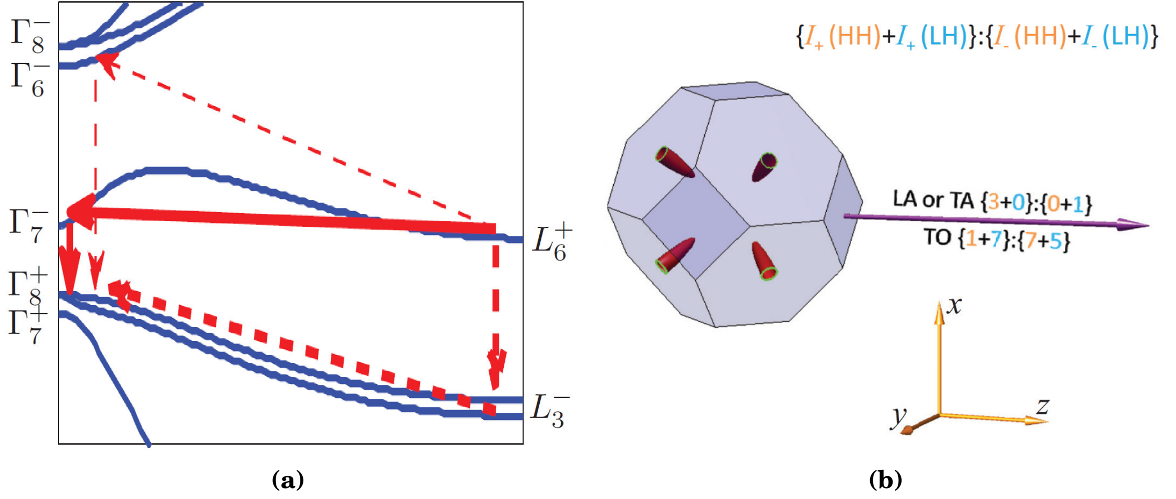

Figure 2.7: (a) Band structure of Ge along the $\Gamma-\Lambda-L$ symmetry axis. The conduction (valence) edge state is indicated by L_6^+ (Γ_8^+). Arrows represent virtual paths for phonon-assisted optical transitions *via* pertinent intermediate states. The path *via* Γ_7^- (L_3^-) is shown in bold solid (dash) lines to represent its dominant role in setting the intensity of LA (TO) phonon-assisted optical transitions. (b) Selection rules of phonon-assisted optical transitions with electron spins oriented along the light propagation direction (z crystallographic axis). Next to each of the indicated phonon modes, it has been reported the ratio A+B:C+D, which denotes the intensity ratio between right and left circularly polarized luminescence. Contributions from transitions involving heavy (light) holes are denoted by A:C (B:D). Adapted from [28].

L_6^+ and Γ_7^- do not vanish completely, thus LA and TA modes follow the same selection rules [28].

In addition to the relatively strong LA and the weak TA spectral peaks, the spectrum of bulk Ge involves TO spectral features, as illustrated in Figure 2.2. The TO mode is symmetry allowed in edge-to-edge optical transitions (dashed arrows in Fig. 2.7a) only if we consider distant intermediate states in Ge (named Γ_6^- and Γ_8^- in Γ point and L_3^- at the VB zone-edge L-points in Figure 2.7a). It is worth noting that the intensity of the transition *via* L_3^- is much stronger than *via* Γ_6^- and Γ_8^-, with the matrix element of the former being 5 times larger than the latter.

Using the same group theory notations, we take the spin-up $L^+_{6,\frac{1}{2}}$ as the initial state. According to this choice, the final states that take part in optical transitions are $\Gamma^+_{8,+\frac{3}{2}}$ and $\Gamma^+_{8,\pm\frac{1}{2}}$ for HH and LH states, respectively. To obtain the intensity ratios between right and left circularly polarized luminescence, the relative amplitudes of radiation-matter and electron-phonon matrix elements have been calculated by means of the basis functions in Ref. [28]. The selection rules are summarized in Figure 2.7b. We observe that the polarization degree ρ for the LA/TA mediated transition is opposite with respect the polarization of TO mode. Moreover, the intensity ratio between HH and

Transition	Polarization degree
$cL - v\Gamma : TA$	$3.4 \pm 0.7\%$
$cL - v\Gamma : LA$	$2.6 \pm 0.5\%$
$cL - v\Gamma : TO$	$-2 \pm 1\%$

Table 2.4: Polarization degree of the phonon mediated indirect $cL - v\Gamma$ transitions in bulk Ge at T=4 K reported in [42]

LH for either the LA and TA peaks is 3 : 1, which is the same ratio than the direct-gap transitions. The reason is that their dominant optical transitions involve electron-phonon interaction between relatively pure spin states in the lowermost conduction band [28]. This theoretical prediction has been recently experimentally demonstrated by means of optical orientation technique in Ref. [42]. The results are summarized in Table 2.4, reporting the polarization degree ρ of the three phonon-mediated transitions. The opposite sign of ρ openly manifest the helicity reversal between TO and the LA/TA contributions. The experimental data in Ref. [42] show that both the $\mathrm{cL} - \mathrm{v}\Gamma : \mathrm{LA}$ and $\mathrm{cL} - \mathrm{v}\Gamma : \mathrm{TA}$ emission lines are indeed co-circularly polarized with respect to the σ_+ excitation, whilst the $\mathrm{cL} - \mathrm{v}\Gamma : \mathrm{TO}$ transition is counterpolarized. This finding matches with the theory reported in Ref. [28] and corroborates the crucial role played by phonon symmetries in optical orientation experiments.

Since the measured circular polarization degrees, albeit small, are non zero, we can conclude that a fraction of the electron spins are still aligned prior to radiative recombination across the indirect band gap. From Equation 2.7 described in the previous Section, we can conclude that the spin relaxation time T_1 is in the same range of the electron lifetime in the L-valley [42].

In conclusion, both for direct and indirect gap transitions, the polarization degree ρ and thus the steady-state spin polarization P under circularly polarized laser excitation depend on the electrons spin relaxation time T_1. In particular, the longer T_1, the larger P. However, even if T_1 is very long, P is limited by its initial value, P_0. This underlines the importance of spin-orbit coupling in the optical spin orientation process. It should be noted that the VB spin states structure shown in Figures 2.5 and 2.6 clearly suggests that a removal of the HH/LH degeneracy can substantially increase P up to the limit of complete spin polarization [27]. This can be obtained by introducing strain and confinement effects. In the following Chapter, we show that it is possible to exploit these properties in order to address new interesting routes towards the study of spin physics properties of Ge.

3 Band Structure Engineering

In this Chapter we present two of the main tools, beside alloying, for engineering the semiconductors band structure: strain and quantum confinement. We focus on the effect of tensile strain in Ge, presenting the effort reported so far in literature for photonic application. We investigate the nature of strain in the Ge epitaxial layer and present strain effects on optical and spin properties, pointing out the crucial role played by tensile strain in increasing spin polarization of carriers. Then we focus on Si/Ge quantum confined heterostructure. The structural properties of SiGe-based quantum wells are presented, focusing on the effect of confinement on spin properties.

3.1 Strain

In this Section the effects of strain on the Ge band structure are analyzed. Strain modifies the energy and the curvature of the bands and breaks the degeneracies, causing relevant changes in the spin and optical properties of the semiconductors.

In general, strain can be described as a tensor [69]:

$$\varepsilon = \begin{pmatrix} \varepsilon_{xx} & \varepsilon_{xy} & \varepsilon_{xz} \\ \varepsilon_{yx} & \varepsilon_{yy} & \varepsilon_{yz} \\ \varepsilon_{zx} & \varepsilon_{zy} & \varepsilon_{zz} \end{pmatrix}$$

If we consider a material layer with deformation under isotropic in-plane stress, we can define $\varepsilon_{\parallel}$ the strain component in the plane parallel to the sample surface ($\varepsilon_{\parallel} = \varepsilon_{xx} = \varepsilon_{yy}$), and $\varepsilon_{\perp}$ the strain component along the direction perpendicular to the surfaces (ε_{zz}).

A deformation under biaxial stress can be decoupled into two components: hydro-

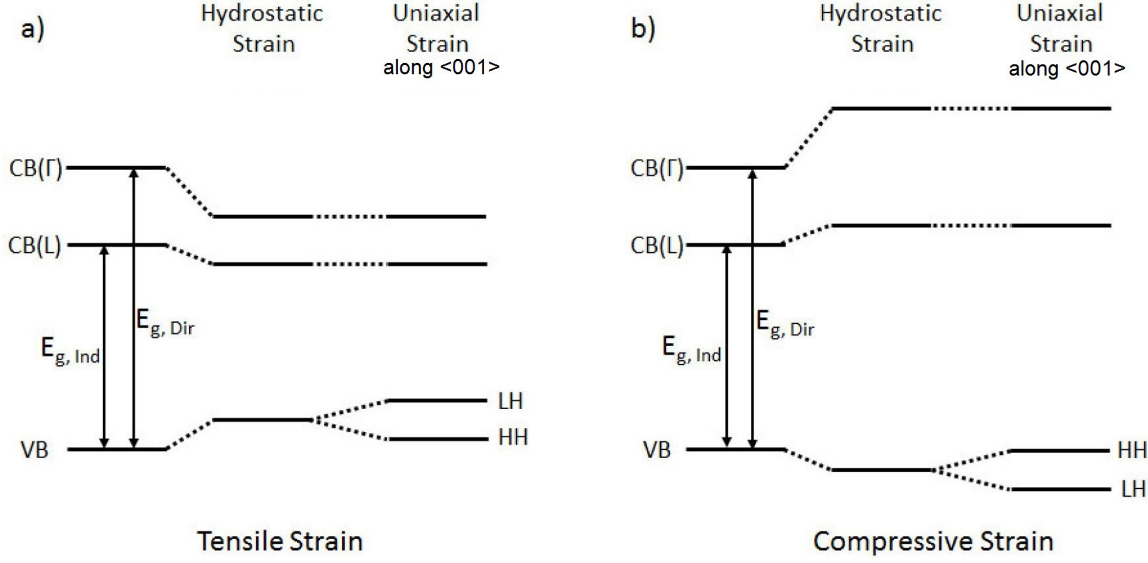

Figure 3.1: Effect of tensile (a) and compressive (b) strain in (001) plane in Ge. Effects of the hydrostatic and uniaxial strain are shown separately.

static and uniaxial. The effects of the two components are schematically shown in Fig. 3.1.

The isotropic hydrostatic component induces a shift of the conduction and valence levels, yielding a variation of the energy gaps. The hydrostatic component is given by the trace of the tensor ε and can be written as [69]:

$$\varepsilon_h = \mathrm{Tr}\varepsilon = \sum_i \varepsilon_{ii} = 2\varepsilon_\parallel + \varepsilon_\perp \tag{3.1}$$

In general, the strain effects on band structure can be described by introducing a perturbation term $\mathscr{H}_\varepsilon$ in the Hamiltonian, defined as [69]:

$$\mathscr{H}_\varepsilon = \begin{pmatrix} l\varepsilon_{xx} + m(\varepsilon_{yy} + \varepsilon_{zz}) & n\varepsilon_{xy} & n\varepsilon_{xz} \\ n\varepsilon_{xy} & l\varepsilon_{yy} + m(\varepsilon_{zz} + \varepsilon_{xx}) & n\varepsilon_{yz} \\ n\varepsilon_{xy} & n\varepsilon_{yz} & l\varepsilon_{zz} + m(\varepsilon_{yy} + \varepsilon_{xx}) \end{pmatrix}$$

where l, m, n are the deformation potential parameters.

In particular, in the case of Ge, both the direct and the indirect bandgaps decrease as a tensile strain is applied [11, 33, 70], while they increase in the compressive case, as sketched in Figure 3.1.

The CB valleys shift can be described as follows:

$$E_c(\varepsilon) = E_c(0) + a_c\varepsilon_h, \tag{3.2}$$

Parameter	a_v	a_c^{dir}	a_c^{ind}	b
Energy (eV)	1.24	-8.24	-1.54	-2.55

Table 3.1: Deformation potential parameters for conduction and valence band of Ge taken from Ref. [71].

where a_c is the volume deformation potential of CB [39, 71]. It is worth noting that the shift of the CB edge is different for the Γ and L valleys, due to different values of a_c^{ind} and a_c^{dir} in Eq 3.2. The values are listed in Table 3.1.

The anisotropic uniaxial component is responsible for the splitting of degenerate levels, *e.g.* HH and LH states at the top of the VB.

The uniaxial component is expressed by [69]:

$$\varepsilon_t = \varepsilon_\perp - \varepsilon_\parallel \tag{3.3}$$

In particular, under compressive strain the top of the VB has a HH character; while under tensile strain the LH state characterizes the top of the VB, as sketched in Figure 3.1. It is possible to describe the strain dependence of the HH and LH energy states as follow [71]:

$$\begin{aligned} E_{hh}(\varepsilon) &= E_{hh}(0) + a_v\varepsilon_h + b\varepsilon_t, \\ E_{lh}(\varepsilon) &= E_{lh}(0) + a_v\varepsilon_h - b\varepsilon_t; \end{aligned} \tag{3.4}$$

where a_v is the VB volume deformation potential and b is a constant, both reported in Table 3.1 [39, 69, 71].

It is worth noting that, for a strain under biaxial stress applied in (001) plane, L and Γ conduction minima are not affected by the uniaxial component. In contrast, the valleys along <001> directions are split: in Figure 3.2 the effect of uniaxial strain along <001> on the Δ valleys of Si is shown. The six-fold degeneracy of the Δ valleys is broken in two-fold degenerate Δ_2 valley and the four-fold degenerate Δ_4 valley. Similarly, the uniaxial component of strain under biaxial stress splits the six valleys in two-fold $\Delta_\perp$ valley and four-fold $\Delta_\parallel$ valley, which are perpendicular and in-plane with respect to the applied strain, respectively. As shown in Figure 3.2, by applying tensile strain the fundamental conduction minima are only two times degenerate (Δ_2 or $\Delta_\perp$) while under compressive strain the CB minimum is four-fold degenerate (Δ_4 or $\Delta_\parallel$).

Following the same line of reasoning, if stress is applied along the <111> crystallographic direction in Ge, the 4-fold L valley degeneracy can be broken in L_3 and L_1 levels [49, 55]: in particular, with the proper value of tensile strain along <111>

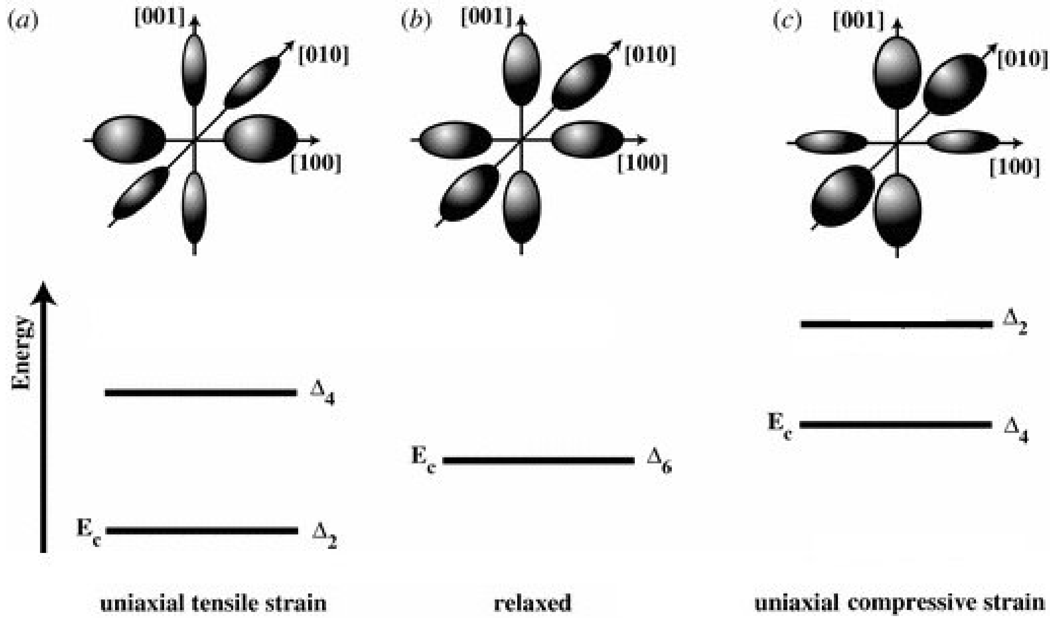

Figure 3.2: Constant energies surfaces (upper panels) and energy splitting (lower panels) of CB minima in Si under the effect of uniaxial tensile (a) and compressive (c) strain, with respect the unstrained case (b). Adapted from [63].

direction, it is possible to remove completely the degeneracy in the L-valley, and the fundamental CB minimum are not degenerate (L_1).

3.1.1 Strain engineering

Strain could open up a new route to overcome the limit which stems from the typical indirect nature of the bandgap of group IV semiconductors, that is the lack of efficient light emitters [72]. To address this challenge, during the last decade, research efforts have been chiefly focused on strained Ge-based light sources [73] for monolithic integration of a group-IV optical circuitry onto the Si platform [74]. The main progresses in this field are reviewed in this Section.

In Ge, strain can be conveniently obtained *via* epitaxial growth of a Ge layer on Si. The maximum strain that can be thereby achieved is of about 0.3%. This strain, albeit very small, is nevertheless useful: various Ge-based LEDs and photodiodes were successfully fabricated on Si, as illustrated by a typical layout in Figure 3.3a [14–17, 75]. Moreover, Liu *et al.* [11] were the first to propose that filling L-valley states *via* n-type doping provide the equalization between Γ and L valley occupancy. This can inhibit the Γ-to-L intervalley scattering naturally occurring and, owing the higher transition rate, favour radiative recombination events *via* the direct gap. The benefi-

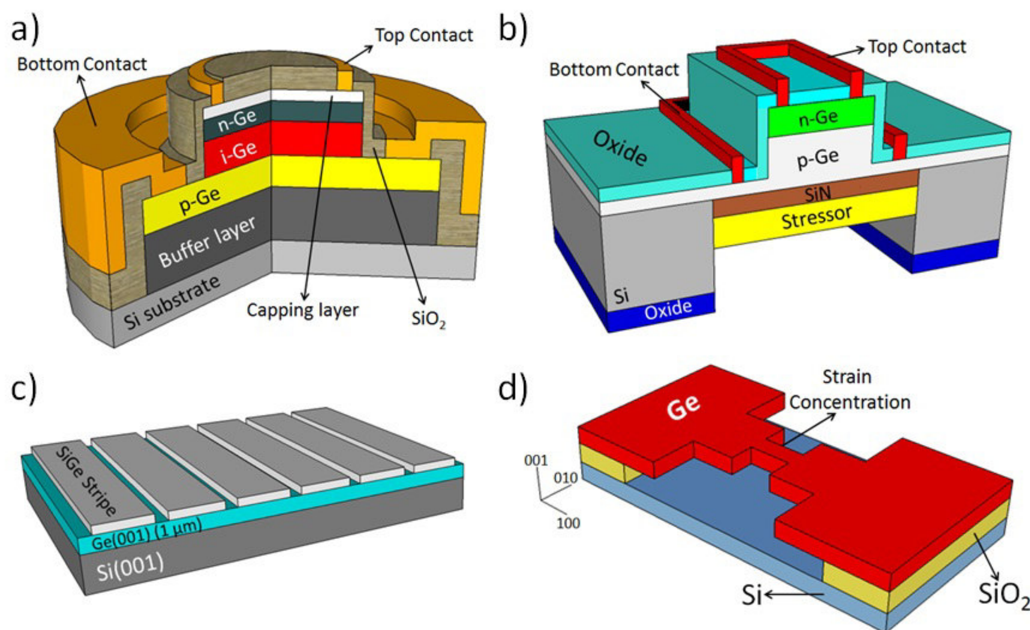

Figure 3.3: Strain engineering approaches [81]. (Drawings not to scale) (a) Typical layout of Ge-based LED and photodiode monolithically integrated on Si [14–17, 75]. (b) Device obtained on highly strained Ge membranes [87, 88]. (c) SiGe stripes patterned on a relaxed Ge layer directly grown on Si substrate [89] (d) Suspended microbridges [90] obtained from underetching of Ge-on-insulator wafers.

cial role played by tensile strain and n-type doping in enhancing direct gap emission has been pointed out by different authors [8, 76–78]. It is worth noting that the combination of the weak thermal strain, described in Section 3.1.2, and high n-type doping was indeed the key enabling factor in the first observation of room temperature laser emission under optical [9] and electrical injection [18]. The original description of the mechanisms leading to stimulated emission in Ge was indeed put under severe scrutiny [79], boosting several theoretical works [19, 80], aimed to accurately evaluate gain/loss mechanisms in an effort to guide experimental investigations.

Many alternatives focused on extending the limit of the attainable strain have thus promptly emerged [81]. As an example, strain engineering was chiefly based on heteroepitaxy: materials with lattice parameter close to but somewhat larger than that of Ge, such as InGaAs, have been investigated [82, 83].

A different approach relies on stressors. These consist of a layer of a material, like silicon nitride or tungsten, overgrown on a Ge membrane under large compressive strain. By doing so, the layer transfers its load to the underlying Ge film inducing therein a tensile strain. [84–86]. Photodiodes and LEDs based on this technology were also fabricated [87, 88], as schematically shown in Figure 3.3b.

Another approach consists in utilizing SiGe directly deposited on top of Ge. After

epitaxial growth, SiGe is patterned in a ridge-like design, as sketched in Figure3.3c. With this technique, the fabrication of free surfaces in the tensile-strained SiGe cap allows strain relaxation and the transfer of a tensile load to the Ge regions in between two adjacent SiGe stripes [89].

Uniaxially-strained Ge layers have been also fabricated by taking advantage of the thermal mismatch between Si and Ge [90]. As alternative to the previously-described methods, constricted Ge suspended microbridges, with a typical layout sketched in Figure 3.3d, were obtained [90].

Finally, Ge can be also strained by utilizing external mechanical stress, allowing the control of the material properties simply by varying the applied stress. In addition, a strain-tunable wavelength range opens up the possibility to get a tunable light source integrated on Si [91]. Further benefits are expected from the use of nanomembranes, which, owning to a reduced layer thickness, can mitigate the possible issues arising at large strain because of plastic relaxation and concomitant defect formation. This technology is based on the complete or partial release of a semiconductor layer, with a thickness of a few tens of nm, from its original substrate *via* the selective etching of an underlying sacrificial layer. When completely released, the Ge membrane can be transferred and bonded onto a variety of substrates. Nanomembranes offer novel opportunities for strain engineering, both through spontaneous elastic strain and through the external application of mechanical stress [92, 93].

3.1.2 Ge epitaxially grown on Si

The epitaxial growth is the deposition of a material layer on a crystalline substrate which determines its crystal orientation. In particular, when the epitaxial layer adapts its lattice parameter in the growth to those of the substrate is defined as pseudomorphic growth.

As a consequence, the layer experiences a strain proportional to the lattice mismatch, *i.e.* to the difference between the lattice parameter of the epilayer and the one of the substrate. As the thickness of the strained epilayer increases, the elastic energy stored in the growing film rises, with a linear dependence between the energy and the thickness [94, 95]. The in-plane strain in the epitaxial layer can be described by:

$$\varepsilon_{\parallel} = \frac{a_s - a_e}{a_e} \tag{3.5}$$

where a_s is the substrate lattice parameter and a_e the equilibrium lattice parameter of the epilayer. For $a_s > a_e$ ($a_s < a_e$), $\varepsilon_{\parallel}$ is tensile (compressive) and, as a consequence, the perperdicular component $\varepsilon_{\perp}$ is compressive (tensile).

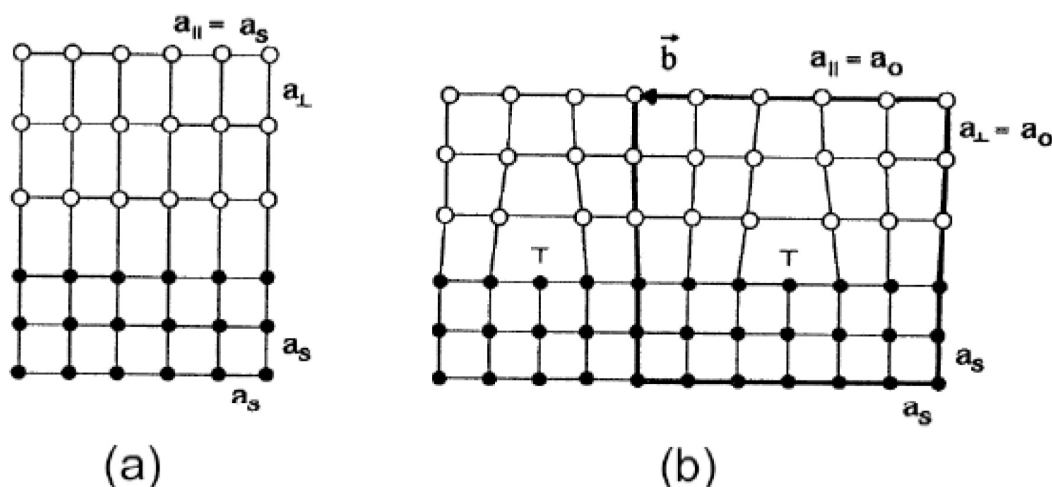

Figure 3.4: (a) Schematic diagram of a Ge film grown pseudomorphically on a Si substrate. The layer is under compressive strain: the in plane lattice parameter, $a_{\parallel}$, is smaller than the out of plane lattice parameter, $a_{\perp}$. (b) A relaxed Ge layer in which strain is relieved by the introduction of misfit dislocations, described by the Burgers vector $\vec{b}$ [100].

The pseudomorphic growth of an epilayer on a substrate with different lattice parameter can not proceed indefinitely. The system might relieve the strain by reducing its free energy through the introduction of structural defects, as illustrated in Figure 3.4 [96], named dislocations. These extended defects relieve the strain, reducing the whole energy of the system, even though their injection requires a minimum energy. There exist a film thickness, called critical thickness, beyond which the introduction of such defects becomes more favourable [97]. In general, dislocations lie along the lowest energy crystallographic directions and, in the case of Si-Ge heterostructures, these defects are named misfit and threading dislocations [98]. Misfit dislocations run along <110> and <$\bar{1}$10> directions, whilst threading dislocations pierce through the epilayer towards the free surfaces, as sketched in Figure 3.4. A detailed discussion about dislocation formation and structure is provided in Ref. [99].

Dislocations are defects that perturb the periodicity of the lattice. In particular, they introduce electronic levels within the band gap of a semiconductor, thus affecting optical and electronic properties of the material.

Si and Ge have different lattice parameter: a_{Si} = 0.54 nm and a_{Ge} = 0.56 nm at RT, respectively. In a pseudomorphic growth of Ge epilayer on Si, the lattice mismatch is of about 4% and induces a compressive in-plane strain in the Ge epilayer, with a critical thickness of about 4 nm. Above this thickness, the generation of dislocations is favourable [95] and the epilayer becomes relaxed.

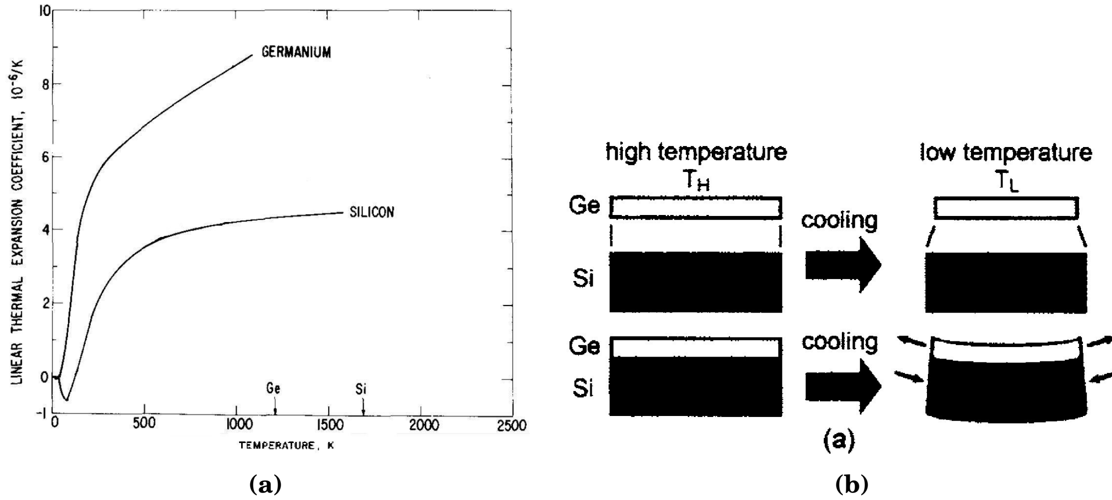

Figure 3.5: (a) Thermal expansion coefficient of Ge and Si as a function of temperature from Ref. [101]. (b) Schematic illustration of deformation of Ge and Si crystals before and after cooling from a high-temperature T_H to a low-temperature T_L. Adapted from Ref. [70].

Thermal tensile strain

The deposition of a thick layer of Ge on Si, above the critical thickness, provides a relaxed layer at the growth temperature. However, by cooling down the structure to RT, the epilayer is subjected to tensile strain. This strain is due to the difference in thermal expansion coefficients between Ge and Si [101] as shown in Figure 3.5a. The thermal expansion coefficient α_{Ge} is greater than the one of Si (α_{Si}) in all the temperature range [101, 102].

Figure 3.5b schematically shows the structural deformation of Ge and Si crystals before and after the cooling from the high growth temperature T_H to lower temperatures T_L. If the Ge layer is spatially separated from the Si substrate, as sketched in upper part of Fig. 3.5b, a larger lattice shrinkage occurs for the Ge after the cooling. When the Ge layer is grown on Si substrate, the shrinkage of Ge lattice during the cooling is prevented by the thick Si substrate. This generates a tensile stress biaxially, as shown in the lower part of Fig. 3.5b. Assuming that the Ge film is completely relaxed at the initial growth temperature by generating misfit dislocations, the in-plane strain in the Ge layer at the low temperature T_L is theoretically given by the following equation [101]:

$$\varepsilon_{\|Ge}(T) \propto \int_{T}^{T_H} [\alpha_{Ge}(T) - \alpha_{Si}(T)]\, dT, \tag{3.6}$$

where T_H is the highest temperature reached during the growth process. In the samples studied in Chapter 4, T_H is the maximum annealing temperature, *i.e.* 800°C.

The calculated biaxial tensile strain at RT is of about 0.18%-0.20%. Further details about the samples growth are provided in Appendix B.

As discussed in details above, in a tensile strained Ge epilayer, the isotropic hydrostatic component induces a shrinking of both the direct and the indirect band gaps, reducing their energy differences [33, 70]. The anisotropic uniaxial component splits the HH and LH states at the top of the VB, with the LH band higher in energy with respect the HH level. The energy difference between LH and HH levels in the Γ-point for the biaxial tensile strain of about 0.2% described above is about 20 meV at low temperature, and close to 10 meV at RT [33].

3.1.3 Optical properties of strained Ge

Tensile strain [10] has been extensively investigated as a means for minimizing the energy difference between the fundamental indirect gap and the direct gap in Ge. Theory predicts that the direct gap shows a more pronounced strain-induced redshift than the indirect gap, so that for a tensile strain in the (001) plane of about 2%, Ge becomes a direct semiconductor with a bandgap width close to 0.5 eV [10]. It should be noted that the indirect-to-direct crossover has been predicted to occur also in the case of uniaxial stress, even though this requires strain values as high as 4% along the <001> and <111> crystallographic directions [103–106].

The reduction in energy difference between the direct and indirect valleys due to <001> [77] or <111> [107] uniaxial component of tensile strain resulting from a biaxial

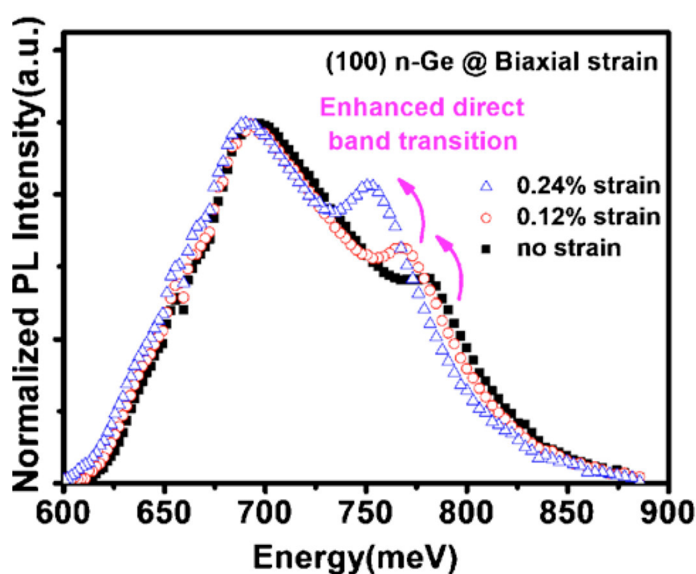

Figure 3.6: PL spectra of n-type bulk Ge <001> under biaxial tensile strain at room temperature. The intensity of direct band gap transition increases with increasing strain. Adapted from Ref. [77]

stress increases the electron population in the direct valley, and enhances the direct transition, as illustrated in Figure 3.6.

3.1.4 Spin properties of strained Ge

In the context of spin physics, strain can be exploited to modify the relaxation mechanisms and thus the spin lifetimes [23, 27, 28]. Furthermore, the zone-center removal of LH and HH degeneracy can significantly improve the optical generation of nonequilibrium spin populations [23]. The optical orientation of spin in a material near the limit of complete spin polarization has been demonstrated in strained III-V semiconductors [23, 29]. This has been achieved through resonant absorption of circularly polarized light at an excitation energy that matches the fundamental strain-split transition [23, 29]. Similar possibilities have been pointed out in indirect gap systems based on group IV materials, such as tensile strained Ge on Si [33] and Ge quantum wells under compressive strain [34, 108–111]. These phenomena are analized further in the following Chapters.

Recent theoretical works [49, 55] suggested that one of the main spin relaxation channels in Ge is the intervalley scattering within the four-fold degenerate L-valleys. Tang *et al.* [55] reported a tight binding model to calculate the intrinsic spin relaxation of conduction electrons in Ge as a function of the energy splitting between the lower conduction valley and the others. In a different paper, Li et al. [49] employed group theory to obtain the intervalley spin flipping matrix elements for electron scattering between different energy-minima points. In particular, they disentangled intervalley and the intravalley scattering contributions to the electron spin lifetime, showing that, due to the uniaxial compressive strain along <111> crystallographic direction, the L-valley degeneracy is completely removed, thus resulting in a single low-energy valley oriented along the strain axis. They demonstrated that, if the strain level is large enough, the energy splitting is sufficient to quench the intervalley spin relaxation mechanism [49, 55]. This is suggested as the optimal condition to achieve a lengthening of the spin lifetime in Ge up to 1 μs at room temperature [49].

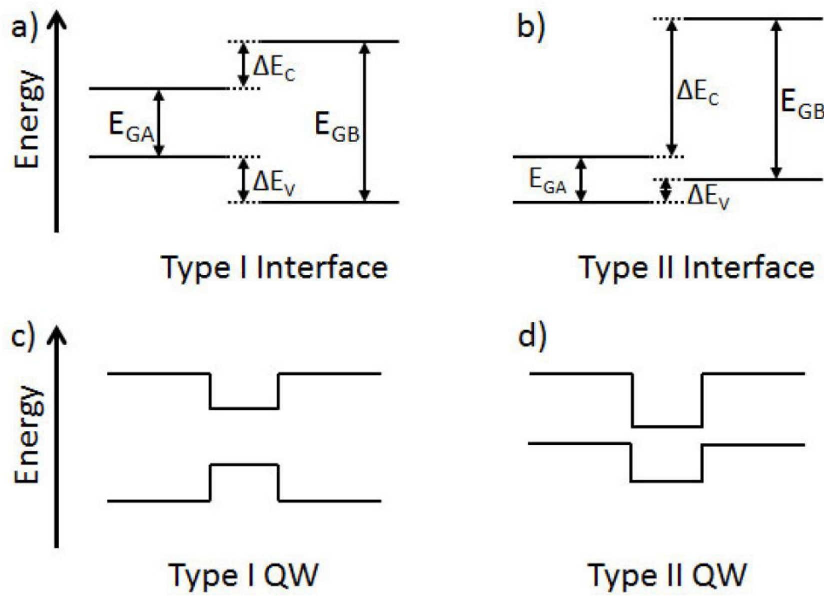

Figure 3.7: Band-edge alignment between the band gap of the well (E_{GA}) and the barrier (E_{GB}) of type I (a, c) and type II (b, d) quantum wells. ΔE_C and ΔE_V are the energy differences of the two conduction and valence bands, respectively.

3.2 Quantum Confinement

Quantum wells (QWs) have attracted a great interest, since they offer the possibility to localize carriers and, thus, to increase the efficiency of radiative transitions [31, 112–114]. QWs are two-dimensional heterostructures in which electrons and holes are spatially confined in a region characterized by a thickness comparable with their de Broglie wavelength. Carrier confinement is achieved by embedding a nanometric layer of a semiconductor (well) into a matrix of a material with an higher gap (barrier).

The way in which the top of the VB and the bottom of the CB align with respect to each other is crucial in these heterostructures. In type I QWs, the VB top of the well is higher in energy than in the barrier, while the CB bottom is lower, as sketched in Figure 3.7. On the other hand, in type II QWs, the CB and VB bands of the well are both below or above the corresponding bands in the barriers. As a consequence, in a type I band alignment both electrons and holes are confined within the same spatial region, whilst in the type II, only electrons or holes are confined within the well. For this reason, nanostructures with type I band alignment are more interesting from the point of view of optoelectronic applications, since a greater overlap of the wavefunctions is caused by the spatial confinement of both types of carriers, thus yielding an increased recombination efficiency with respect to the type II.

In this Section we focus on Ge quantum wells (QWs) in SiGe barriers. After intro-

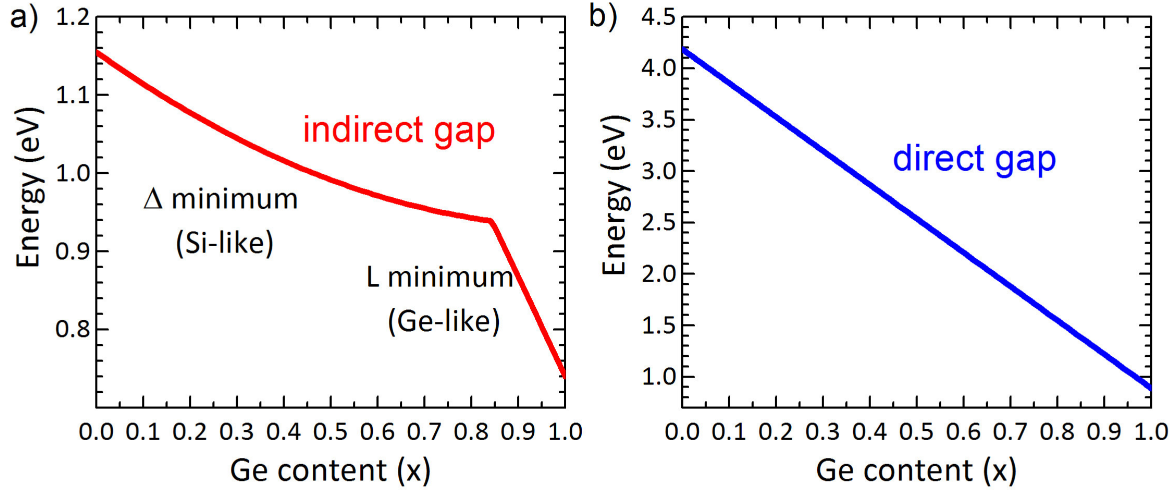

Figure 3.8: Indirect (a) and direct (b) excitonic bandgap of $Si_{1-x}Ge_x$ alloys as a function of Ge molar fraction (x) [115].

ducing the properties of SiGe alloys, we linger on strain and band structure engineering effects on spin properties.

3.2.1 SiGe alloys

Si and Ge are fully miscible. $Si_{1-x}Ge_x$ alloys (like Si and Ge) are indirect-gap semiconductors for all the Ge concentrations. For a Ge molar fraction, x, lower than 85%, the CB absolute minima lies in the Δ valleys along <001> directions (Si-like), while for a larger Ge content they are in the L valleys (Ge-like), as shown in Figure 3.8a. Figure 3.8 shows the monotonic decrease from Si to the Ge bulk value for both the indirect and direct excitonic band gap. The latter presents a very steep linear dependence on the Ge content x described by [115]:

$$E_\Gamma = E_\Gamma^{Si} - 3.286 \cdot x \ eV \tag{3.7}$$

where E_Γ^{Si} = 4.182 eV is the direct band gap of bulk Si.

SiGe alloys stabilize in a diamond crystalline structure in which the lattice parameter a of these solid solutions varies from the one of pure Si (a_{Si} = 0.54 nm) to that of pure Ge (a_{Ge} = 0.56 nm). The linear dependence of the alloy lattice parameter is well described, to a first approximation, by the empirical Vegard's law [116]:

$$a_x = a_{Si}(1-x) + a_{Ge}x = a_{Si} + x\Delta a \tag{3.8}$$

When a $Si_{1-x}Ge_x$ layer is epitaxially grown on a $Si_{1-y}Ge_y$ substrate with different composition, it adapts its lattice parameter to the one of the substrate in a pseudo-

morphic growth. As a consequence, the layer experiences a strain. This strain under biaxial stress is compressive in the plane and tensile in the growth direction if $x > y$, and tensile in the plane and compressive in the growth direction if $y > x$. The structural strain is proportional to the lattice mismatch, *i.e.* to the difference between the lattice parameter of the epilayer and the one of the substrate, as reported by Eq.3.5.

Moreover, a thermal strain appears in the epilayer which adds to the structural one. Extending the discussion of Section 3.1.2 to SiGe alloys, the dependence of their expansion coefficient on T is expected to be intermediate between those of Ge and Si, depending on the composition. As the thickness of the strained epilayer increases, the elastic energy stored rises, and the system relieves the strain lowering its total free energy by means of the nucleation of dislocations [97].

3.2.2 Band Alignment

A full description of valence band and conduction band alignment in a $Si_{1-x}Ge_x$ strained material epitaxially grown on a relaxed $Si_{1-y}Ge_y$ buffer along the <001> direction is provided in Ref. [117]. By modifying the x and y concentrations and the growth direction, a large variety of different band structures and charge carrier effective masses can be tailored.

Figure 3.9 shows the fundamental energy gap, the band offsets and the band alignment of the active material as a function of x and y [117]. The line $x = 0$ represents the case of pure strained Si grown on an alloy with Ge fraction y; the line $y = 0$ reproduces a strained alloy with x Ge fraction, grown on pure Si. This calculation qualitatively confirms that the biaxial strain breaks the sixfold degeneracy of the Δ line in k-space giving rise to a twofold degenerate $\Delta_{\perp}$ axis and a fourfold degenerate $\Delta_{\parallel}$ axis. We can therefore distinguish in Figure 3.9a three domains according to the k-position of the bottom of conduction band: a first region, for $x < y$, where the bottom is along the orthogonal axis $\Delta_{\perp}$, a second region for $x > y$ where it is along the parallel direction $\Delta_{\parallel}$, and a third one characterized by weakly strained alloys with high Ge content where the bottom of the conduction band occurs at the L point and therein the alloy is Ge-like [117]. In this calculation, based on the tight binding method, it is assumed that the substrate is relaxed while the active material layer is pseudomorphically grown on the substrate, and consequently strained.

It is worth noting the band alignment shown in Figure 3.9d: in the *(x, y)* space we can distinguish four regions according to the sign of the valence band offset (VBO, Figure 3.9b) and the conduction band offset (CBO, Figure 3.9c) produced at the heterointerface. In region (i) VBO < 0 and CBO < 0, in region (ii) VBO < 0 and CBO > 0, in region (iii) VBO > 0 and CBO < 0 and finally in region (iv) VBO > 0 and CBO >

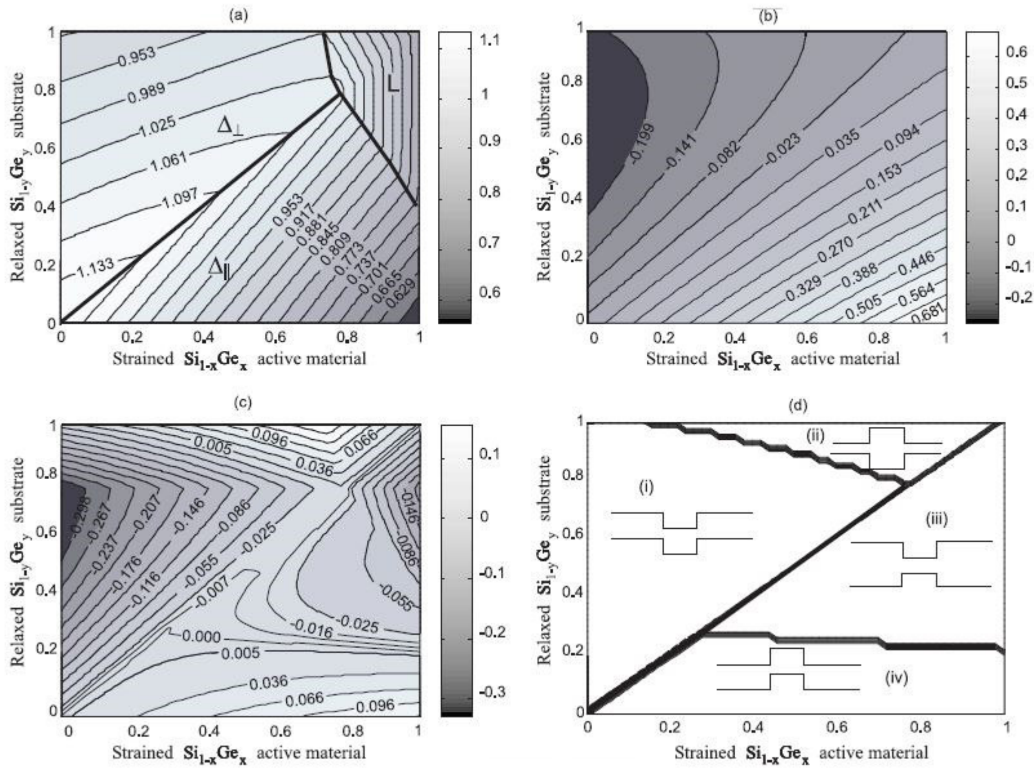

Figure 3.9: (a) Fundamental bandgap energies; (b) valence band offsets; (c) conduction band offsets and (d) band-edge profiles of $Si_{1-x}Ge_x$ alloys as a function of the Ge concentration, x, in the strained active material and in the substrate, y. The latter determines the $a_{\|}$ lattice parameter of the active layer. Adapted from Ref. [117].

0. A type-I alignment for band edges is thus predicted for region (iii), with both types of carriers at the fundamental gap that are spatially confined in the active layer zone [117].

In Chapter 5 of this thesis, we study Ge/SiGe multiple QWs (MQWs) samples with Ge-rich barriers (*x = 1, y = 0.85*), and we briefly focus on the results achieved in this system. In the case of strained Ge QWs embedded in barriers with Ge content higher than 0.4, the fundamental energy gap in the well layer involves the conduction minimum at L. The positive value of CBO reported in Fig. 3.9c for the compositions of interest indicates that the L minimum of the CB in the Ge well is lower in energy respect to that of the $Si_{0.15}Ge_{0.85}$ barriers. On the contrary, the negative value of Fig. 3.9b allows to conclude that the VB maximum in the Ge well is higher in energy with respect to that of the $Si_{0.15}Ge_{0.85}$ barriers. These offsets yield the type-I band alignment, sketched in Fig 3.9d for the indirect gap of Ge/$Si_{0.15}Ge_{0.85}$ QWs.

Finally, it should be noticed that in the Ge/SiGe QW samples analyzed in this work, both well and barrier layers are strained because they adapt their lattice parameter to the one of the final layer of the virtual substrate (VS), while in the calculations

summarized in Figure 3.9 the barriers are assumed to be relaxed. Anyway, the band alignment reported in Figure 3.9 can be applied as a well description of our case, since the composition of the barriers (0.85) and that of the VS (0.90) are close, so the tensile strain in the barriers is quite small.

3.2.3 Spin properties of Ge QWs

The importance of semiconductor QWs systems lies also in the spin properties of the electronic states. Studies of spin relaxation in those systems are driven not only by the need for fundamental understanding of spin relaxation and decoherence, but also by the perspective of finding ways to reduce or otherwise control spin relaxation and coherence in general [23]. The difference between the system with reduced dimensionality and the bulk lies in the localization of the wave function into two dimensions and the appearance of structure-induced random magnetic fields. Spin relaxation in semiconductor heterostructures is thus caused by random magnetic fields originating either from the base material or from the heterostructure itself [23]. All four mechanisms of spin relaxation presented in Section 2.3 can also be important in QWs, depending on the material, doping, and geometry.

In III-V compounds low dimensional heterostructures, the Dyakonov-Perel and hyperfine interaction are believed to be most relevant [23]. It was shown that size quantization significantly reduces spin relaxation of holes, due to the lifting of heavy and light hole degeneracy [118]. Moreover, the reduction of spin relaxation *via* the Bir-Aronov-Pikus electron-hole exchange interaction can be obtained through spatially separating the two carriers [23].

In Ge heterostructures, a relevant reduction of spin relaxation mechanism T_1 is expected [23], as the Elliott-Yafet mechanisms, effective for conduction electrons, is less efficient for localized quantum states [23]. In a 2D electron gas (2DEG), like in quantum wells, the probability of spin-dependent scattering events *via* Elliot-Yafet mechanism provides transverse relaxation of in-plane spin components, but does not affect out-of-plane spin components [34]. For lower dimensional localization, *e.g.* the electrons bound on donors, the Elliot-Yafet mechanism is less effective and the dominant mechanism is a hyperfine-interaction process [23].

Hyperfine interaction can be relevant also in 2DEG heterostructures, by affecting the spin dephasing time T_2. In quantum wells itinerant L-valley electrons experience an effective suppression of the hyperfine relaxation and are expected to yield the so-called motional narrowing. Nevertheless, during their random walk within the QW plane, electrons are likely to reside for a finite time in smooth potential islands induced by thickness fluctuations. This partial localization enhances the Fermi contact

interaction between the spin and the local nuclear fields, sustaining dephasing.

Another spin relaxation channel is known to be the impurity-driven electron scattering [23]. In quantum wells systems, this relaxation channel can be suppressed by spatially separating the carriers from their donor atoms. This effect can be achieved by means of modulation doping in Ge/SiGe quantum wells structures, as discussed in detail in Chapter 5.

4 Germanium on Silicon

In this Chapter we provide an overview of the optical properties of epitaxial Ge thick layers grown on <001>-oriented Si substrate (Ge-on-Si), which are relaxed at the growth temperature. We focus on the spin properties studied *via* optical spin orientation, described in Section 2.4, pointing out the crucial role played by tensile strain in increasing spin polarization of carriers. In particular, the study of polarization-resolved continuous-wave photoluminescence (CWPL) by means of the full Stokes analysis (detailed in Appendix C) provides an important tool for resolving the strain-split HH and LH contributions. A model of carrier dynamics, supported by theoretical tight binding calculation is presented, providing a description of the non-trivial spin physics occurring in Ge-on-Si layers. Finally, the effect of doping and temperature on the spin properties is investigated.

4.1 Sample structure

The samples analyzed in this Chapter consist of 1.5-2 μm thick Ge layers grown on <001>-oriented Si substrate *via* low energy plasma enhanced chemical vapor deposition (LEPECVD). Further details about the growth technique can be found in Appendix B and in Ref. [119]. The samples, listed in Table 4.1, have been grown and characterized by Dr. J. Frigerio at the LNESS laboratory in Como (Italy).

We have carried out Raman spectroscopy measurement at room temperature on 9173-F6 (i-Ge), 9223-F5 (n-Ge) and 9261-F5 (p-Ge) samples to evaluate the strain value in Ge layers. Figure 4.1 shows the Raman peak of the three samples with respect to an unstrained bulk Ge reference. The peaks positions demonstrated that the biaxial tensile strain is the same for all the samples. To calculate the strain value we

Sample name	Doping type	Doping concentration (cm^{-3})	Thickness (μm)
9173-F6 (i-Ge)	undoped	$\sim 10^{15}$	2
9261-F5 (p-Ge)	p-type (B)	$4.5 \cdot 10^{17}$	1.5
9223-F5 (n-Ge)	n-type (P)	$4.5 \cdot 10^{17}$	1.5
8869-E6	p-type (B)	$3 \cdot 10^{16}$	1.5
8870-E6	p-type (B)	$9 \cdot 10^{17}$	1.5
8871-E6	p-type (B)	$2 \cdot 10^{17}$	1.5
8872-E6	p-type (B)	$5 \cdot 10^{17}$	1.5

Table 4.1: Samples of Ge-on-Si studied in this thesis.

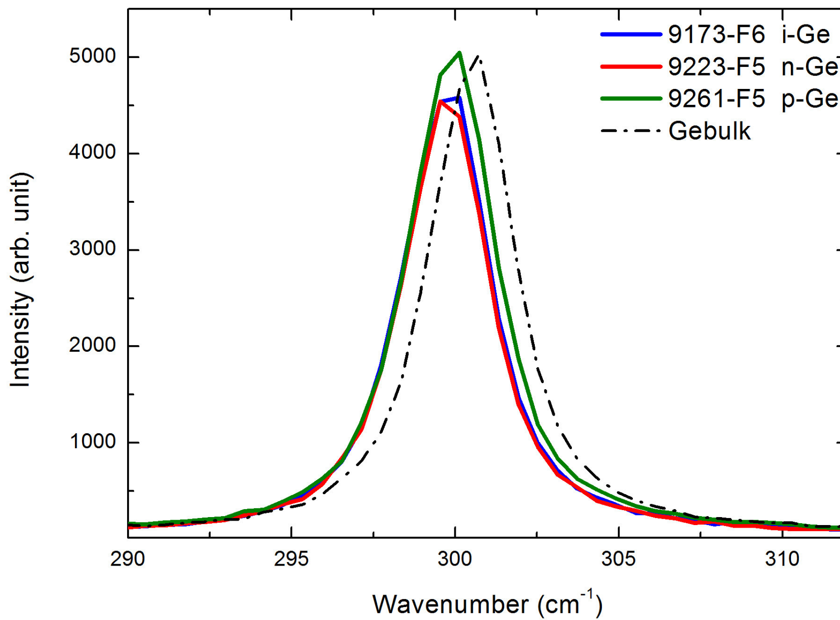

Figure 4.1: Raman spectra of i-Ge, p-Ge and n-Ge (solid lines) at room temeperature. The Raman shift of the samples are compared with the one of relaxed bulk Ge (dashed line), pointing out a redshift stems from thermal tensile strain.

have applied the following relation [120]:

$$\omega_s = \omega_0 - b\ \varepsilon \Longrightarrow \Delta\omega = \omega_0 - \omega_s = b\ \varepsilon_{\parallel} \tag{4.1}$$

where ω_0 and ω_s are the Raman shift for the unstrained and the strained case, respectively, and b = 408 cm^{-1} is a constant reported in Ref. [120]. From the data shown in Figure 4.1, a $\Delta\omega$ of 0.7 ± 0.1cm^{-1} is measured, from which it results a biaxial tensile strain of $\varepsilon_{\parallel} = 0.18 \pm 0.02\%$, in agreement with calculation on thermal strain from Eq. 3.6 reported in Section 3.1.2.

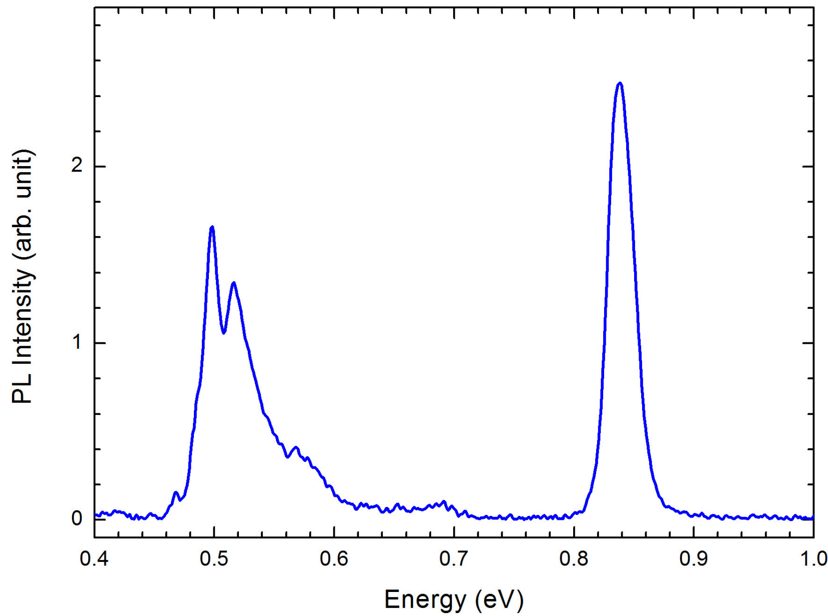

Figure 4.2: PL spectrum of 8872 Ge-on-Si sample with $5 \cdot 10^{17}$ B concentration at 6 K under 1.165 eV excitation. The two spectral features at 0.84 eV and at about 0.5 eV are ascribed to direct bandgap and dislocations levels recombinations, respectively.

4.2 Optical properties of Ge-on-Si

In Section 3.1.3 we pointed out how tensile strain is effective in boosting the direct emission in Ge with respect the indirect one.

Figure 4.2 shows a CWPL measurement of sample 8872-E6, with a boron concentration of $5 \cdot 10^{17}$ cm^{-3} at 6 K excited by the 1.165 eV line of a Nd:YVO$_4$ laser. The excitation power density was about 5 kW/cm^2. The PL was probed by PbS detector using Fourier-Transform Infrared Spectroscopy (FTIR) system.

The spectrum clearly points out the recombination due to the direct $c\Gamma - v\Gamma$ transition at 0.837 eV, while the emission due to fundamental $cL - v\Gamma$ transition is not clearly visible. Moreover, there is a broad emission in the low energy part of the spectrum (0.49-0.56 eV), which can be ascribed to recombination at dislocations levels [121, 122]. The absence of indirect recombination is related to the presence of dislocations as well: as described in Section 2.2, in Ge the satellite Δ- and L-valleys energy relaxation is the most efficient thermalization process after photoexcitation in the Γ-valley [25] with a characteristic time lying in the hundreds of fs regime [32, 123], while in the absolute minima of the L-valleys, electrons exhibit a long lifetime τ_L in hundreds of ns at low temperature [41, 42]. For this reason, the dislocations-related

non-radiative recombination processes, which have a characteristic lifetime lying in the tens of ns range [124], affect the indirect-gap recombination, while they do not play any role in the direct-gap transition.

In the following Sections, we focus on direct-gap emission of Ge-on-Si samples, performing a full-characterization *via* polarization-resolved CWPL as a function of doping and temperature.

4.3 Spin properties of Ge-on-Si

This section provides details about the investigations of spin and energy relaxation processes in tensile-strained Ge-on-Si. All the data discussed in the following refer to polarization-resolved CWPL measurements carried out in back-scattering geometry on samples described in Table 4.1. A full discussion of the experimental set-up is given in Appendix A.1.1. Samples were excited by right-handed (σ_+) circularly polarized laser light at 1.165 eV energy with a power density of about 4 kW/cm^2. The PL peak amplitude was measured by a spectrometer equipped with an InGaAs array multiple-channel detector with cutoff energy at 0.75 eV. PL spectra were measured at different orientation angles (θ) between the fast axis of the quarter waveplate (λ/4) and the linear polarizer axis. The dependence of the PL peak intensity on the analyzer angle θ allowed us to perform the Stokes analysis of the data (described in details in Appendix C), thus providing information about the helicity and the circular polarization degree ρ of the emitted light. The list of investigated samples is given in Table 4.1.

Figure 4.3 reports the direct transition $c\Gamma - v\Gamma$ of 9173-F6 (i-Ge) measured at 4 K. The upper panel of Fig. 4.3 shows the color-coded maps of the PL intensity as a function of the analyzer angle. It is worth noting that the intensity oscillations have a period equal to π. The lower panel of Figure 4.3 better emphasizes such a result, by reporting line scans from the maps at the analyzer angles of 45° (black curve) and 135° (red curve). The latter (former) corresponds to σ_+ (σ_-) circularly polarized PL, *i.e.*, emission copolarized (counterpolarized) with respect to the excitation. A well-defined PL peak can be observed with a maximum at 0.855 eV. The σ_+ component of the emission is exceedingly brighter than the σ_- counterpart, yielding a large PL circular polarization degree $\rho = 85 \pm 1\%$. It is worth noting that, to the best of our knowledge, this is the highest polarization reported so far in literature [33] of group-IV semiconductors, despite an off-resonance excitation of more than 300 meV. Unexpectedly, the measurement of the σ_- component, *i.e.* black spectrum of Fig. 4.3, unveils the presence of an additional weaker PL line at 0.874 eV. The two peaks observed in i-Ge have indeed opposite circular polarizations, with the lowest energy component of

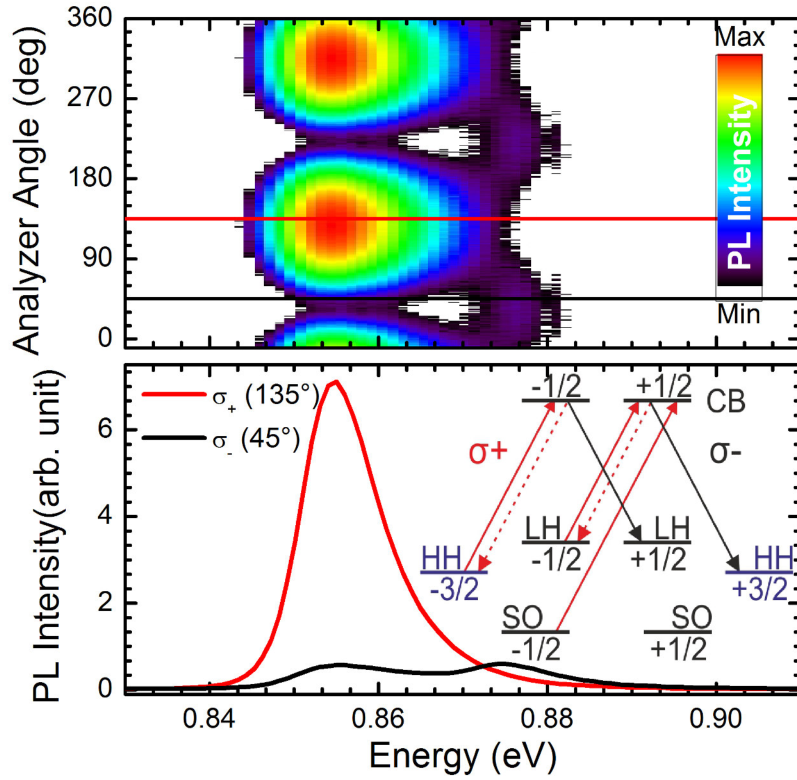

Figure 4.3: 4K PL of intrinsic Ge-on-Si epilayer resolved for left (σ_-) and right-handed (σ_+) helicity. The upper panel provides the full polarimetric analysis reporting the colour-coded PL intensity map as a function of the angle between an optical retarder and a linear polarizer placed along the emission path. The inset is a scheme of the dipole-allowed transitions for right-handed (σ_+, red lines) and left-handed (σ_-, black lines) circularly polarized light involving HH, LH and SO states in the valence band (VB), and conduction band (CB).

the doublet being copolarized with the laser excitation, while the highest energy one is counterpolarized. This cross-polarized PL features can be ascribed to direct radiative recombinations of electrons with strain-split LH ($c\Gamma-$LH) and HH ($c\Gamma-$HH). As described in Section 3.1, $c\Gamma-$LH is the fundamental transition, *i.e.* the low energy peak of the doublet, due to the tensile strain in the Ge-on-Si heterosystem. Relying on the spin-dependent selection rules for the dipole-allowed transitions at the zone-centre [23], shown as inset in Figure 4.3, our findings suggest that the majority of the conduction carriers involved in the radiative recombination has a spin up orientation.

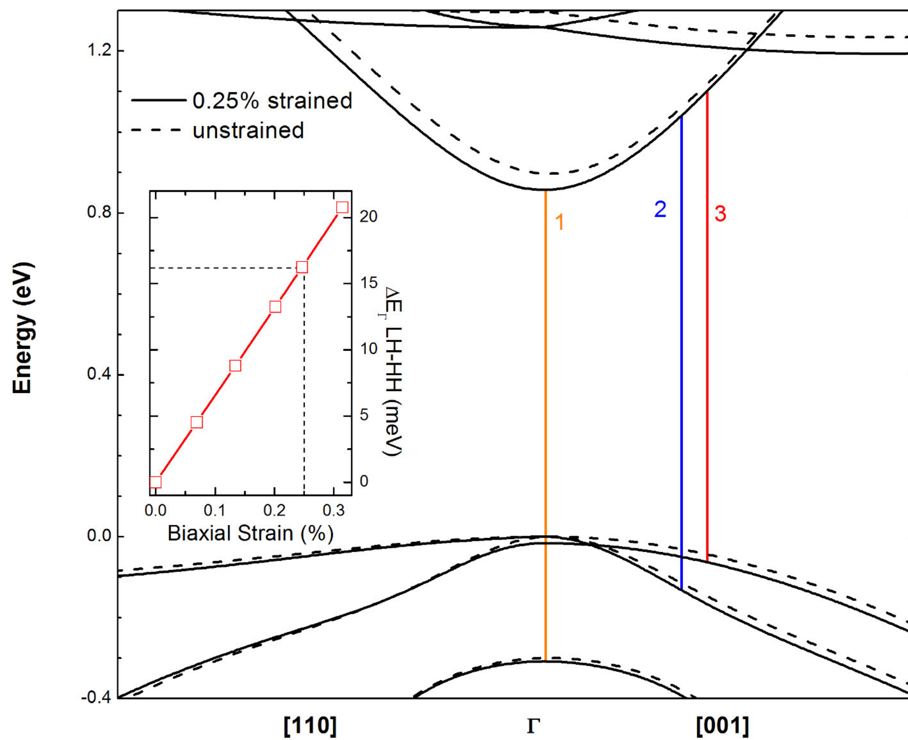

Figure 4.4: Low temperature band structure of relaxed bulk Ge (dashed lines) and of Ge with 0.25% biaxial tensile strain (solid lines), *i.e.* the Ge-on-Si heterostructure. Vertical transitions from 1 to 3 are promoted respectively by the absorption of photons at $\hbar\omega_p = 1.165 eV$ from the SO states near Γ, the second (V2) and the topmost (V1) out-of-zone-center VB states. In the inset the strain-induced LH-HH splitting calculated *via* the tight-binding method at Γ as a function of a biaxial tensile strain is plotted.

4.3.1 Tight-binding calculations

To study further the origin of the exceptionally high ρ observed in sample 9173-F6 (i-Ge), we have evaluated the low temperature electronic band structure and the photogenerated spin population by means of a first-neighbour tight-binding Hamiltonian. The calculation were performed by Dr. M. Virgilio at the University of Pisa (Italy).

We adopt the parametrization first proposed in Ref. [125], which includes $sp^3d^5s^*$ orbitals and spin-orbit interaction [33]. The two main effects of strain are summarized by the calculated band structure shown in Figure 4.4: the removal of the LH/HH degeneracy at the Γ-point and the band-gap shrinking. At a value of $\varepsilon_{\parallel} = 0.25\%$, which is used in our calculations to model the thermal strain of Ge-on-Si at 4 K, the expected LH-HH splitting is 16 meV, as shown by the inset of Figure 4.4. This is consistent with the separation of 19 meV measured for the two cross-polarized PL lines of i-Ge shown in Figure 4.3, and it underlines the potential of polarization-resolved PL spectroscopy to probe the strain-induced changes of the electronic structure. Moreover, Figure 4.4

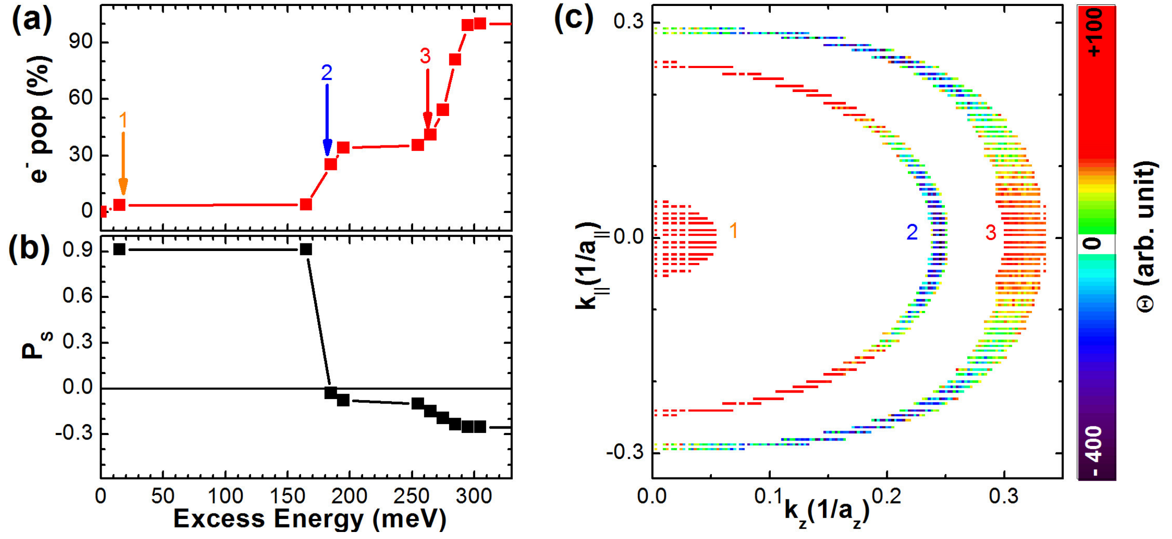

Figure 4.5: Relative population (a) and spin polarization P_S (b) as a function of the excess energy of CB electrons optically promoted by σ_+ excitation. (c) Color-coded map of the photogenerated electronic spin population Θ as a function of the components of the electron momentum.

elucidates that the main effect of the band-gap narrowing on the optical orientation process is that the absorption of photons at 1.165 eV provides a sizeable access to the cΓ – SO transition (named 1 in Figure 4.4). We notice, as shown in Figure 4.5a, that the fraction of carriers excited from the top of the SO band is only about 4%. Most of the electrons are generated from the topmost VB states (*via* the transitions named 2 and 3 in Figure 4.4), due to the much larger joint density of states associated with this transitions out of the zone center, and they thus possess a much larger kinetic energy with respect to the ones optically coupled to the SO states. More precisely, at the adopted pump energy of 1.165 eV, the latter transitions produce CB electrons with an excess energies of about 180 and 280 meV, respectively, from the bottom edge of the Γ valley, as summarized in Figure 4.5a. On the other hand, it is shown in Figure 4.5a that electrons promoted from the SO band have only a few meV of kinetic energy.

Tight-binding calculation provide also the energy-resolved electron spin polarization P_S, plotted in the Figure 4.5b, which is defined in Eq. 2.4 described in Section 2.4, and has been evaluated by taking into account the spin up ($n_\uparrow$) and spin down ($n_\downarrow$) electronic population up to a given excess energy in the Γ valley. Calculations reported in Figure 4.5b indicate that the 90% of the small amount of electrons photogenerated from SO band in the zone center is spin-up polarized, while the transitions involving the topmost VB states cause a lowering of the positive spin polarization generated by the SO transitions. A negative sign for P_S is predicted for an excess energy larger than 180 meV and, indeed, the overall polarization evaluated integrating over the total spin

ensemble at the Γ valley turns out to be $P_S = -65\%$. It is useful to remember that spin-dependent selection rules described in Section 2.4 strictly hold at the Γ point, where initial and final states have a well-defined J_z quantum number [23]. In our case, the topmost VB states involved in the optical orientation process feature relevant J_z mixing, due to both strain and excess pump energy. For this reason, the character of the states are not pure HH and LH eigenstates: the first (V1) and the second (V2) topmost out-of-zone-center VB states contribute both in populating the spin-down state in CB, as illustrated in Figure 4.5b.

Further information about the spin selection rules for the transitions out of the Γ valley can be found in Figure 4.5c. The quantity Θ, defined as [33]:

$$\Theta = \delta(\hbar\omega_p - E_{tr})|\vec{p} \cdot \hat{e_{\sigma+}}|^2 \langle S_z \rangle d^3k \tag{4.2}$$

represents the $\vec{k}$-resolved contribution to the non-equilibrium spin ensemble. k_z and $k_\parallel$ are respectively the component of the electron momentum along the light propagation direction z and lying in the xy plane parallel of the sample surface, E_{tr} is the transition energy, and $\langle S_z \rangle$ is the expectation value of the component of the spin operator along z evaluated for the CB states. Finally, $\vec{p}$ is the momentum operator and $\hat{e}_{\sigma+}$ is the polarization versor corresponding to the right-handed circular polarization. In line with the above discussion, we find that SO electrons (1), characterized by a small momentum, are described by a positive value of Θ (red color in map of Figure 4.5), which stems from spin up electrons. Transitions 2 and 3, involving V1 and V2, are clearly distinguishable at larger k values in the $(k_\parallel, k_z)$ plane, and present a strong mixing of the main orbital symmetry character. Where the character is HH-like, the quantity Θ has negative values (blue color in Figure 4.5c) and the corresponding spin of the electron results to be down, while the LH-like character of the states is characterized by positive Θ value.

Despite the calculated polarization of the injected carriers has a negative total value, the helicity of the $c\Gamma - LH$ and $c\Gamma - HH$ PL features unambiguously demonstrates that the spectra are dominated by the recombination of spin up electrons, pointing out the role of small momentum electrons in determining the overall ρ of the radiative recombination across the direct gap [33]. Above all, the steady-state spin population, which results from the relaxation of the photogenerated carriers due to both intervalley scattering in the CB and the radiative and non-radiative recombinations, may significantly differ from the calculated photogenerated distribution shown in Figure 4.5b. The reason of this has to be found in the rich dynamics of CB electrons in Ge. The striking agreement between the PL polarization of + 85% measured for the

fundamental transition in i-Ge and the predicted spin polarization of + 90% for the subset of electrons photogenerated from the SO band demonstrates that the circular polarization degree of the direct gap PL echoes the SO-like spin population as given by optical selection rules right after excitation, since electron spin relaxation mechanisms take place on a time scale [16] much longer than the lifetime at the Γ valley [35,36]. This also corroborate the previous results for bulk unstrained Ge, reported in Ref. [25, 126]: only radiative transitions across the direct gap with a very small electron momentum are active, since at the adopted excitation density and doping levels, the quasi-Fermi level in the VB of intrinsic Ge is of the order of 10 meV, which corresponds to active transitions with a conduction excess energy of less than 100 meV. The Γ-valley electrons with a large kinetic energy are more effectively scattered out of the Γ valley into lower energy Δ and L satellite valleys, finally suppressing their contribution to the radiative recombination events across the direct gap.

In addition to the spin-selective dwell of electrons at the Γ valley, it is worth noting that biaxial tensile strain is ultimately beneficial for the achievement of high ρ in Ge-on-Si heterosystems. As opposed to the relaxed bulk case, strain lifts the LH/HH degeneracy, leading to a spectral separation of photons emitted with opposite helicity *via* the otherwise interfering $c\Gamma - LH$ and $c\Gamma - HH$ transitions.

This matching between the measured ρ and the calculated P_S, along with the highly mixed spin states expected for the photogenerated hole ensemble, strongly suggest that holes participating in the radiative recombination events can be assumed to be unpolarized. Although no direct measurement is provided for the spin relaxation time of holes, it can be inferred, in light of the above discussion, that is should be shorter than the intervalley scattering time in the CB, *i.e.* in the hundreds-of-fs time range [45, 67].

In the following sections we provide a study of the polarization of direct-gap emission of Ge-on-Si as a function of doping and temperature, to gather a better understanding of the non-trivial spin properties of tensile-strained Ge.

4.3.2 Doping effect on spin polarization

The low temperature direct gap PL of 9223-F5 n-doped sample (n-Ge) and 9261-F5 p-doped sample (p-Ge) are reported in Figure 4.6a and b, respectively. We recall that the two samples have the same level of doping concentration, that is $4.5 \cdot 10^{17} \text{cm}^{-3}$, as listed in Table 4.1. As in Figure 4.3, the upper panels of Fig. 4.6 show the color-coded maps of the PL intensity as a function of the analyzer angle, while the lower panels report the spectra at the analyzer angles of 45° (black curve) and 135° (red curve), corresponding to σ_- and σ_+ circularly polarized PL, respectively.

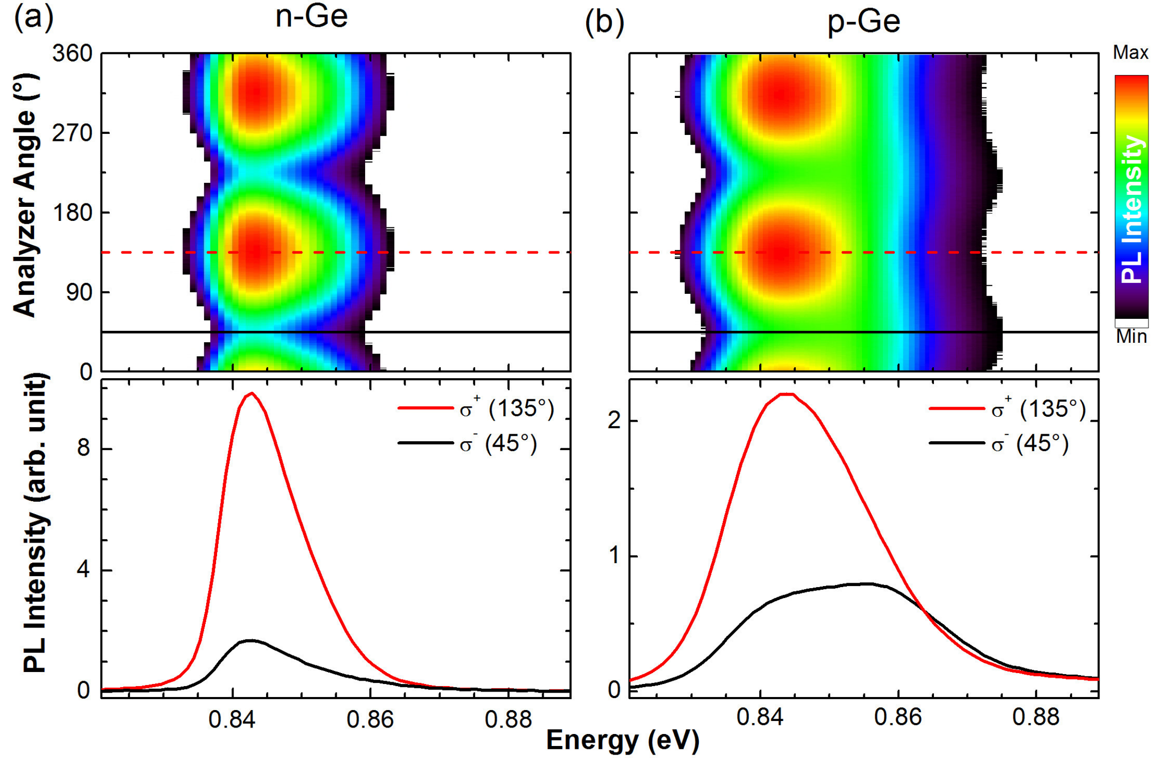

Figure 4.6: Upper panels: Color-coded intensity maps of the PL measured as a function of the analyzer angle at 4 K in tensile-strained (a) n-Ge and (b) p-Ge. Lower panels: 4 K PL spectra of (a) n-Ge and (b) p-Ge corresponding to σ_- (analyzer angle at 45°, black solid line) and σ_+ (135°, red dashed line) polarization components.

In n-Ge PL spectra shown in Fig. 4.6a, one well-defined PL peak can be observed with a maximum at 0.843 eV. Its energy position is consistent with the shrinking of the band gap with respect to i-Ge shown in Figure 4.3, caused by the contributions of doping [127]. The polarization analysis reveals a $\rho = 70 \pm 1\%$, which is lower with respect the intrinsic case. Above all, there is no evidence of the recombination due to the $c\Gamma - HH$ transition. On the contrary, the p-Ge spectra shown in Figure 4.6b point out a broader PL peak, with a polarization degree $\rho = 48 \pm 1\%$. Yet, the polarization analysis allows us to distinguish two cross-polarized contributions at 0.843 eV and at about 0.86 eV. Notably, the higher energy feature is more pronounced than the intrinsic case illustrated in Figure 4.3, suggesting that the acceptor concentration is effective in populating the energetically unfavoured HH states.

To confirm this results, we have carried out a systematic polarization-resolved PL study as a function of p-type doping. Figure 4.7 shows the PL maps and spectra measured at 4 K of Ge-on-Si samples with an increasing acceptor concentration. As expected, there is a redshift of the peak position due to doping-induced band-gap narrowing and an overall enhancement of the PL intensity with the B content [25, 127]. However, the σ_+ and σ_- PL spectra shown in Figure 4.7 point out an increasing of the

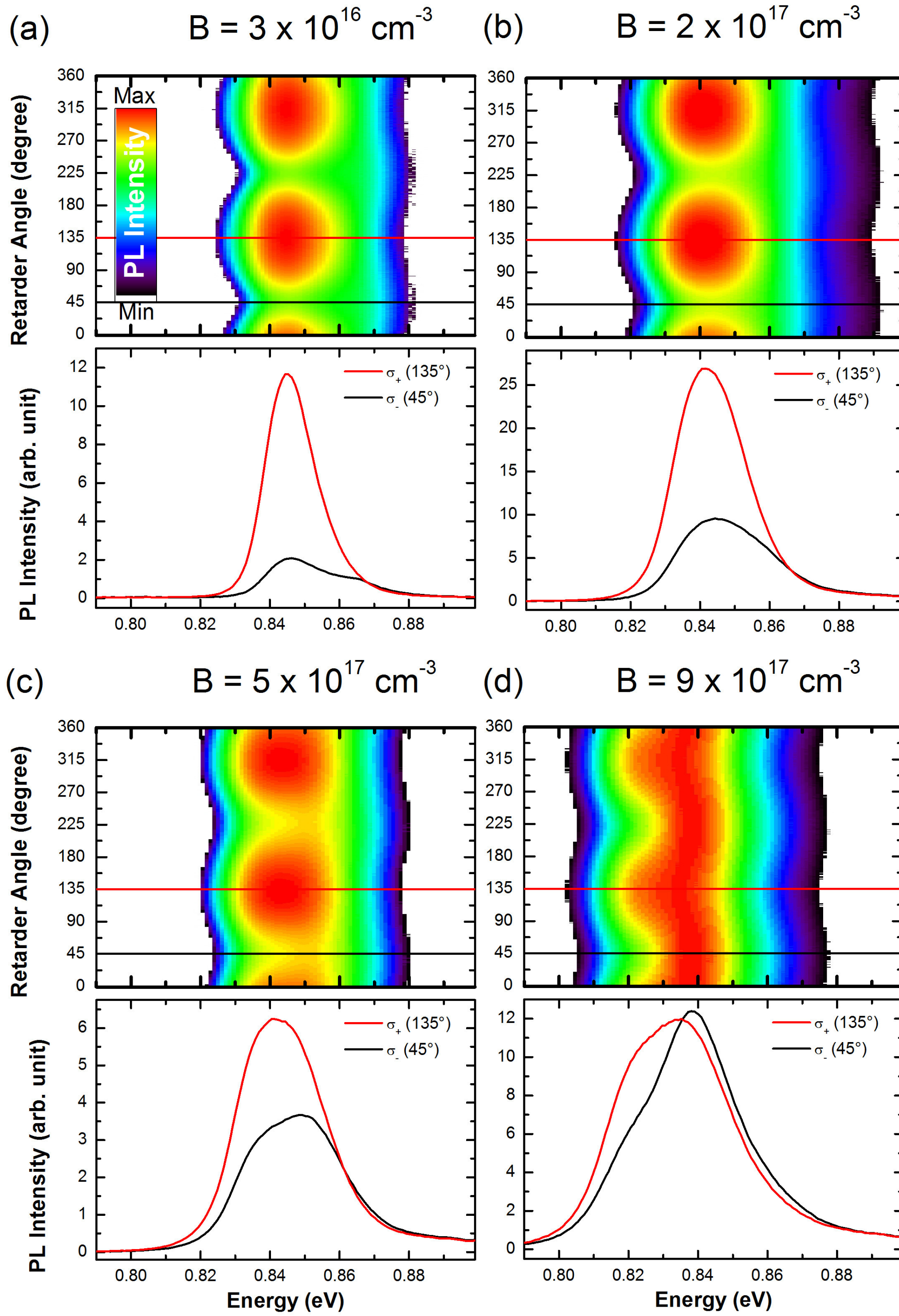

Figure 4.7: Upper panels: Color-coded intensity maps of the PL measured as a function of the analyzer angle and PL spectra corresponding to σ_- (analyzer angle at 45°, black solid line) and σ_+ (135°, red line) polarization components at 4 K of tensile-strained *p*-doped Ge-on-Si with different boron content: (a) $3 \cdot 10^{16}\text{cm}^{-3}$ (sample 8869-E6), (b) $2 \cdot 10^{17}\text{cm}^{-3}$ (sample 8871-E6), (c) $5 \cdot 10^{17}\text{cm}^{-3}$ (sample 8872-E6) and (d) $9 \cdot 10^{17}\text{cm}^{-3}$ (sample 8870-E6).

Sample name	B concentration (cm^{-3})	Polarization degree ρ (%)
8869-E6	$3 \cdot 10^{16}$	70 ± 1
8871-E6	$2 \cdot 10^{17}$	48 ± 1
8872-E6	$5 \cdot 10^{17}$	26 ± 1
8870-E6	$9 \cdot 10^{17}$	-2 ± 1

Table 4.2: Polarization degree of Ge-on-Si as a function of p-doping content at 4K.

cΓ – HH transition spectral weight, and the polarization degree of the emission, listed in Table 4.2, decrease by increasing B content. The high energy HH transition becomes dominant for the highest boron content, $9 \cdot 10^{17} cm^{-3}$, and results in an overall peak circular polarization that is counterpolarized with respect to the laser excitation (*i.e.* $\rho = -2 \pm 1\%$).

Indeed, the Fermi level shifts deeper in the VB by increasing the density of extrinsic holes, thus providing access to lower energy electron states and causing a rise of the population of the HH band, which is optically coupled to spin up electrons by the emission of σ_- photons.

This data on doped samples supports the physical picture leading to the PL polarization discussed in the previous Section. Indeed, backscattering of high energy electrons from the satellite Δ valleys towards the zone center can be strongly enhanced by Coulomb interactions with doping-induced charges [25, 126]. This mechanism is known to result in doping-related changes of the PL polarization due to an increased accumulation at the edge of the Γ valley of the spin down electrons originally photogenerated from the V1 and V2 states [25, 33, 126]. Consistently with this mechanism, we measured ρ values for the fundamental transition that in n-Ge and p-Ge are smaller than in the less doped i-Ge.

4.3.3 Temperature effect on spin polarization

We performed polarization-resolved CWPL measurement on i-Ge, n-Ge and p-Ge as a function of the temperature. Figure 4.8a shows the polarization degree ρ of the i-Ge direct gap PL emission as a function of the temperature. It is worth noting that the polarization degree monotonically decreases by increasing the temperature, and vanishes at about 150 K. The emitted light is not circularly polarized above this temperature, *i.e.*, the electron spins are no longer oriented prior to recombination. We can therefore conclude that there exists a thermal activation of spin relaxation-mechanisms above 150 K, as observed already in bulk relaxed Ge [25]. The PL spectra for σ_+ and σ_- components measured at different temperatures are shown in Figure

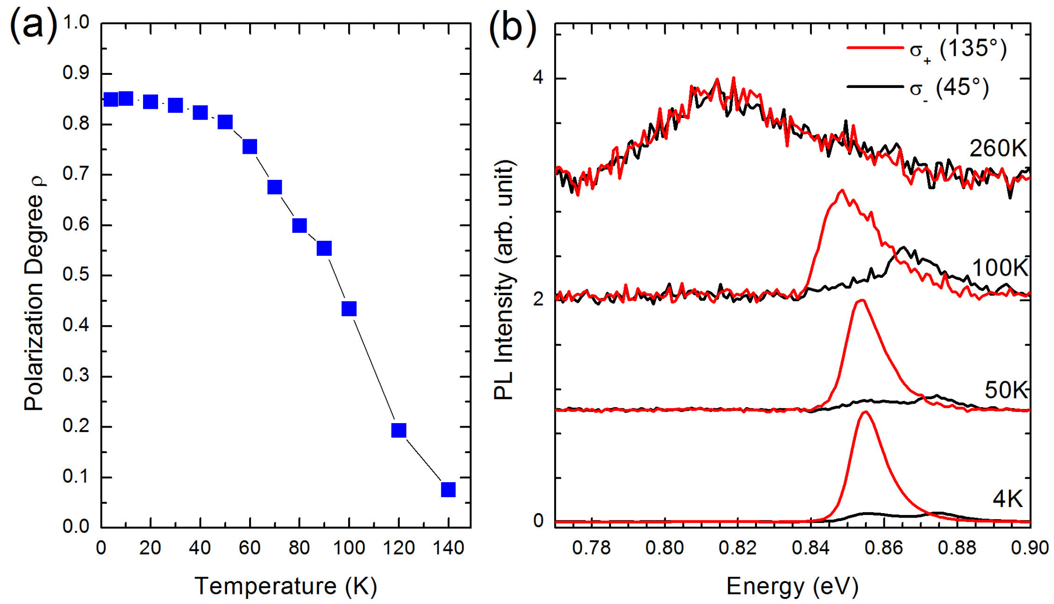

Figure 4.8: (a) Polarization degree of direct emission of i-Ge as a function of temperature. (b) PL spectra of σ_- (analyzer angle at 45°, black solid line) and σ_+ (135°, red line) polarization components at 4, 50, 100 and 260 K of i-Ge.

4.8b and point out a broadening of the spectral structures by increasing the temperature. This effect combined with the vanishing polarization degree does not allow us to resolve the two $c\Gamma-LH$ and $c\Gamma-HH$ contribution in the high temperature regime.

A similar behaviour is observed for n-doped Ge-on-Si, as summarized in Figure 4.9: the polarization degree of the n-Ge direct emission decreases with the temperature, vanishing again at about 160 K (Figure 4.9a). Remarkably, above 50K, the polarized-resolved analysis of the direct emission points out the existence of high energy $c\Gamma-HH$ PL feature, as illustratedi in Figure 4.9b.

This result underlines how temperature, like doping, can play a role in modifying the occupation of the available hole states, eventually changing the spectral weight between $c\Gamma-LH$ and $c\Gamma-HH$ even for n-doped sample [33]. This suggest the possibility to observe an inversion in spectral weight between the fundamental $c\Gamma-LH$ and the higher energetic transition $c\Gamma-HH$ by changing the temperature in properly doped samples. The study of polarization-resolved direct gap PL of the p-Ge sample confirm this hypothesis, as shown in Figure 4.10. As described above, the low p-doping content provide a polarization degree of the direct recombination at 4 K of about +47%. By increasing temperature, as shown in Figure 4.10a, the polarization degree ρ of the broad PL peak (black triangles) decrease with increasing temperature and, above 140 K, it changes its sign. Moreover, in contrast to the i-Ge and the n-Ge samples, the polarization, albeit very small, is not vanishing up to 280 K.

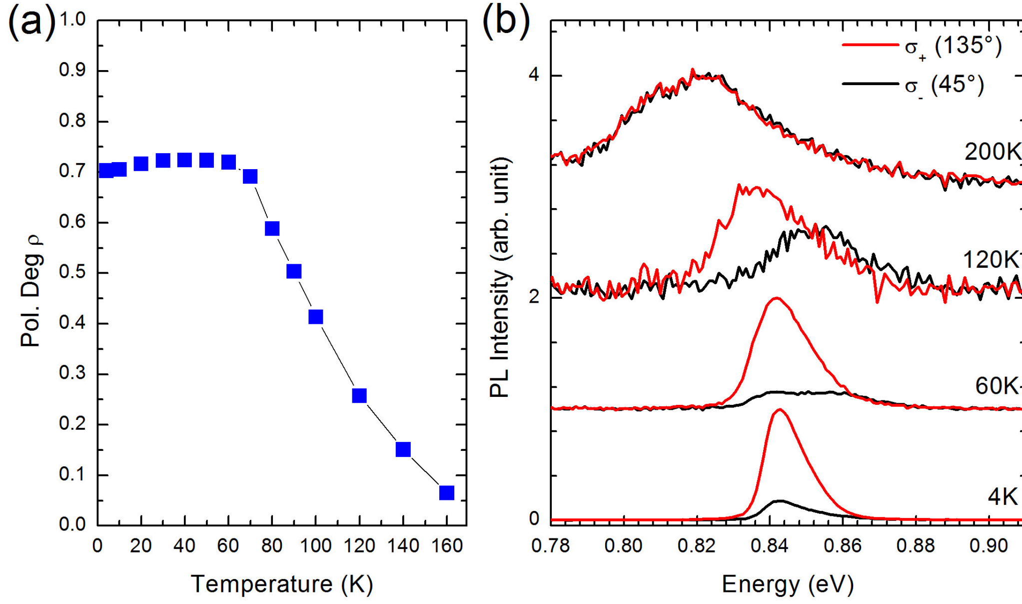

Figure 4.9: (a) Polarization degree of direct emission of n-Ge as a function of temperature. (b) PL spectra of σ_- (analyzer angle at 45°, black solid line) and σ_+ (135°, red line) polarization components at 4, 60, 120 and 200 K of n-Ge.

To gain a better understanding of the change of the ρ sign, it is useful to calculate the polarization degree for the $c\Gamma-LH$ and $c\Gamma-HH$ transitions, separately (blue squares and red circles in Figure 4.10a, respectively). The spectral resolution of the two transition allow us to observe that the reverse of the polarization helicity from σ_+ to σ_- is an indication of the dominance of the $c\Gamma-HH$ transition in the high temperature regime. This is demonstrated also by the PL spectra at various temperature reported in Figure 4.10b. We point out, moreover, that at the temperature of 135 K, the difference in intensity between the σ_+ and σ_- PL component gives a ρ equal to zero (black triangles in Figure 4.10a). However, this null value does not stem from unpolarized light emission, but it is the superposition of equal contribution of σ_+ and σ_- intensity.

This is further demonstrated in Figure 4.10c, which shows the modulation pattern of the PL intensity measured in p-Ge at 135 K. The Stokes analysis allows us to unfold the similar intensity of the $c\Gamma-LH$ and $c\Gamma-HH$ transitions [33]. At this temperature, the thermal energy, which corresponds to 12 meV, is quite close to the energy separation between LH and HH at the Γ point at this temperature (about 15 meV).

As shown in Figure 4.10b, the PL peak become broadener by increasing the temperature and, above 200 K, the two components merge into a single, broad line. The measured PL peak positions for the σ_+ and σ_- polarization-resolved spectra as a function of the temperature are summarized in Figure 4.11. Below 200 K, the σ_+ and σ_-

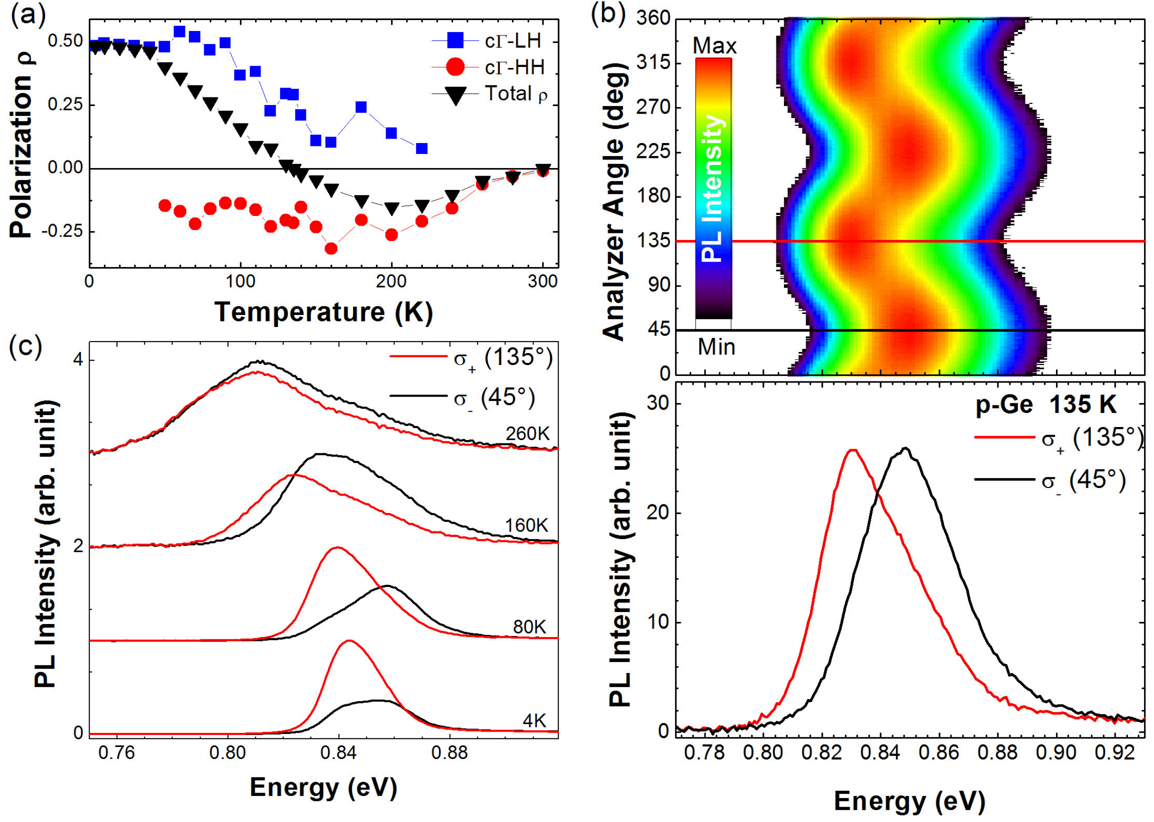

Figure 4.10: (a) Polarization degree of cΓ − LH (blue square dots) and cΓ − HH (red circle dots) direct emission of p-Ge as a function of temperature. The black triangles stem from the polarization degree of the whole PL peak. (b) PL spectra of σ_- (45°, black solid line) and σ_+ (135°, red line) polarization components at 4, 80, 160 and 260 K of p-Ge. (c) Color-coded map as a function of the analyzer angle (upper panel) and corresponding σ_- (45°, black solid line) and σ_+ (135°, red line) PL spectra measured at 135 K in p-Ge (bottom panel).

peak positions agree well with the expected cΓ − LH and cΓ − HH transition energies, respectively (solid lines in Figure 4.11). To obtain the cΓ − LH and cΓ − HH transition energies as a function of the temperature, we consider the Varshni's empirical equation [37] for the band-gap changes due to the temperature. The PL peak maximum of a direct transition is blue-shifted with respect to the bandgap by an amount equal to k_BT/2 [48]. The thermal-related strain shift is thus evaluated by adding a linear dependence E(ε(T)) [70], where $\varepsilon(T)$ is obtained by solving the integral of Eq. 3.6 reported in Section 3.1. The energy shift E(ε(0K)) are different for HH and LH states and are calculated by Equations 3.4 in Section 3.1. Finally, the Varshni-like equations for the doped samples are rigidly red-shifted of the same energy amount due to doping-induced band-gap narrowing [127]. The final equation has the following form:

$$E_\Gamma(T) = E_\Gamma(0K) + \frac{\alpha\, T^2}{\beta + T} + E(\varepsilon(T)) + \frac{1}{2}\, kT \tag{4.3}$$

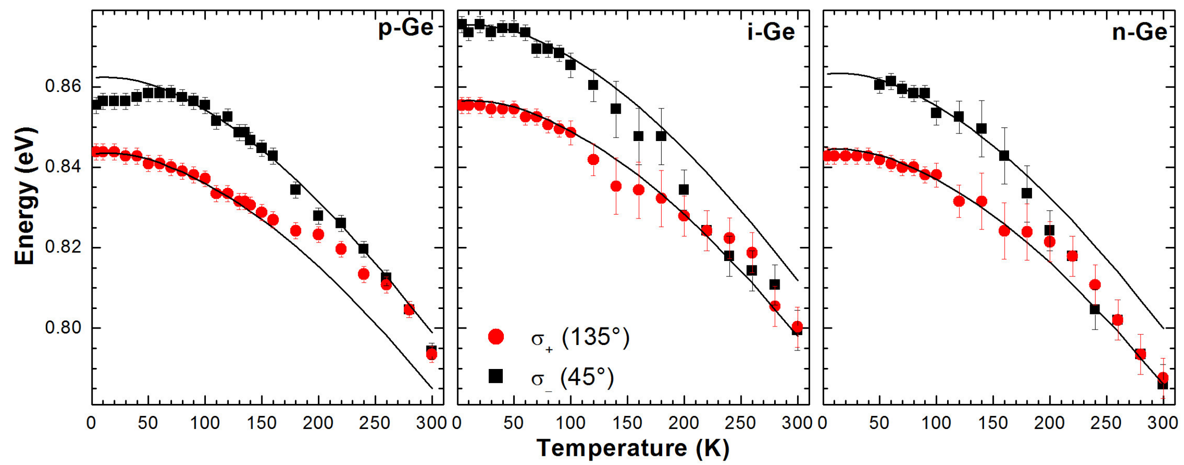

Figure 4.11: Temperature dependence of the PL peak positions resolved for the σ_+ (red circled dot) and σ_-(black squared dot) components of the emission of p-Ge (left panel), i-Ge (middle panel), and n-Ge (right panel). The solid lines account for the expected $c\Gamma - LH$ and $c\Gamma - HH$ transition energies owing to the corresponding temperature [37], strain [70], and doping [127] contributions.

Figure 4.11 compares the peak positions for the σ_+ and σ_- PL components of p-Ge (left panel), i-Ge (middle panel) and n-Ge (right panel) in the 4-300 K range. It is worth noting that in p-Ge, above 200 K, the σ_+ data collapse on the higher energy component of the doublet, thus corroborating the result described above, in which the cΓ – HH recombination dominates the PL spectrum of p-Ge in the high temperature regime [33]. Remarkably, Fig. 4.11 demonstrates that, as opposed to *p*-doped Ge-on-Si, cΓ – LH provides the main contribution to the high temperature PL of i-Ge (middle panel) and n-Ge (right panel). Even though above 200 K the PL of these two samples becomes not circularly polarized, the peak positions are fully consistent with the lower energy cΓ – LH component of the doublet. Such a finding unravels the relative role of LH and HH occupancy in determining the PL spectral shape of tensile-strained Ge. This has been largely neglected in previous literature works [91, 92, 128], although it has a crucial importance for the precise evaluation of optical gain in Ge [92].

5

Ge/SiGe Quantum Wells

The samples of Ge/$Si_{1-x}Ge_x$ multiple quantum wells (MQWs) with Ge-rich barriers (x = 0.85) analysed in this Chapter are characterized by the structure schematically shown in Figure 5.1a.

A graded virtual substrate (GVS), whose Ge composition varies from 0% to 90%, is deposited on a Si substrate. The GVS in then capped with a 2 μm thick $Si_{0.10}Ge_{0.90}$ relaxed layer. This buffer constitutes the relaxed substrate upon which strained-compensated quantum wells and barrier are grown. The active part of the structure consists of 500 Ge QWs separated by $Si_{0.15}Ge_{0.85}$ barriers. Finally, a 40 nm $Si_{0.10}Ge_{0.90}$

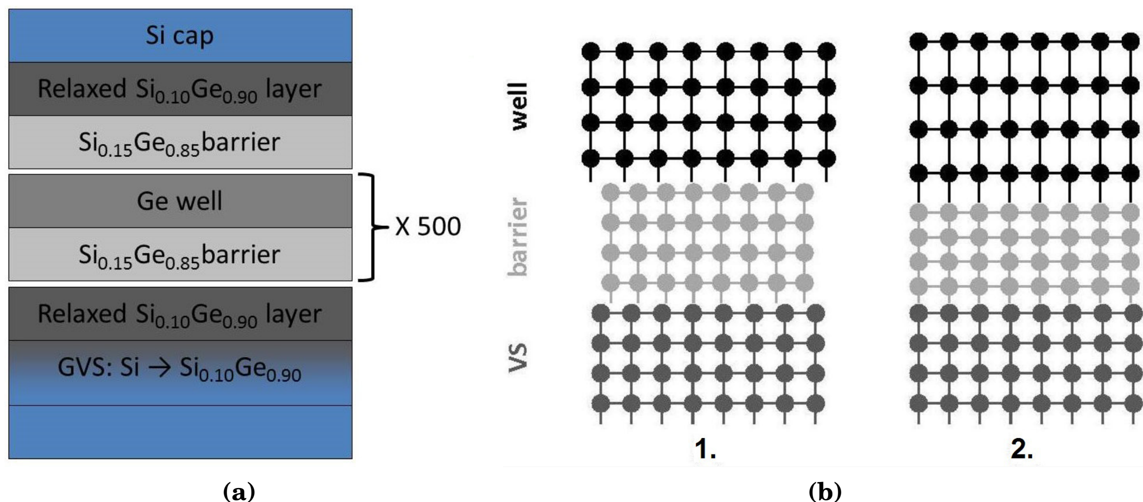

Figure 5.1: (a) Sketch of the structure of the Ge/$Si_{0.15}Ge_{0.85}$ Multiple Quantum Wells sample investigated in this thesis. (b)1. SiGe lattice parameter depends on alloy composition. 2. Strain balanced heterostructure pseudomorphic to the relaxed $Si_{0.10}Ge_{0.90}$: the tensile strain in $Si_{0.15}Ge_{0.85}$ barriers is compensated by the compressive strain in Ge wells.

Sample name	Doping type	Doping content (cm^{-3})	Well thickness W (nm)
8930-F8	undoped	-	20 ± 1
8931-F8	n-mod	$\sim 5 \cdot 10^{16}$	20 ± 1
8931-F4	n-mod	$\sim 6 \cdot 10^{16}$	17 ± 1
8931-H5	n-mod	$\sim 6 \cdot 10^{16}$	16 ± 1

Table 5.1: Ge/$Si_{0.15}Ge_{0.85}$ samples analyzed.

layer and a 10 nm Si cap are grown on the top of the stack. Despite the high number of periods, the analyzed samples present a good structural quality, as discussed in Ref. [31]. This is possible mainly because of two factors: the introduction of the GVS and the strain balance in the active part of the structure.

The GVS reduces the effect of the lattice mismatch between the Si substrate and the Ge-rich layers, yielding to a threading dislocation density of about $4-5 \cdot 10^6$ cm^{-2} in the topmost relaxed $Si_{0.10}Ge_{0.90}$ layer [129]. The strain compensation allows to keep the mean strain in the active layer equal to 0, preventing strain relaxation through formation of new dislocations. For this reason, the value of $4-5 \cdot 10^6$ cm^{-2} can be reasonably assumed to characterize also the active part of the MQWs structure. This value is two orders of magnitude lower than the typical threading dislocation density of Ge layers directly grown on Si [130].

As a matter of fact, in order to adapt their lattice parameter to that of the relaxed $Si_{0.10}Ge_{0.90}$ layer (pseudomorphic growth), wells and barriers experience compressive and tensile strain, respectively. In other words, the mean lattice parameter of a period, well plus barrier, has to be equal to that of the relaxed layer at the top of the GVS, as sketched in Figure 5.1b. The lattice parameter and the thickness of wells and barriers, respectively, satisfy the following relation:

$$a_S = \frac{d_W \cdot a_W + d_B \cdot a_B}{d_W + d_B} \tag{5.1}$$

where d is the layer thickness, a is the lattice parameter, while W, B and S refer to well, barrier and substrate, respectively.

The well thickness and dopants content of each sample presented in this Chapter are listed in Table 5.1. The samples were grown at the L-NESS centre of Como (Italy) *via* low-energy plasma-enhanced chemical vapor deposition (LEPCVD), an epitaxial growth technique based on a chemical deposition process, enhanced and activated *via* a high-intensity and low-energy plasma [119]. LEPCVD technique is characterized by high growth rate and a good control of the deposition thickness and the interfaces roughness. LEPECVD is a well suited tool for the epitaxial growth of high quality

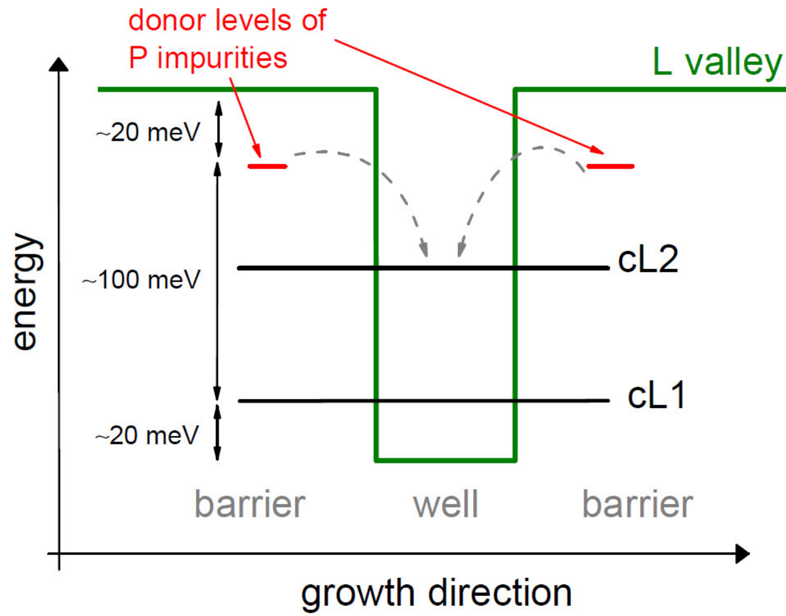

Figure 5.2: Sketch of the conduction band energy profile and electronic levels in a 10 nm modulation n-doped Ge/$Si_{0.15}Ge_{0.85}$ QW at the L point of the Brillouin zone.

500-fold stack Ge QW. Further informations about the growth technique are given in Appendix B. The thickness of the deposited layers is non uniform across the wafer, due to inhomogeneity in the intensity of the plasma. As described in details in Appendix B, each sample is identified with two numbers: the first refers to the wafer, and the second indicates the position of the sample across the wafer.

Two different kind of samples are analyzed: a nominally undoped 8930-F8 sample and a set of modulation n-doped (n-mod) 8931 samples. Modulation doping provides the spatial separation of the carriers from the impurities and has been obtained by depositing one monolayer of P atoms in all the $Si_{0.15}Ge_{0.85}$ barrier layers, at half of the barrier thickness. P atoms are shallow donors in SiGe alloys, with ionization energies ranging from 13 meV in Ge to 45 meV in Si [131, 132]. Due to the low confinement energy of the first confined L state, the donor level in the barrier has an energy higher than the cL1 and cL2 states in the QW layer (Figure 5.2) favoring donor electron transfer to the confined L states of the QW. The electrons transferred in the QW layer stay in the fundamental L minimum of the conduction band, and constitute a two-dimensional electron gas (2DEG). Further details about modulation doping and its effects on the band energy profile are given in Ref. [133].

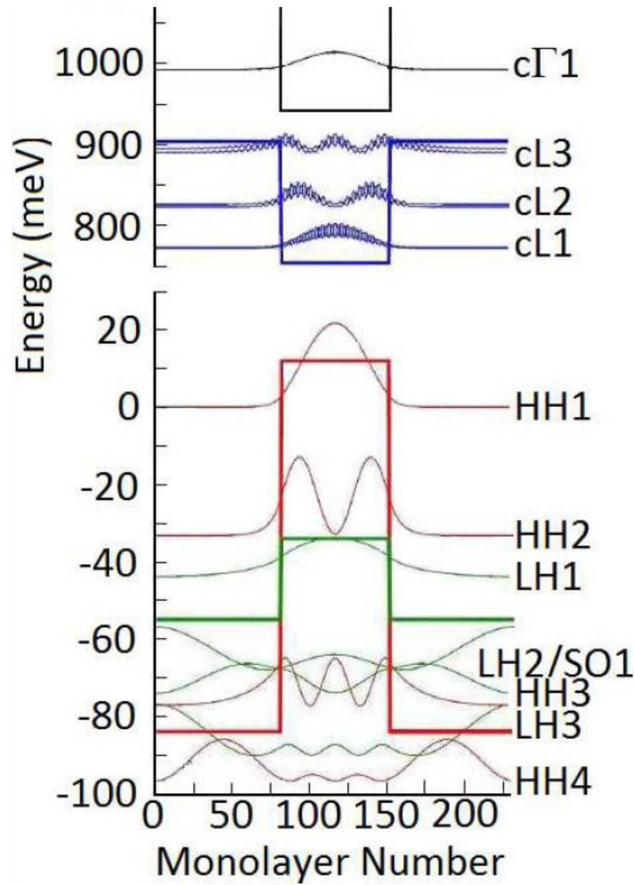

Figure 5.3: Calculated band offsets and square modulus of the wavefunctions of electron and hole confined states in a 10 nm thick Ge/$Si_{0.15}Ge_{0.85}$ QW [31]

5.1 Heterostructure and band alignment

The low temperature band alignment has been obtained by M. Virgilio and G. Grosso for Ge/$Si_{0.15}Ge_{0.85}$ MQWs grown on $Si_{0.10}Ge_{0.90}$ VS through tight binding calculations [31]. They predicted a type I band alignment for both the fundamental indirect and the direct gaps.

A schematic representation of the energetic levels and the square modulus of the wavefunctions, obtained from the tight binding calculation for a 10 nm thick Ge QW with 23 nm thick $Si_{0.15}Ge_{0.85}$ barriers, are reported in Figure 5.3 [31].

The L minimum of the CB in the Ge well is lower in energy with respect to the one of the $Si_{0.15}Ge_{0.85}$ barriers. At the same time, the VB maximum in the Ge well is higher in energy with respect to the one of the barriers. These offset values give the type-I band alignment for the indirect gap of the Ge QWs. Notably, both electrons and holes are confined in the same spatial region, *i.e.* in the Ge layer. The type I band alignment has been experimentally proved in Ref. [31, 113].

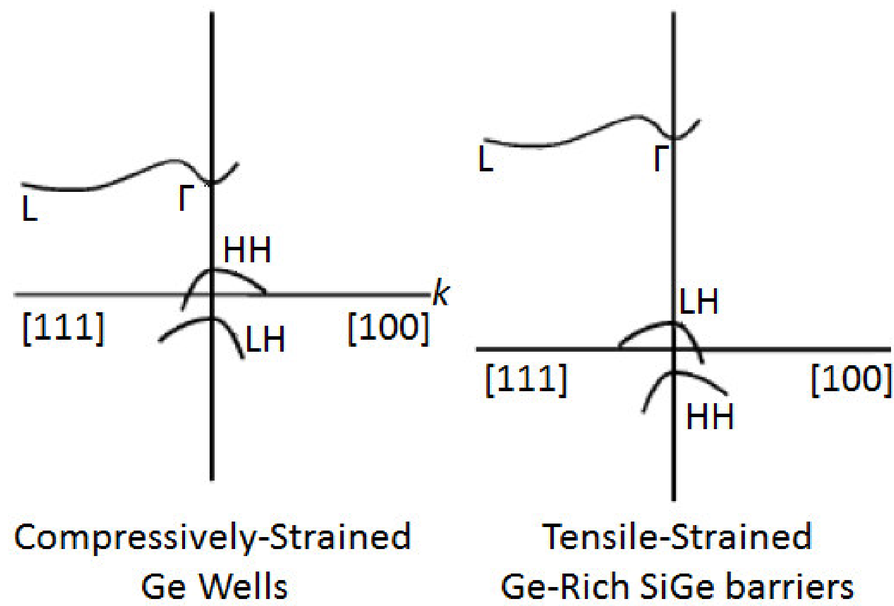

Figure 5.4: Sketch of the band structure of <001>-oriented compressively strained Ge wells (a) and tensile-strained barriers (b) [134].

The band offset for the L minimum is about 150 meV, while for the Γ valley conduction minimum it is about 400 meV. L and Γ conduction levels are labeled by cLn and cΓn, respectively, while HHn, LHn and SOn indicate heavy holes, light holes and split-off confined states. It is worth noting that the HH and LH levels in the well and in the barrier layers are not degenerate. Since the Ge well experiences a compressive strain while $Si_{0.15}Ge_{0.85}$ barriers are slightly under a tensile strain, there is a character inversion between the top of the VB in well and barrier regions (Figure 5.4). In fact, in the well (barrier) region the top of VB has a HH (LH) character.

Finally, it should be noted that the wavefunctions corresponding to the n = 1 states are almost completely confined within the well region while, as n increases, also the wavefunction penetration within the barrier region is larger, so that carriers confinement decreases [31].

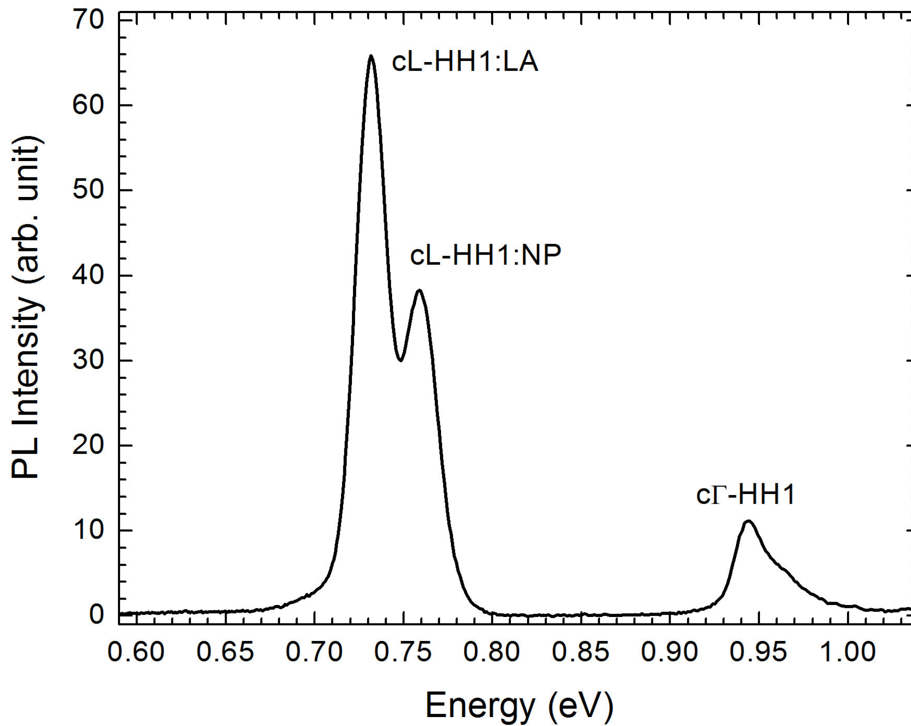

Figure 5.5: PL spectrum of Ge/$Si_{0.15}Ge_{0.85}$ MQWs at T = 4K under continuous-wave (CW) laser excitation at 1.165 eV. Phonon mediated and no-phonon line of indirect transition cL-HH1:LA and cL-HH1:NP and direct transition $c\Gamma - HH1$ are shown.

5.2 Optical properties

In this section, we discuss the optical properties of undoped 8930-F8 sample of Ge/ $Si_{0.15}Ge_{0.85}$ MQWs heterostructures. The thickness of wells and barriers, obtained by means of X-Ray diffraction measurements, are d_W = 20 nm and d_B = 21 nm. The continuous-wave (CW)PL spectrum of the sample measured at 4 K is shown in Figure 5.5. The sample was excited by means of a Nd : YVO_4 laser, having a 1.165 eV emission energy and a power density of 4.8kW/cm^2. The description of the experimental set-up is presented in Appendix A.

The spectrum exhibits three well resolved features. The one at the highest energy stems from the direct-gap emission ($c\Gamma - HH1$). It is worth noting that the 1.165 eV excitation is almost resonant with the direct gap transition in the Ge wells (Figure 5.4). As a result, electrons are photoexcited directly in the Γ valley of the QWs. As already mentioned, in Ge QWs biaxial compressive strain and confinement remove the degeneracy between HH and LH at the Brillouin zone center. The top of the valence

band is thus HH-like, and the electron population generated from HH and LH bands changes with respect to the bulk case [108]. Strain and confinement act also on the SO band, so that in Ge QWs the energy of the transition between the SO band and the Γ states in CB is much larger than the excitation energy. Photogenerated electrons in the Γ valley of the QWs are scattered to L valleys on a sub-picoseconds timescale [32, 123]. In this short time, few electrons can recombine radiatively from the Γ states of the CB with holes in the HH states of the VB.

The two PL peaks at lower energy can be ascribed to the zero-phonon line of the indirect transition between the first confined CB state at L (cL1) and the HH1 VB state (cL-HH1:NP) and its longitudinal acoustic (LA) phonon replica (cL-HH1:LA).

The observation of the NP line in Ge/$Si_{0.15}Ge_{0.85}$ MQWs is justified considering two different mechanisms related to the roughness of the interface between the wells and the barriers: (i) irregularities of the interfaces can act as scattering centres for excitons, providing to the electrons in the L states the required momentum to recombine with holes at Γ [115, 135], and (ii) the QW thickness fluctuations localize excitons in regions of lower potential, thus providing a delocalization of electrons and holes in the k-space [136]. This results in a non-zero probability to observe the no-phonon line emission [114].

It is worth to emphasize that both direct and indirect transitions are distinguishable in the same PL spectra, differently from the Ge-on-Si case presented in Chapter 4. This is due to the presence of the GVS. As described at the beginning of this Chapter, no plastic relaxation occur in the Ge/SiGe active layers, due to the strain balance with respect the relaxed $Si_{0.10}Ge_{0.90}$ buffer layer.

On the basis of the calculated band structure summarized in Figure 5.3, the energy distance between the HH1 and LH1 states is expected to be of about 40 meV. However, no evidence is experimentally found in the PL spectra of the indirect cL1-LH1 transition, involving the first LH confined valence state. This may be due to the weak oscillator strength of the transitions involving LH bands. Indeed, the ratio of the probability of $c\Gamma1-LH1$ and $c\Gamma1-HH1$ direct transitions is one third and a similar behaviour may be reasonably assumed for the cL1-LH1 and the cL1-HH1 transitions. Furthermore, the different effective mass value of HH and LH valence states favours the recombination on HH states. This may account for the lack of the cL1-LH1 transition in the PL spectrum.

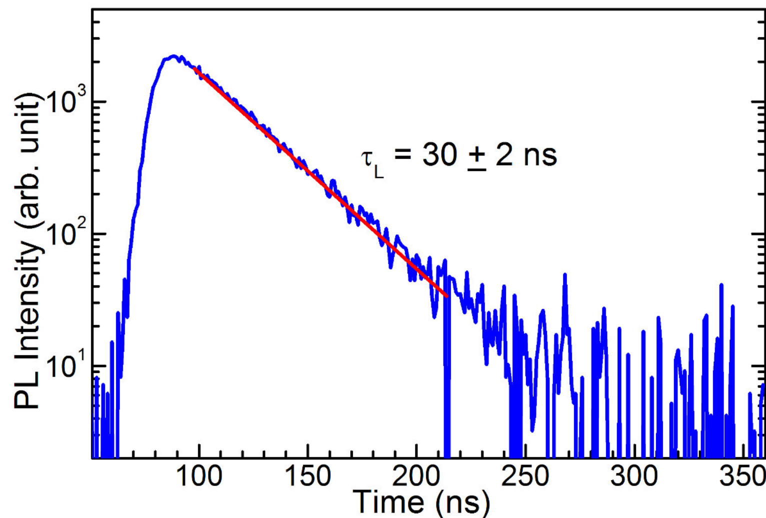

Figure 5.6: Low temperature decay curve obtained for the NP-line at 0.756 eV of the sample 8930-F8 Ge/$Si_{0.15}Ge_{0.85}$ MQWs under 1.165 eV pulsed excitation.

Decay time

We focus now on the decay time of the PL of Ge/SiGe MQWs. In case of indirect transitions, the radiative recombination can occur through different mechanisms, such as phonon participation or scattering with interface roughness; as described above, the latter process is important for Ge/SiGe MQWs. Figure 5.6 shows a decay curve obtained for the zero-phonon cL1-HH1 transition at the energy of 0.756 eV and the temperature of T = 4 K for the sample 8930-F8. A single exponential decay is observed and, at this lattice temperature, a decay time of the order of 30 ns has been measured. Remarkably, this value results to be about three times longer than the ones reported in literature for similar structures [114]. The results presented in Ref. [114], and summarized in Figure 5.7a, show the decay time of a 200-fold stack Ge/$Si_{0.15}Ge_{0.85}$ MQWs at low temperature as a function of the well thickness L_z. The decay time increases from 6 to 13 ns as the QW thickness increases from 3 nm to 20nm-thick QWs [114]. Figure 5.7a also shows that for a given QW thickness, one can have different decay times in different samples. In their work [114], the authors suggests that this difference is related to the presence of defects. To confirm this finding, the authors analyzed the two low temperature CWPL spectra of two samples characterized by the same well thickness (7.3 nm) but different decay times. The result is summarized in Figure 5.7b. The solid line is the spectrum of the sample characterized by a longer decay time, whereas the dashed line is the spectrum of the sample characterized by a shorter decay time. In both spectra a peak at about 0.6 eV is present that has been attributed to transitions related to dislocations [114]. In the PL spectrum of the

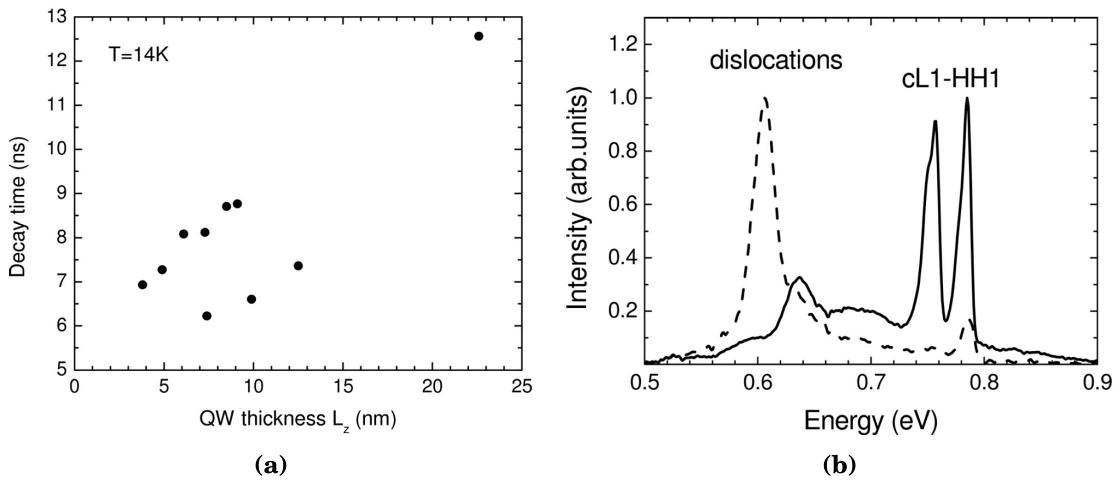

Figure 5.7: (a) Decay time of the zero-phonon cL1-HH1 transition as a function of the QW thickness L_z at the lattice temperature T = 14 K. (b) CWPL spectra at 5 K of two samples with the same well thickness (7.3 nm) and different decay times. The solid line refers to the sample with a longer decay time, and the dashed line to the other sample. Adapted from [114].

sample with a shorter decay time, the dislocation PL peak is brighter; this higher contribution of competitive recombination channels related to dislocations causes a reduction of the total lifetime of photoexcited carriers. As shown by CWPL spectrum of 8930-F8 sample in Figure 5.5, no emission due to dislocation is observed in the 0.6 eV spectral range. The decay time of 30 ns measured in this thesis (Figure 5.6), can thus be accounted for the good quality of the analyzed sample.

The decay time of the LA replica (not shown) reproduces that obtained for the NP line, as expected. Indeed, decay time measures the depletion rate of the excited state involved in the transition, regardless of the different mechanisms that contribute to the depletion. Consequently, no difference is expected between the decay time of the LA replica and of the zero-phonon emission, since the same initial and final states are involved.

5.3 Spin properties of Ge/SiGe MQWs

In this section we present polarization-resolved PL measurement of the undoped sample 8930-F8 (Table 5.1), carried out in backscattering geometry. We achieve optical spin orientation through absorption of photons carrying angular momentum. The selection rules for electric dipole interband transitions with circularly polarized light allow the excitation of a non-equilibrium population of carriers in the vicinity of the Γ-point having a net spin orientation along the propagation direction of the optical beam. Incident light was right-handed (σ_+) circularly polarized. The polarization state of the emitted light was probed by means of a rotating quarter $\lambda/4$ waveplate followed by a linear polarizer.

5.3.1 Polarized-resolved CWPL

The CWPL spectra of Ge MQWs measured at 4 K are shown in Figure 5.8. The spectra have been measured by varying the retarder angle between the $\lambda/4$ and the linear polarizer, thus resolving to the σ_+ and σ_- intensity components (red and black spectra in Figure 5.8, respectively). A full description of the experimental set-up is given in Appendix A.

It is worth noting that the data reported in Figure 5.8 clearly point out a non-zero circular polarization ρ both for direct and indirect recombination, thus confirming the successful optical spin orientation. In particular, the $c\Gamma - HH1$ emission is co-polarized with respect to the excitation (σ_+) with a polarization degree of $(31 \pm 1)\%$.

The PL spectra of the Ge MQWs displays also the polarization of the indirect emission. The NP peak reveals a polarization degree of about $(5 \pm 1)\%$, and similarly the LA peak displays $\rho = (4 \pm 1)\%$. A co-polarized indirect-gap feature was reported in the literature for similar Ge/$Si_{1-x}Ge_x$ MQWs heterostructures [109]. This observation is a clear indication that the optically oriented spins withstand the ultrafast transfer to the L valleys and the dwell time of electrons in the L valleys before recombination. In Ge, the energy relaxation of the photoexcited holes, towards the centre of the Brillouin zone in the valence band, is accompanied by a quick spin depolarization occurring in a sub ps regime [109, 110]. On the other hand, ultrafast scattering events deplete the optically excited conduction band levels on a hundreds-of-fs time scale [109, 110]. Electrons transferred out of Γ will eventually accumulate at the bottom of the L-valley [25], where they reside for a few ns [114]. The electron spin polarization is notably not extinguished during such non-trivial processes. Rather, it governs the radiative recombination with the unpolarized hole-pocket at Γ, yielding circularly polarized PL

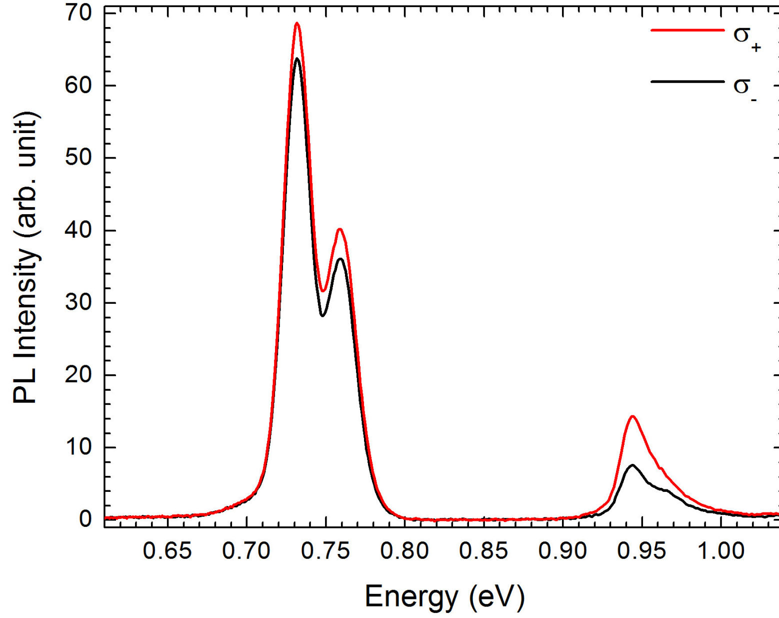

Figure 5.8: Low temperature polarization-resolved CWPL spectra of Ge/$Si_{0.15}Ge_{0.85}$ MQWs at excitation at 1.165 eV. Red (black) curve corresponds to σ_+ (σ_-) PL intensity component.

[109]. As mentioned above, the initial electron polarization at the Γ valley is 31%, so the smaller measured value for the indirect recombination (4%-5%) is likely due to the spin-relaxation mechanisms that electrons experienced in the L valleys.
To gain a deeper understanding of spin-relaxation mechanism in Ge MQWs, we have carried out polarization- and time-resolved (TR)PL measurements. The results are presented in the following section.

5.3.2 Spin-relaxation time by polarized-resolved TRPL

The time decay of the cL1-HH1 optical transition offers us the possibility to selectively access the spin dynamics of L-valley electrons. Figure 5.9 reports the intensity decay versus time of the NP line of the indirect PL emission at 0.756 eV. The PL was measured at 4 K under excitation with σ_+ circularly polarized light at 1.165 eV. In Figure 5.9, the co-circular (σ_+, grey dots) and counter-circular (σ_-, orange dots) emissions are reported, along with the corresponding fits. The different intensities of the two helicity-resolved PL components at the early stage of the recombination dynamics demonstrate the net circular polarization of the emission. This provides a measurement of the initial polarization degree ρ_0 of the indirect transition of about $(10 \pm 1)\%$. It is worth noting that the time-decay of the optically-induced non-equilibrium popu-

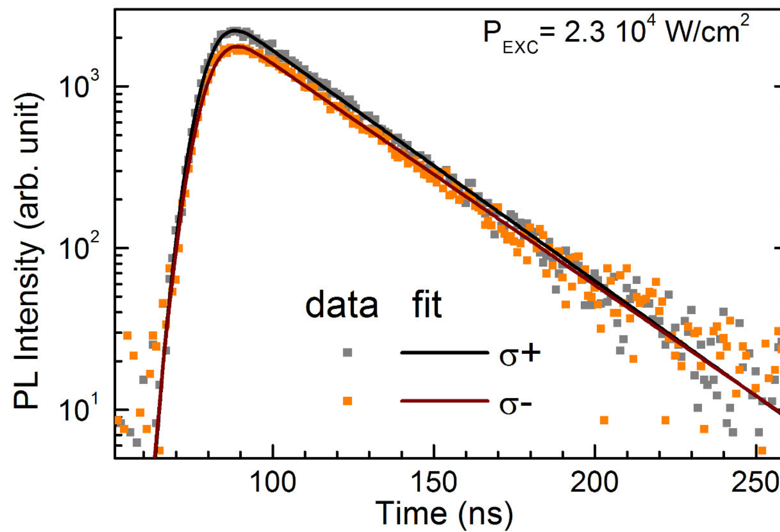

Figure 5.9: Low temperature polarization-resolved decay curves obtained for the NP-line at 0.756 eV of Ge/$Si_{0.15}Ge_{0.85}$ MQWs at excitation at 1.165 eV. Grey (orange) dots correspond to σ_+ (σ_-) PL intensity component, while the black and red solid lines are the exponential fits of the σ_+ and σ_- decay curves, respectively.

lation of the electron spins is reflected by the time-dependent depolarization of the PL. The latter can be described by a single exponential decay, providing a direct means to measure the spin-lattice relaxation time (T_1) [22]. The time dependence of the polarization degree of the PL is described as follows [23]:

$$\rho(t) = \rho_0 \, e^{-\frac{t}{T_1}} \tag{5.2}$$

By applying Eq. 5.2 to the data shown in Figure 5.9, we can derive the spin-relaxation time $T_1 = (120 \pm 10)$ ns.

This value compares well with recent reports on bulk Ge [42, 61]. As pointed out in Section 2.3, in this temperature regime, theory suggests a T_1 extending well above the μs range [49, 55]. Also, longer spin-relaxation time can be expected in low-dimensional structures, due to the effect of strain and confinement [24, 34]. To gather a better understanding of the dominant mechanisms leading to spin flip in our MQWs, we perform polarized-resolved TRPL measurement at different excitation power densities.

Power dependence of spin-relaxation time

Figure 5.10 reports the intensity decay *versus* time of the NP-line (0.756 eV) of the indirect PL emission for different pump powers. It is shown the co-circular (σ_+, grey dots) and counter-circular (σ_-, orange dots) emissions with respect to the right handed σ_+ excitation.

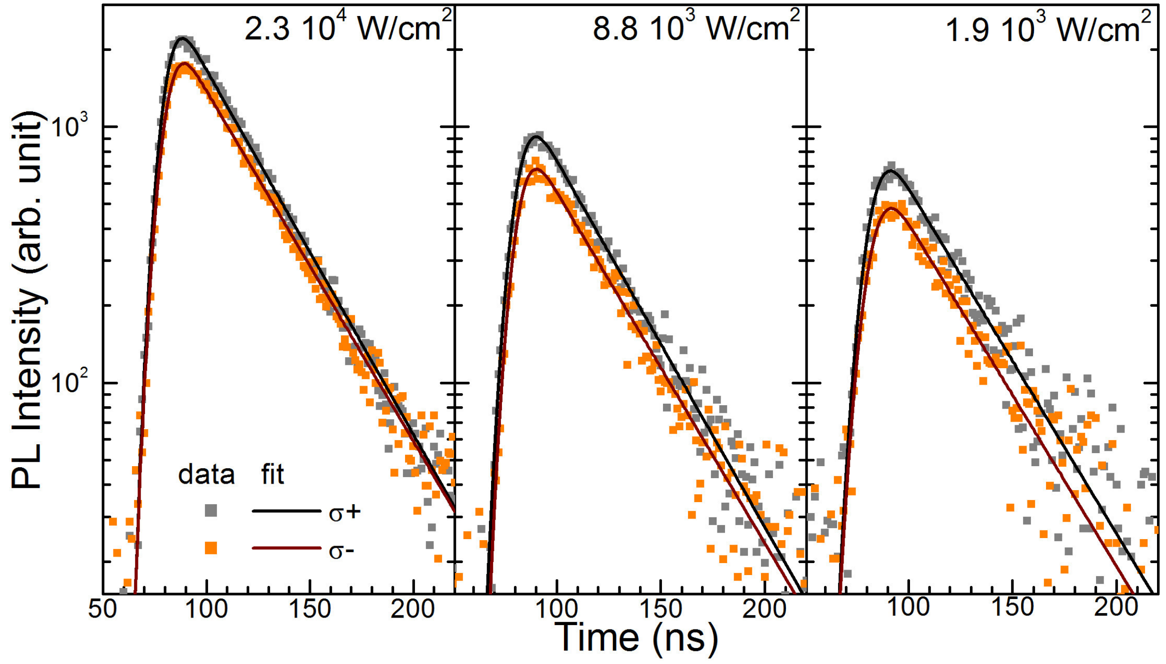

Figure 5.10: Decay curves of the indirect PL emission of a 20 nm thick Ge/$Si_{0.15}Ge_{0.85}$ MQWs at T=4K, under excitation by 1.165 eV circularly polarized laser. The three panels report data (dots) and fits (lines) of the σ_+ (grey, black) and σ_- (orange, red) PL intensity components for the various pump power densities.

Power density (W/cm^2)	ρ_0 (%)	T_1 (ns)
$2.3 \cdot 10^4$	10 ± 1	120 ± 10
$8.8 \cdot 10^3$	14 ± 1	180 ± 20
$1.9 \cdot 10^3$	16 ± 1	800 ± 300

Table 5.2: Inizial polarization degree ρ_0 and spin relaxation time T_1 obtained for different pump power densities.

Figure 5.10 demonstrates that, by increasing the pump power, the initial PL polarization decreases. Moreover, the equalization of the PL intensity of the right- and left-handed components occurs at earlier times, implying shorter T_1 values. The calculated values of initial polarization degree ρ_0 and spin-relaxation time T_1 at different pump power densities are listed in Table 5.2. This strong T_1 suppression can be ascribed to electron-hole exchange interaction, which depends on the density of carriers, as an effective spin relaxation mechanism in this quantum confined systems [137, 138]. To confirm this hypothesis, we calculate the optically injected carriers density from the laser pulse power. The PL decay curve of Figure 5.6 show that the carrier lifetime is 30 ns, while the FWHM of the laser pulse is much shorter (about 14 ns, as reported in Appendix A). As a result, we can assume that no recombination takes place during the pulse absorption. The pulse excitation power density has been evaluated as fol-

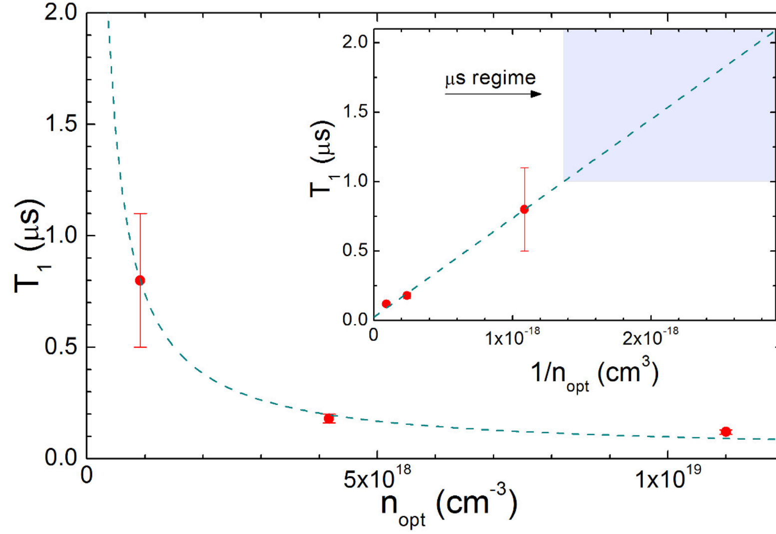

Figure 5.11: Spin relaxation time T_1 as a function of photoinjected carrier density n_{opt}. The inset shows the linear dependence with respect of T_1 the reciprocal $1/n_{opt}$. The μs regime region is underlined.

lows. The laser power was measured by a thermopile, providing the average $P_{average}$ distributed on a laser spot area A, obtained by measuring the spot diameter of about $d = 47\mu$m. The pulse power is

$$P_{pulse} = \frac{P_{average}}{f \cdot \Delta t} \tag{5.3}$$

where f is the laser pulse frequency (10 kHz) and Δt is the laser temporal width. As a consequence, the pulse power density is defined ad P_{pulse}/A.

For sake of simplicity, we model the laser pulses as a rectangular wave. The energy associated with a single pulse is $E_{pulse} = P_{pulse} \cdot \Delta t$, while the number of photons reaching the sample surface for a pulse is $\phi_{pulse} = E_{pulse}/h\nu$. Here $h\nu$ is the energy of a single photon, *i.e.* 1.165 eV. Finally, the concentration of absorbed photons inside the sample depends on the surface reflectivity (R), and on the absorption coefficient (α) of the Ge, according to the formula [48]:

$$n_{opt} = \frac{\phi_{pulse} \cdot (1-R) \cdot \alpha}{A} \tag{5.4}$$

In the analysed sample, R = 0.38. By using the literature data in the work of Bonfanti *et al.* [31], we approximate $\alpha = 1.1 \cdot 10^4 \text{cm}^{-1}$ for a single QW. Carrier-loss mechanism due to radiative recombination through the direct band gap can be neglected because the probability of electron transfer out of the Γ valley is about four order of magnitude larger than the one of a radiative event at the zone center [25, 32]. Hence n_{opt} corresponds to the initial concentration of L-valley electrons.

In Figure 5.11 is shown a monotonic dependence of T_1 on the density n_{opt} of elec-

trons optically injected in the QWs at the various excitation power levels. The well-defined density-dependent characteristics and the marked suppression of T_1 openly confirm the surge of the electron-hole exchange interaction [34, 137, 138]. Possibly, this spin-relaxation channel is strengthened in the QWs by the spatial confinement of the carriers. This might have concealed the direct observation of the phenomenon in previous literature reports dealing with bulk Ge [42, 61].

Since, to a first approximation, the T_1 dependence on n_{opt} can be modelled as $T_1 \propto n_{opt}^{-1}$ (dashed line in Figure 5.11), we can disentangle the exchange interaction mechanism from the optically derived data and extrapolate a spin-lattice relaxation time in the μs regime for a lower carrier density, as shown in the inset of Figure 5.11. It is worth noting that this density value is below the detection limit for the optical measurement, due to the strong reduction of the PL by decreasing the pump power.

To overcome this limitation, in the following we compare the T_1 derived by the PL with the spin-lattice relaxation time obtained by electron spin resonance (ESR) technique.

5.4 Comparison between ESR and TRPL

In this section we thus present the experimental ESR data of conduction electrons in type I Ge QWs [34]. ESR is one of the most accurate techniques allowing one to gather information on the spin-orbit coupling phenomena in semiconductor-based structures. ESR provides the derivative signal of the spin-flip due to microwave absorption of electrons in a uniform magnetic field. By scanning the magnetic field at constant microwave frequency, one can obtain spectra from which important informations such as the Landé g factor can be derived. The study of the ESR linewidth provides the information on the T_1 and the T_2 of confined electrons in two-dimensional Ge-based systems, as briefly discussed in Appendix A.

We have carried out ESR measurements on n-type modulation doped Ge MQWs samples (8931- series, listed in Table 5.1) as a function of the well thickness: 20 nm, 17 nm, and 15 nm (details on samples can be found in Appendix B).

During the ESR measurements, the magnetic field H is rotated in the $(1\bar{1}0)$ plane from the <001> to the <110> crystal direction. The orientation of the magnetic field is indicated by the angle θ between H and the <001> direction. Since the cleavage planes of Ge belong to the [011] family, a rotation of the sample by 90° corresponds to a rotation of H in the $(1\bar{1}0)$ plane from the growth direction <001> ($\theta = 0$) to the <110> direction in the crystal (H parallel to the QW plane, $\theta = 90°$). As sketched in Figure 5.12a, in this geometry also the <111> direction is met. The ellipsoidal

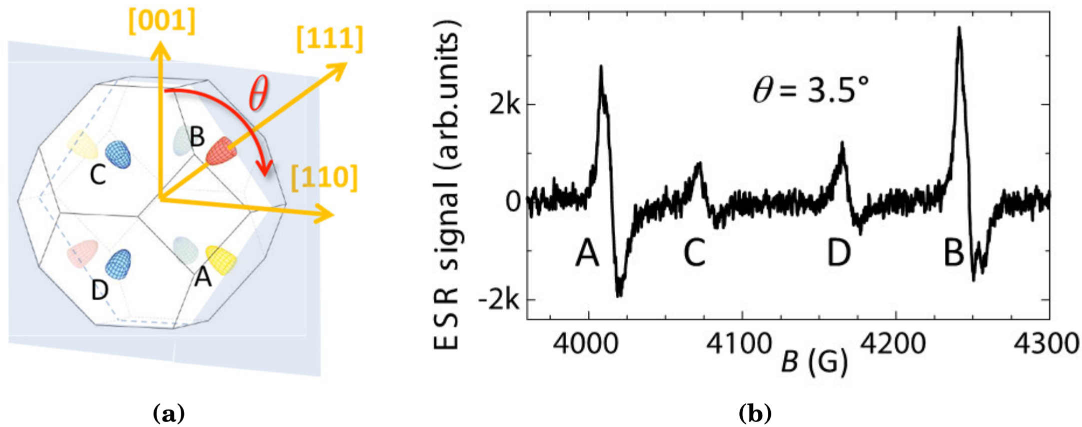

(a) (b)

Figure 5.12: (a) Brillouin zone of bulk Ge. The ellipsoidal isoenergetic surfaces of the conduction band at the L point are shown. θ is the angle between the <001> crystallographic direction and the magnetic field B, which scans towards the <110> direction. (b) ESR signals from conduction electrons in Ge QWs measured at T=2 K and θ = 3.5°, after subtracting a linear background.

surfaces of different L minima, shown in Figure 5.12a, in general have different angles relative to H, with one exception: for H parallel to the <001> direction ($\theta = 0$). In this case, all ellipsoids have the same angle with H. As a result of the g anisotropy, ellipsoids with different orientations with respect to H provide different g values and, as a consequence, different spin resonance signals. Figure 5.12b shows ESR spectrum of n-mod doped Ge/$Si_{0.15}Ge_{0.85}$ QWs sample at θ=3.5°, and T=2 K. Four well defined spin resonances are observed. The magnetic field intensity at which each resonance appears determines its g factor.

It is worth noting that the observation of a well-resolved ESR multiplet proves that spin relaxation of conduction electrons in MQWs is dominated by zone-centre intravalley rather than zone-edge intervalley electron-phonon coupling [49]. The latter, due to scattering among the different L minima, would have otherwise averaged out the g factors, eventually yielding a single spin resonance line [131]. By working at cryogenic temperatures, we could selectively quench the intervalley scattering in MQWs, that previous literature work recognized as one of the crucial factors in limiting the experimentally accessible spin-relaxation times [59, 139]. This open up the possibility to precisely unveil relevant spin-flip and dephasing mechanisms.

Here we present the ESR results on the spin relaxation and dephasing time in Ge QWs and the comparison between the the T_1 obtained from ESR and TRPL measurements reported in the previous Section. As detailed in Appendix A, the modelling of resonance lines provides us the T_1 and T_2^* times, summarized in Figure 5.13, for all the MQWs samples. T_1 was obtained by modelling the linewidth of the spin resonance

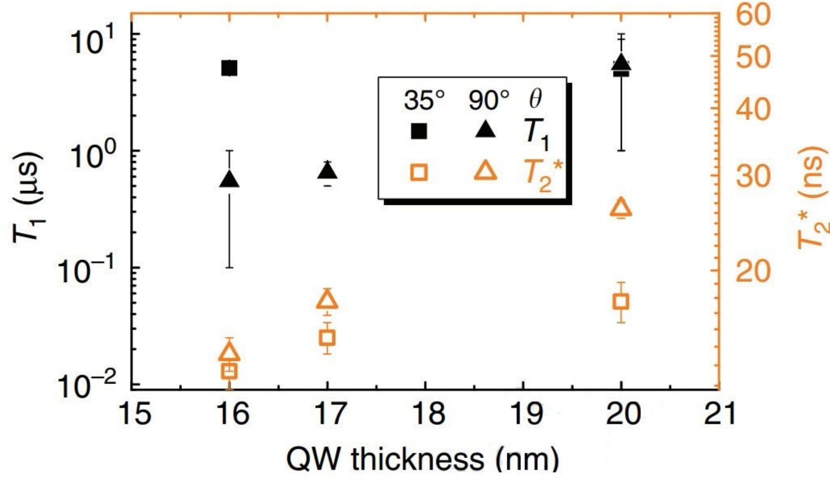

Figure 5.13: Values of spin-lattice relaxation time T_1 and ensemble dephasing time T_2^* obtained from ESR peaks in QWs with different thickness from Ref. [34].

signal as a function of the microwave power [140] at θ = 90°. The results, shown in Figure 5.13, provide a T_1 of few μs for all the three QWs thickness under investigation.

Moreover, we can determine the relaxation time of the spin ensemble T_2^*, summarized in Figure 5.13, which provides a lower limit for the spin decoherence time T_2 [140].

T_2^* turns out to be ~ 20 ns, which is about two times longer than the hyperfine-limited dephasing times of electrons bound to shallow donors listed in Table 5.3 [24]. This behaviour is in agreement with the physical picture of itinerant electrons subject to fluctuating confinement potentials described in Section 3.2.3. Moreover, Figure 5.13 also shows that T_2^* decreases in thinner QWs, due to an enhancement in the electron localization, with a correspondingly increasing efficiency in the spin dephasing due to hyperfine coupling. Above all, the spin-lattice relaxation times T_1 derived in MQWs are substantially longer than the one reported for conduction electrons in bulk Ge at the same temperatures, as summarized in Table 5.3 [34, 42, 61]. In this temperature regime, theory suggests a T_1 extending well above the μs range, whilst the

Reference	Sample	T_1 (μs)	T_2^* (ns)	T (K)	Electrons
[59]	intrinsic Ge	0.2-0.9		30-60	Cond. - 3D
[61]	intrinsic Ge	0.017-0.065	26-36	30-60	Cond. - 3D
[42]	intrinsic Ge	0.127-0.26		4-50	Cond. - 3D
[34]	Ge MQWs	1-5	10-30	2-5	Cond. - 2D
[24]	7.8% ^{73}Ge:As	50-800	11	2-5	Bound

Table 5.3: Survey of the spin relaxation T_1 and dephasing T_2^* time measured for electrons in Ge. Adapted from Ref. [34].

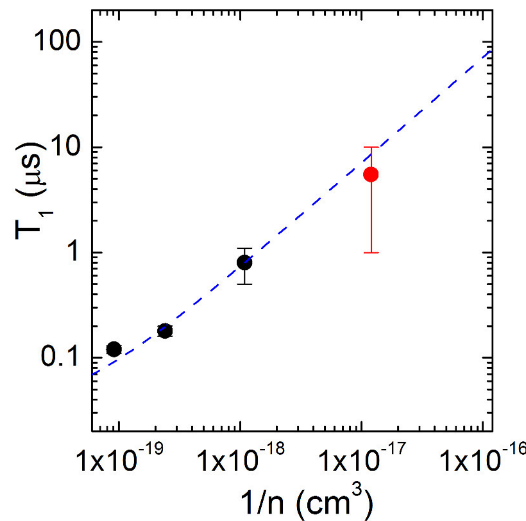

Figure 5.14: Spin relaxation time T_1 as a function of the reciprocal of the carrier density n (logarithmic scale). The T_1(2DEG) of $5 \pm 4\mu$s pertains to electron concentration n(2DEG) of the 20 nm n-mod MQWs studied by ESR (red dot).

experimental results are found to be limited in hundred of ns regime [42]. All these endeavours put forward the subtle role played by impurities in introducing extrinsic spin-relaxation channels [141, 142] that in bulk Ge emerge at low temperatures and drastically prevail over the intrinsic but slower Elliott-Yafet process.

In the MQWs structure analyzed, by spatially separating conduction band electrons residing in the Ge QW from their parent donor atoms embedded in the SiGe barriers, we have prevented the impurity-induced bottleneck pertaining to experiments utilizing bulk Ge wafers, and eventually resolve long-lived spins despite the low temperature operation. This demonstrates that quantum confinement, guaranteed in our Ge/SiGe heterojunctions by the type I band alignment, possibly provides an additional mechanism concurring to the lengthening of T_1 that arises when the conduction electrons reside in QWs rather than in bulk material.

Crucially, the density of carriers introduced by the remote doping in the n-mod samples turns out to be n(2DEG) $\sim 5 \cdot 10^{16}$cm^{-3}, which is about two order of magnitude lower than the n_{opt} calculated in previous optical measurements. Even though the PL intensity would preclude a measurement at $n_{opt} \approx$ n(2DEG), we can attempt to reconcile PL and ESR data [34]. We compare the optically derived data with the spin-lattice relaxation time pertaining to the n-mod Ge QWs with the same well thickness (20 nm) studied by ESR. Figure 5.14 shows that $T_1 = 5 \pm 4\mu$s for the 2DEG (red dot in Figure 5.14) inferred from ESR measurements is in good agreement with the linear trend of spin-lattice relaxation time obtained *via* optical technique.

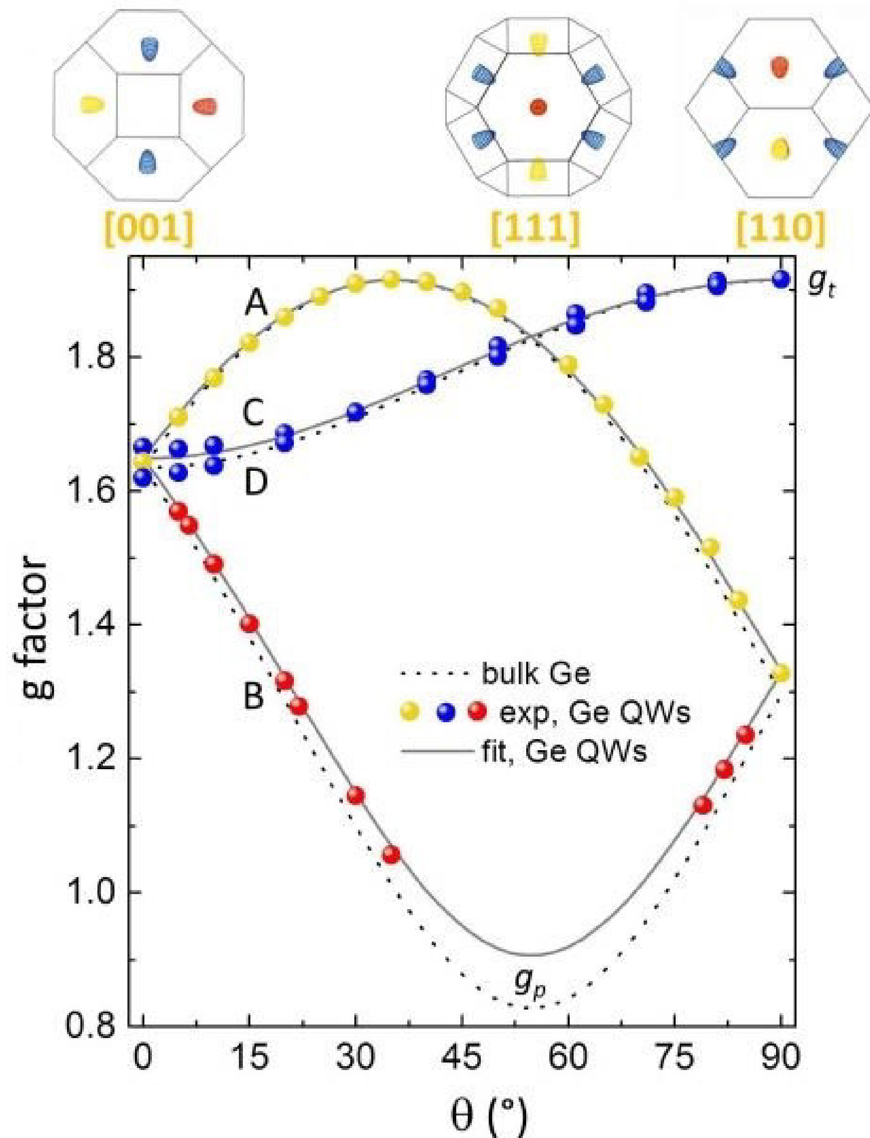

Figure 5.15: Values of the g factor measured from the ESR peaks at T=2 K in a 20nm Ge MQWs as a function of θ. The correspondence between the angle θ and the main crystallographic directions are highlighted in the upper part of the figure. There are shown the sketches of the Brillouin zone when B is directed along the main crystallographic axis.

5.4.1 g factor of conduction electron in Ge/SiGe QWs

Here we present the results of ESR measurement on the g factor of n-type modulation doped Ge MQWs samples as a function of the well thickness [34]. As described in the previous Section, the spin resonance signal is provided by the resonant absorption of electromagnetic radiation by unpaired electrons in a magnetic field, and provides many information on the spin properties of carriers, in particular the g factor. For a free electron moving on a single ellipsoidal surface, the effective g value is given by

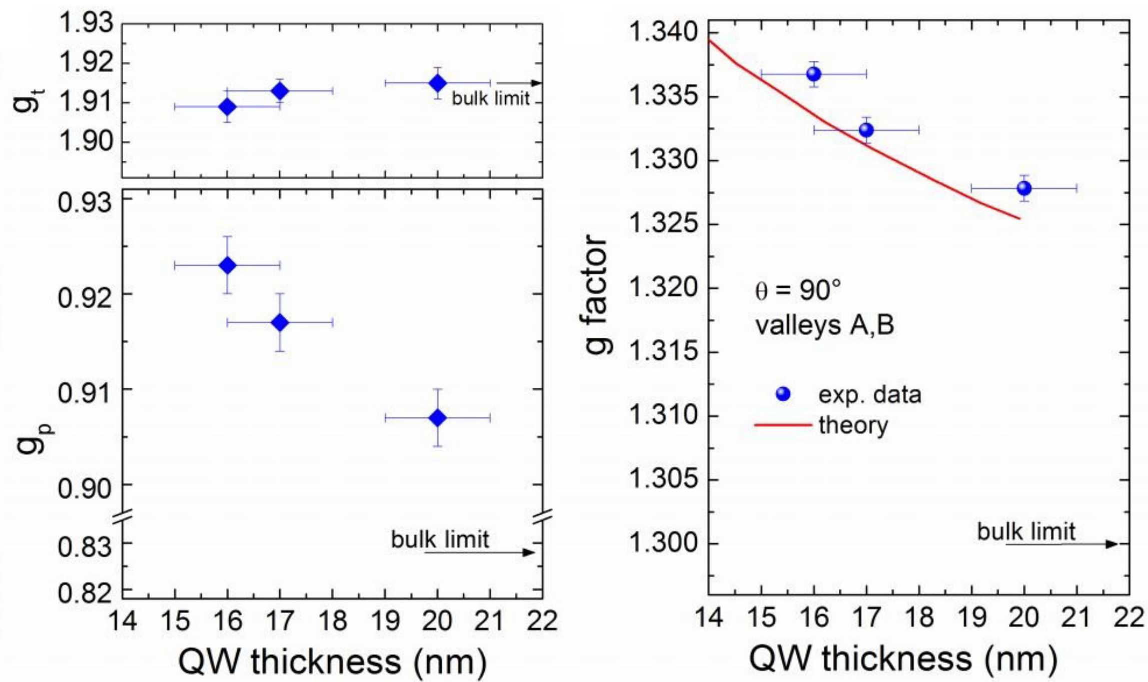

Figure 5.16: Values of g_p and g_t reported in ref. [143] for bulk Ge (arrows), and obtained in Ref. [34] (diamonds) for Ge QWs with different thickness. Errors bars were derived from the least square fitting analysis of the experimental data. (b) g factor values at θ = 90° for the valleys A and B as a function of the QW thickness. The experimental data of Ge QWs (dots) are reported along with the values calculated by Baron *et al.* in ref. [143] (red line), and the reference values of bulk Ge according to ref. [143]. Error bars of the g factor were derived from the resonance field uncertainty [34].

[140]:

$$g^2 = g_p^2 cos^2\phi + g_t^2 sin^2\phi \tag{5.5}$$

where g_p and g_t are the longitudinal and the transverse components of the g tensor lying along or being normal to the major axis of the ellipsoid, respectively, and ϕ is the angle between the direction of the magnetic field H and the major axis of the ellipsoidal energy surface.

Different spin resonance signals, as shown in Figure 5.12b, are provided by different g values, as a result of ellipsoids with different orientations with respect to H. The magnetic field intensity at which each resonance appears determines its g factor.

The g factor of each resonance changes with the sample orientation: the values of g obtained for the four spin resonances as a function of θ are reported in Figure 5.15. The dashed lines in Fig. 5.15 show the g factor of L-valley electrons in bulk Ge, calculated using Eq.A.6 using $g_p = 0.82$ and $g_t = 1.93$, reported in the literature [143].

We carried out ESR measurements on different Ge QWs samples as a function of the well thickness. Figure 5.16 reports g_p and g_t as a function of the well thickness

along with the corresponding bulk Ge value (arrows) taken from the literature [143]. The dependence of g on the well thickness calculated in Ref. [143] is also reported. The experimental data are in good agreement with the theory. Remarkably, while g_t of bulk and QW coincide within the experimental error, g_p becomes substantially larger than the bulk limit as the QW width decreases. This demonstrates that in Ge/SiGe MQWs confinement acts on the spin-orbit coupling of CB electrons inducing interactions between the lowest conduction band at the L point and the other close and remote bands [34].

The measured g factor of the QWs (Figure 5.16) shows a strong evidence of the confinement effect, in good agreement with the theoretical prediction of the g factor anisotropy in these structures reported in the literature [143].

6 Conclusions

The microelectronics industry is striving for a paradigm shift, called More-than-Moore. This consists of the exploitation of novel functionalities *via* advanced designs and technologies, rather than pursuing progress *via* the typical scaling-down approach foreseen by the canonical Moore's law [144].

Spintronics [20] and photonics [74] are two mainstream pathways that are separately explored to extend and enrich the performances of the existing Si devices, notwithstanding the tremendous potential that would be enabled by their joint implementation [145]. The main goal of such an attempt is to design and develop a new generation of devices by combining standard microelectronic properties with spin-dependent effects and light-matter interaction, while preserving the large-scale and cost-effective production offered by the microelectronics foundries [21]. With this respect, Ge offers key advantages, such as a quasi-direct behaviour, which stimulated detailed investigations of its photonic properties for integration within the complementary metal oxide semiconductor (CMOS) technology. Moreover, Ge presents an intriguing spin physics which stems from the non-trivial dynamics in its multi-valley conduction band.

This work aims to close the gap between spintronic and photonic, by leveraging the unique properties of Ge, achieved by means of strain and quantum confinement. Strain has been widely exploited to engineer Ge band structure [11, 92], aiming to enhance the performances of electronic [4] and photonic [7, 18] devices. Despite such advantages, a systematic understanding of carrier and spin kinetics in strained Ge is still lacking, although it is of fundamental interest and central importance for any applications in spintronics and photonics.

In this thesis, we have carried out a systematic investigation of the fundamental

spin properties of strained and low dimensional Ge heterostructures. This has been achieved *via* an all-optical technique, by exploiting the quasi-direct behaviour of Ge to gather optical access to its spin processes [25]. One of the main advantages of the all-optical technique is to avoid spin depolarization that affect electrical measurements due to interfaces within ferromagnetic material, thus inhibiting the measurement of intrinsic spin lifetime [30].

Within this aim, we perform polarization-resolved PL measurements of the direct gap emission of tensile strained Ge films epitaxially growth on Si. Our results reveal that the strain-induced band-gap narrowing provides a sizable access to the transition involving split-off (SO) band *via* the absorption of infrared (IR) photons. Indeed, the spin orientation of electrons photoexcited from SO states has a dominant role in determining the polarization degree associated with the radiative recombination across the direct gap. In particular, the fundamental strain-splitted transition has a low temperature circular polarization degree as high as 85%, despite an off-resonance excitation of more than 300 meV [33]. This is the highest value reported so far for group-IV materials and it is due to the non-trivial electron spin dynamics in multi-valley Ge conduction band. This provides a remarkable difference with respect to strained III-V compound, in which high polarization degree can be achieved only through resonant light absorption at an excitation energy that matches the fundamental strain-split transition [23, 29]. Moreover, we demonstrate that, by varying lattice temperature and doping content, it is possible to tune the density of photoexcited carriers occupying the two spin states contributing to light emission through the direct gap. This findings introduces effective tools to govern the helicity and the degree of polarization of the direct gap emission.

In this thesis, we have focused also on confinement effects on spin physics of Ge heterostructures, performing a comprehensive study of the spin dynamics of the photoexcited carriers in $Ge/Si_{1-x}Ge_x$ multiple quantum wells (MQWs). In such systems, the confinement and the epitaxially induced strain provide an effective control over the optical transition energies, eventually yielding a type-I band alignment for both the direct and the indirect bandgaps [31, 32, 117].

In particular, the polarization of the indirect emission of $Ge/Si_{0.15}Ge_{0.85}$ MQWs is exploited to measure the spin lifetime of electrons by means of polarization- and time-resolved PL. We investigate the spin relaxation time as a function of the pump powers, *i.e.* of the photoinjected carrier densities. Measurements at T = 4 K reveal spin lifetime varying from 120 ns to 800 ns by decreasing pump power. This reduction of the spin lifetime with increasing photoinjected carrier density allow us to probe the effect of electron-hole exchange interaction as a spin relaxation mechanism. In particular,

we have been able to determine the spin relaxation time of thermal electrons in the low density limit. This result has been directly compared with ESR data on n-type modulation doped Ge/$Si_{0.15}Ge_{0.85}$ MQWs. These measurements provide information on the spin relaxation (T_1) and spin decoherence (T_2) times of a 2D electrons gas at T=2 K. The former (latter) is found to be in the μs (tens of ns) range for different well thickness [34], matching well the optically derived T_1 values [34].

This result underlines the promising role of modulation doped Ge/SiGe MQWs to overcome the extrinsic limitation of spin relaxation time in Ge introduced by impurities, which has been found to play a dominant role in low temperature regime in relaxed bulk Ge [141, 142].

In conclusion, this work is devoted to an all-optical study of the spin properties of Ge-based systems. Original results obtained in this thesis, both on strained epitaxial Ge-on-Si films and on low dimensional Ge/SiGe MQWs heterostructures, can represent a step forward in the comprehension of the relaxation and dynamics of spin polarized electrons in group IV materials. These findings possibly provide new routes for the realization of novel spintronic devices, by combining the huge potential of Ge-based heterostructure with the powerful tools for bandgap engineering, namely the quantum confinement and strain.

Methods

This appendix is devoted to the description of the experimental set-up used in this thesis to perform PL measurements. At first, we describe the polarization-resolved continuous-wave photoluminescence (CWPL) apparatus, and then the time-resolved PL (TRPL). Finally we show details of the Electron Spin Resonance technique.

A.1 Continuous-wave PL

Figure A.1 report a schematic drawing of the experimental set-up used in this thesis to perform polarization-resolved CWPL. The light source is a linearly polarized CW $Nd:YVO_4$ laser (CNI Lasers) emitting at 1.165 eV (i. e. 1064 nm). The power ranges from a few mW to 500 mW. The exciting beam, filtered through two 1064 nm band-pass (BP) filters and a 850 nm long-pass (LP) filter, pass through a half waveplate ($\lambda/2$) and a quarter waveplate ($\lambda/4$) allowing the light incident on the sample to be right-handed (σ_+) circularly polarized. PL measurements are carried out in the backscattering geometry: the direction of the luminescence detection is the same along which the sample is excited, namely perpendicular to the sample surface. The reflecting mirror for the laser beam is a 3 mm diameter silver mirror, mounted on a 5 cm diameter gimball support. The laser light is focused on the sample surface by means of an achromatic doublet with 100 mm focal length. Figure A.2 shows the laser spot diameter as a function of the doublet position. The focused spot diameter was measured to be about 47 μm. The sample is mounted in a cryostat cooled by a closed cycle helium refrigerator (Oxford Optistat AC-V12). Vacuum is obtained by means of a set of pumps (HiCube Classic, produced by Pfeiffer Vacuum). The PL signal emitted by the sample is collected by the focusing doublet in a 1 inch diameter beam and sent to the analyser,

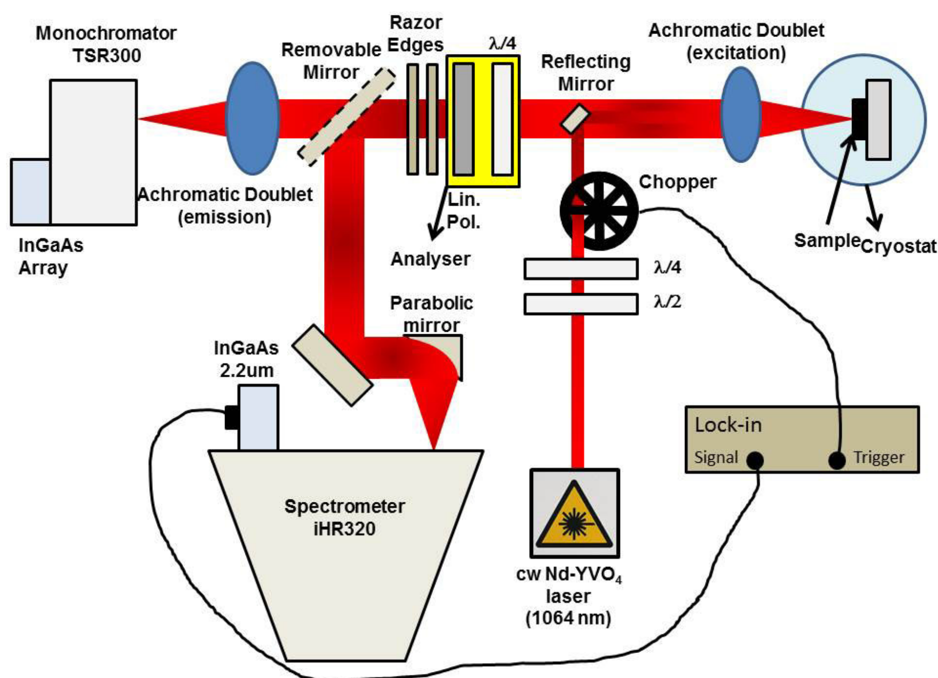

Figure A.1: Sketch of the experimental set-up used for polarization-resolved continuous-wave PL measurements described in Chapters 4, 5.

consisting of a rotating $\lambda/4$ waveplate followed by a linear polarizer. The $\lambda/4$ waveplate is mounted on a rotating holder synchronized with the detection system. Two 1064 nm razor edge (RE) filters reject the laser light. The PL signal can be directed towards two different spectrometers by means of a removable mirror. The two spectrometers are coupled with an InGaAs array detector and an extended 2.4 μm InGaAs single-channel detector. In the following the two optical paths are described.

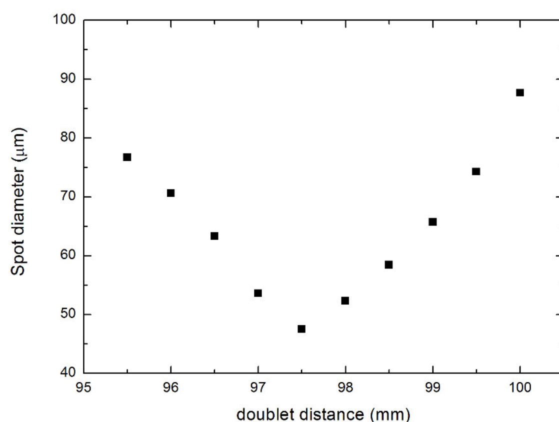

Figure A.2: CW Nd : YVO_4 laser spot as a function of the achromatic doublet position. The measured diameter at the minimum position (97 mm of doublet distance) is 47 μm.

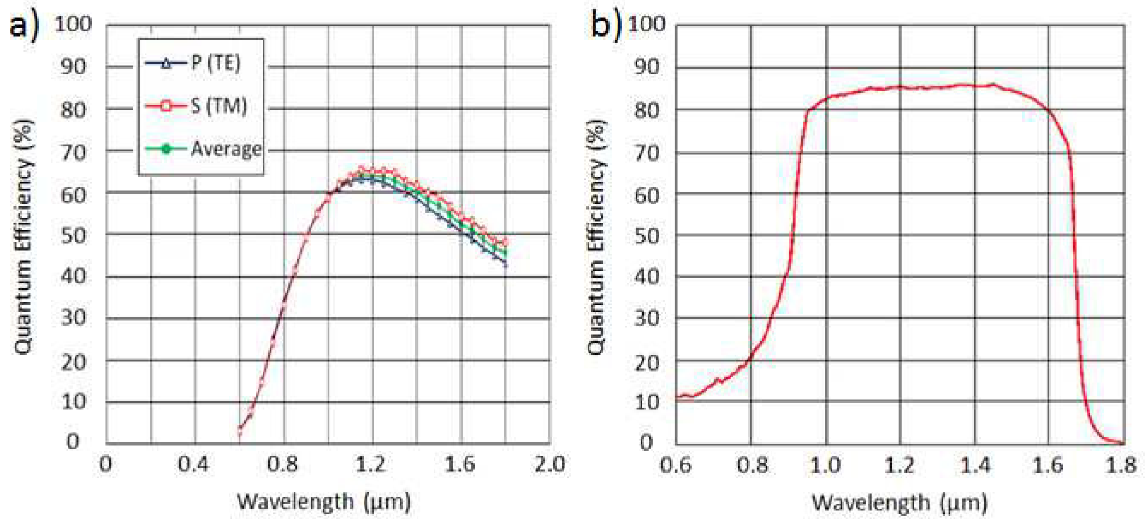

Figure A.3: (a): Quantum efficiency of the 100 lines/mm holographic diffraction grating, blazed at 1.2 μm. P and S stem from transverse-magnetic and transverse-electric polarizations. (b): Quantum efficiency of the Andor iDus InGaAs 1.7 μm detector as a function of the wavelength.

A.1.1 InGaAs array line

An achromatic doublet (100 mm focal length) focuses the signal on the entrance slit of a spectrometer with a focal length of 300 mm. The spectrometer (JASCO, TRS-300) is equipped with a 100 lines/mm holographic diffraction grating (Shimadzu company), having a blaze at 1.2 μm. The spectral response of this grating is shown in Figure A.3a.

The dispersed light is measured by a thermoelectrically cooled InGaAs 512 pixels multichannel detector (DU492A-1.7, produced by Andor Technology) with a cut-off energy at 0.75 eV. The spectral response of the InGaAs array detector is shown in Figure A.3b. This optical line was used to perform direct-gap PL measurements of tensile strained Ge-on-Si reported in Chapter 4.

A.1.2 Single-channel extended InGaAs line

By adding a removable mirror on the optical path, as sketched in Figure A.1, the collimated PL is directed towards a gold-coated parabolic mirror (100 mm focal length), that focuses the signal on the entrance slit of a spectrometer with a focal length of 320 mm. The monochromator (HORIBA iHR 320) is equipped with 3 holographic diffraction gratings, mounted on a turret. In this work, only the grating with 150 lines/mm groove density and blaze at 2 μm was used: its spectral response is shown in Figure A.4a.

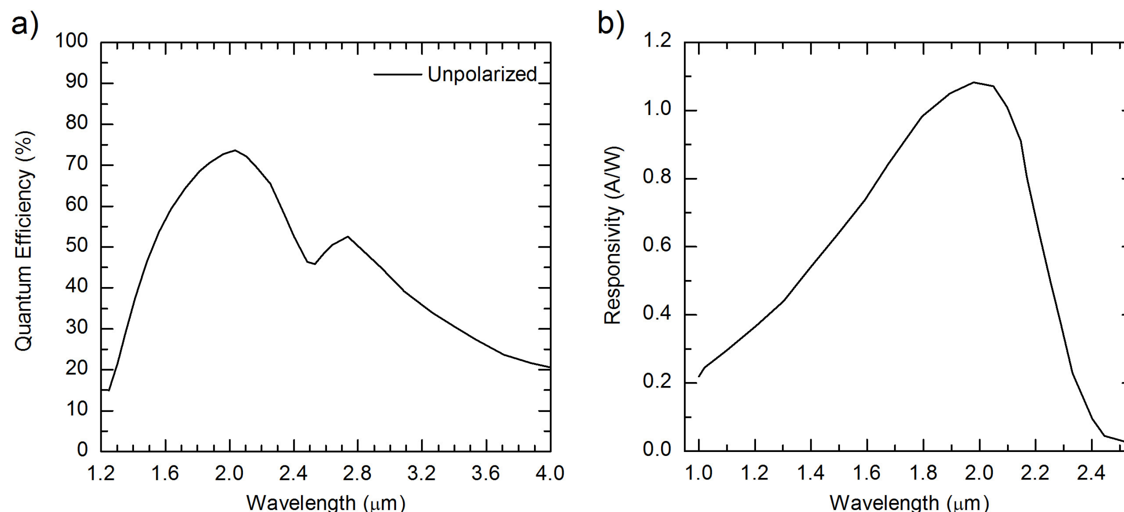

Figure A.4: (a): Quantum efficiency of the 150 lines/mm holographic diffraction grating. Blaze is at 2 μm. (b): Quantum efficiency of DSSIGA2.2 LN InGaAs 2.2 μm detector as a function of the wavelength.

The dispersed light is then measured by a liquid nitrogen cooled InGaAs single channel detector (DSSIGA2.2 LN, sold by HORIBA Jobin Yvon) with a cut-off energy at about 0.52 eV. Its spectral response is shown in Figure A.4b. Finally, the output signal of the detector is filtered by means of a SR510 Stanford lock-in amplifier. This set-up was used to carry out the CWPL of $Ge/Si_{0.15}Ge_{0.85}$ MQWs sample in Chapters 5.

A.2 Time-resolved PL

A schematic drawing of the experimental set-up used to carry out polarization-resolved TRPL with a resolution in the ns time scale is reported in Figure A.5. The excitation source is a 1.165 eV (1064 nm) DTL-324QT Nd:YAG Q-switch pulsed laser (Laser-Export) having a repetition rate of 10 kHz and an average power density of 6.8kW/cm^2. The peak power density of $4.9\cdot10^4$ kW/cm^2 was calculated using the following formula:

$$D_{Pulse} = \frac{P_{Pulse}}{A} = \frac{P_{average}}{A} \cdot \frac{1}{f \cdot \Delta t} \tag{A.1}$$

where $P_{average}$ is the average laser power, A is the spot area of the laser beam focused on the surface of the sample, f is the laser repetition rate and Δt is the laser temporal width. The temporal width of the laser is about 14 ns at 10 kHz (Figure A.6a). The laser light follows the same excitation optical path described in section A.1, as illustrated in Figure A.5.

The emission path is the same as described in Section A.1.2, and the PL is collected

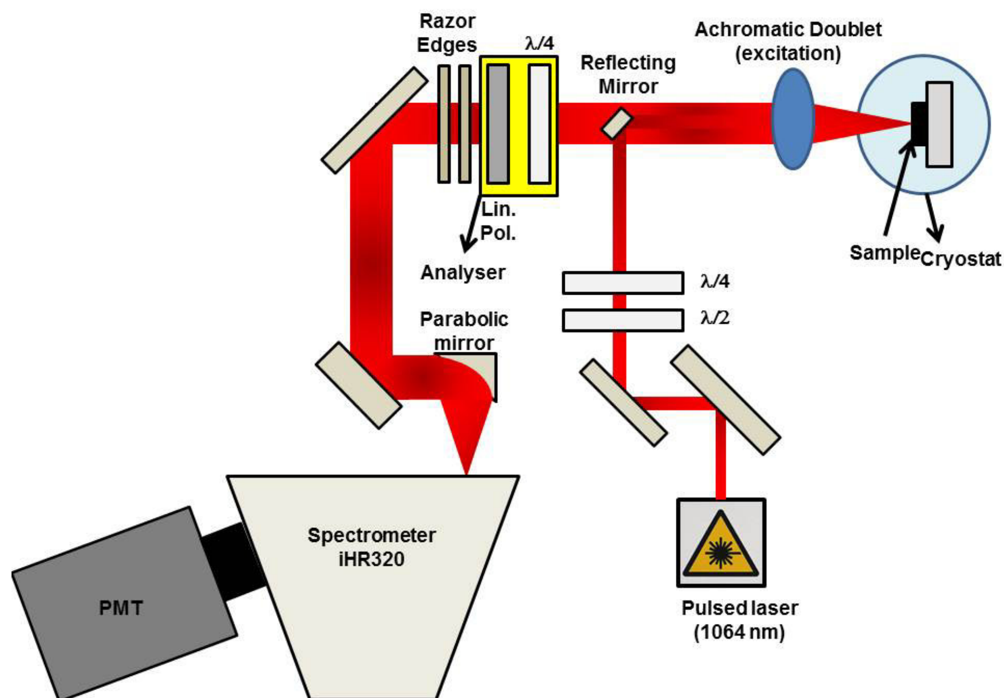

Figure A.5: Sketch of the experimental set-up used for the polarization- and time-resolved PL measurements with nanosecond time resolution.

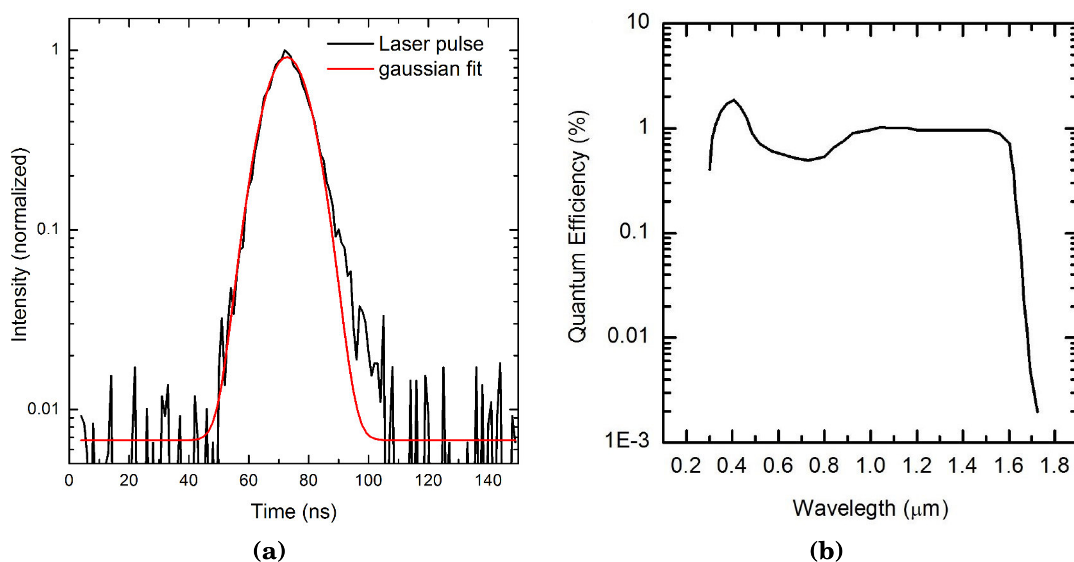

Figure A.6: (a) Laser pulse temporal width (black line) and Gaussian fit (red line). The FWHM obtained from the fit is 14 ns. (b) Photomultiplier spectral response [146].

by the same monochromator HORIBA iHR 320 equipped with a 150 l/mm holographic grating. The monocromator is coupled, on the lateral exit slit, to a photomultiplier tube (PMT) by means of two silver-coated parabolic mirrors (100 and 150 mm of focal length, respectively), which focus the PL signal on the photocathode of a liquid nitrogen cooled Hamamatsu R5509-73 PMT, with a cut-off energy at about 0.77 eV. Its spectral response is shown in Figure A.7. The cut-off is defined by the material of the PMT window (borosilicate glass), and by the InGaAs/InP photocathode. The signal is recorded by a FAST ComTec P7888-1(E) multi-stop acquisition board, working in single photon counting mode with a time resolution of 1 ns. The signal is displayed by means of an oscilloscope, and a trigger coming from the laser provides the start acquisition. The experimental set-up described in this section was employed to carry out TRPL measurements on $Ge/Si_{0.15}Ge_{0.85}$ MQWs reported in Chapter 5.

A.3 ESR technique

We provide here a brief description of the ESR technique, discussing origin and characteristics of the spin resonance signals. Further details about the technique and the analysis of the spin resonance can be found in Ref. [140].

The ESR measurements were carried out by Dr. A. Giorgioni at the Johannes Kepler Universität in Linz (Austria) and by Dr. A. Giorgioni and S. Paleari at the University of Milano-Bicocca (Italy). In the ESR experiments a phase sensitive detection is used, by adding an oscillating component to the uniform magnetic field scanned over a ΔH range, and by a lock-in detection system coupled with the magnetic field modulation [140]. As a result of the phase sensitive detection, the spectra show the first derivative of the spin resonance absorption signal, commonly called *spin resonance*.

The spin resonance signal is provided by the resonant absorption of the electromagnetic radiation by unpaired electrons in a magnetic field [140]. Unpaired electrons in semiconductors can be found in partially filled bands, localized at isolated defects or impurities, or in broken bonds. According to the Zeeman effect two degenerate spin up and spin down states are splitted in energy by an applied uniform magnetic field. The spin-flip absorption of a microwave takes place when the microwave energy hf matches with the Zeeman splitting between the spin up and spin down states. In ESR measurements hf is fixed, while the magnetic field H is scanned over a ΔH range (Figure A.7a). Under resonant condition:

$$hf = g\mu_B \mu H_0 \tag{A.2}$$

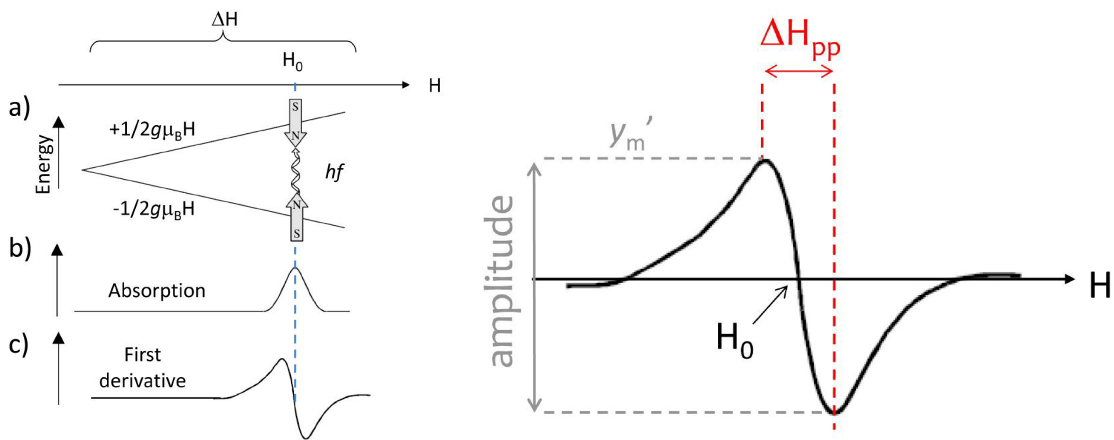

Figure A.7: Left Panel, (a) Zeeman splitting of two spin up and spin down states as a function of the magnetic field H. (b) absorption signal of an electromagnetic wave with energy hf taking place at resonance condition with the Zeeman splitting. (c) first derivative of the absorption signal, observed in ESR measurements with phase sensitive detection. Right Panel: Example of first derivative of lorentian spin resonance signal at $\mathrm{H_0}$. The peak-to-peak linewidth $\Delta\mathrm{H_{pp}}$ and the maximum peak intensity $\mathrm{y'_m}$ of the spin resonance are shown.

where g is the Landé g-factor, μ_B the Bohr magneton, μ the permeability and $\mathrm{H_0}$ is defined as the magnetic field providing the resonance condition. The absorption signal (Figure A.7b) as a function of the magnetic field is assumed to be a Lorentian curve, whose peak position is found at $\mathrm{H_0}$. The Lorentzian derivative lineshape (right panel of Figure A.7) has the normalized form [140]:

$$Y'(H) = \frac{16y'_m[(H-H_0)/0.5\Delta H_{pp}]}{\{3+[(H-H_0)/0.5\Delta H_{pp}]^2\}^2} \tag{A.3}$$

where $\mathrm{y'_m}$ is the maximum peak intensity, and $\Delta\mathrm{H_{pp}}$ is the peak-to-peak linewidth of the spin resonance, as summarized in the right panel of Figure A.7. The spin resonance signal provides information on the spin properties of carriers, in particular the g factor and the spin relaxation time $\mathrm{T_1}$. For a spin resonance line, the $\mathrm{H_0}$ value can be identified as the magnetic field at which the curve changes sign and curvature (Figure A.7, right panel). The g factor is then easily obtained by Eq. A.2, once the microwave frequency is known. It worth be noting that ESR measurements can provide g estimations with great accuracy.

In thermal equilibrium and in an external magnetic field, the spin up (↑) and the spin down (↓) states splitted by the Zeeman effect present two different populations $N\uparrow$ and $N\downarrow$, respectively. Assuming that the spin up state is the one at higher energy, then $N\uparrow < N\downarrow$. The microwave absorption perturbs this equilibrium increasing $N\uparrow$, and reducing the difference between the two populations. Besides, the spin system is

coupled to the lattice of the semiconductor, and there is always a finite probability for an energy transfer during which the spin relaxes from its higher energy (↑) state to the lower energy (↓) state. The relaxation processes restore the energy level populations to their thermal equilibrium values, within a characteristic spin-lattice relaxation time, i.e. T_1. For high microwave powers and/or long T_1 the spin system saturates the microwave absorption, providing a new equilibrium condition between the two spin states and causing the population difference to disappear. This condition is called saturation regime. In saturation regime the linewidth of the spin resonance increases, and the peak-to-peak distance of the first derivative of the spin resonance absorption signal (the amplitude shown in the right panel of Figure A.7) decreases. In order to estimate T_1, the value of the linewidth of the absorption peak is needed, both in and out of the saturation regime. T_1 can then be calculated by [140]:

$$T_1 = \frac{\left(\frac{\Delta H_{1/2}}{\Delta H^0_{1/2}}\right)^2 - 1}{\left(\frac{g\mu_B H_1}{\hbar}\right)^2 T_2} \tag{A.4}$$

where $\Delta H_{1/2}$ ($\Delta H^0_{1/2}$) is the measured linewidth in (out of) saturation regime, and H_1 the amplitude of the magnetic field of the microwave inside the sample. For a lorentzian curve, $\Delta H_{1/2}$ can be estimated from the peak-to-peak linewidth of the spin resonance line: $\Delta H_{1/2} = \sqrt{3}\Delta H_{pp}$. Finally, T_2 is defined as:

$$T_2 = \frac{\hbar}{g\mu_B}\frac{2}{\mu\Delta H^0_{1/2}} \tag{A.5}$$

In Chapter 5, we report the results of ESR measurements on modulation n-doped Ge/SiGe QWs. Modulation doping in the barriers provides the spatial separation of the carriers from the impurities, due to the energy profile of the structure [133]. Because of the potential profile, donor electrons are transfered from the barriers to the QW layers, where the carriers are free. Moreover, these electrons are not affected by spin depolarization mechanisms due to impurity scattering, thanks to the remote doping.

A.3.1 Spin-relaxation time

The ESR technique can provide the spin relaxation time T_1, when the spin resonance is measured in the saturation regime. However, in our experimental investigation described in Chapter 5, we were not able to observe any saturation effect. In the following, we thus extract the spin-lattice or longitudinal relaxation time T_1 from the power (P) dependence of continuous wave ESR [140].

For a free electron moving on a single ellipsoidal surface, the effective g value is given by [140]:

$$g^2 = g_p^2 cos^2\phi + g_t^2 sin^2\phi \tag{A.6}$$

where g_p and g_t are the longitudinal and the transverse components of the g tensor lying along or being normal to the major axis of the ellipsoid, respectively, and ϕ is the angle between the direction of the magnetic field H and the major axis of the ellipsoidal energy surface.

At $g = g_t$, the Gaussian broadening due to interface roughness vanishes. Therefore, the ESR line of conduction electrons is fully described by the three contributions defined as follow [34, 147]:

a. absorption signal (AS). It originates from the interaction of the sample with the magnetic field of the microwave through the imaginary part of the magnetic susceptibility. It is given by the spin-flip microwave absorption due to magnetic-dipole transitions, and is well described by:

$$f'_{AS} = -\frac{1}{\pi}\frac{2h}{(1+p+h^2)^2} \tag{A.7}$$

where $\mathrm{h} = \sqrt{3}(\mathrm{B}-\mathrm{B_0})/\Delta\mathrm{B_{pp}^L}$, with $\mathrm{B_0}$ the resonance field, and $\Delta\mathrm{B_{pp}^L}$ the Lorentzian linewidth; $\mathrm{p} = \gamma^2\mathrm{H_1^2T_1}/\Delta\omega$ with γ the gyroscopic factor, $\mathrm{H_1}$ the amplitude of the magnetic field of the microwave on the sample, $\mathrm{T_1}$ the spin-lattice relaxation time, and $\Delta\omega$ the linewidth of the ESR line. The quantity p is proportional to the microwave power due to the term $\mathrm{H_1^2}$. The low power linewidth (far from saturation) is related to the spin relaxation rates by the following relation [140]:

$$\Delta\omega = \frac{1}{2T_1} + \frac{1}{T_2} \tag{A.8}$$

b. dispersion signal (DS). It is provided by the interaction of the sample with the electric field of the microwaves through the imaginary part of the electric conductivity, in the case of high mobility electrons. It is described by:

$$f'_{DS} = \frac{1}{\pi}\frac{1+p-h^2}{(1+p+h^2)^2} \tag{A.9}$$

c. polarization signal (PS). It is due to the interaction of the sample with the electric field of the microwave. This signal arises when the electric conductivity of the sample depends on the spin polarization of the carriers. Indeed, when this condition is verified, the electrical response of the sample changes during the res-

onant microwave absorption, because the spin population changes at resonance. PS has the following shape:

$$f'_{PS} = -\frac{2ph(1+h^2)}{(1+p+h^2)^3} \tag{A.10}$$

These three contributions sum up in the shape function S' describing the ESR line measured at $g = g_t$. We observed that at fixed θ, S' depends on the microwave power P. Particularly, the lineshape depends on P, and does not affect significantly ΔB_{pp}, which is related to $\Delta\omega$.

Giving that the measurement of T_2 is limited by broadening factors [34], we can obtain a lower limit of T_2, called T_2^*. Since T_1 and T_2 are related through the Eq. A.8, a lower-limit estimation of T_2 gives us the possibility to get an upper-limit of T_1.

The whole set of ESR peaks measured as a function of P (at $g = g_t$ and fixed θ) can be fitted by:

$$S' = A_{AS} \cdot f'_{AS} + A_{DS} \cdot f'_{DS} + A_{PS} \cdot f'_{PS} \tag{A.11}$$

yielding the values of T_1 and T_2, and the appropriate values for the weight of the contributions A_{AS}, A_{DS} and A_{PS}.

The modelling of the linewidth, as described above, provides the T_1 values described in Chapter 5

B

Samples

This section is devoted to the description of the samples analyzed in this work. The main features of the growth technique are summarized. Then, the characteristics of the samples studied in this thesis are described and their structural quality is discussed.

B.1 Low Energy Plasma Enhanced CVD

The samples analyzed in this work have been grown by low energy plasma enhanced chemical vapor deposition (LEPECVD). The key features of this technique are a wide range of growth rates (from 0.1 nm/s to 10 nm/s), the independence of the deposition kinetics on the substrate temperature and the close correspondence between the mixture of precursor gases and the composition of the grown layers [119]. Moreover, the LEPECVD allows one to get a good control of the layers thickness and of the interface roughness. A schematic diagram of the LEPECVD system is shown in Figure B.1. The core of this growth system is a CVD reactor in which the cracking of the precursor gases is caused by a plasma flow instead of being due to the high temperature of the substrate. The high intensity of the plasma provides fast deposition rates, while its low energy prevents any damage of the substrate due to collisions with ions. The plasma is generated by a DC arc discharge in an Ar^+ atmosphere between a heated filament (cathode) and the grounded walls of the chamber (anode). External copper coils, that produce a magnetic field, allow to stabilize the plasma flux, to make it homogeneous and to focalize or deviate it. In this way, it is possible to calibrate the intensity of the plasma on the substrate, in order to obtain the desired growth rate. During the deposition process, the working pressure is 10^{-2} mbar. The substrate, whose diameter in

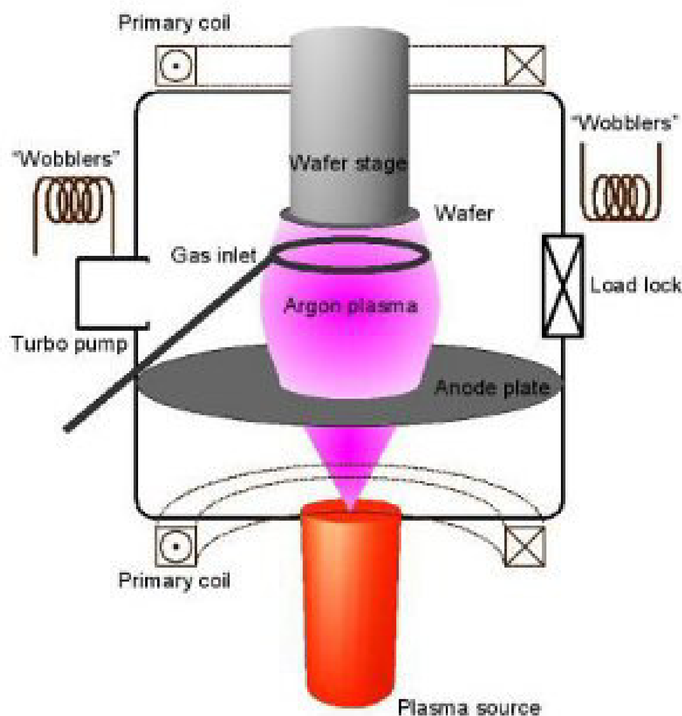

Figure B.1: Sketch of the Low Energy Plasma Enhanced Chemical Vapour Deposition (LEPECVD) [148].

the case of our samples is 4 inch, is kept at temperatures between 450°C and 700°C, depending on the composition of the SiGe alloy to be deposited. The cracking of the precursor gases by the plasma provides a better control of thickness and composition of the grown layers than the thermal activation due to the substrate heating as in conventional CVD. For Ge and SiGe alloys, germane (GeH_4) and silane (SiH_4) are used as precursors, diluted in H_2. In case of n or p doping, PH_3 and B_2H_6 are respectively employed. Further details on the growth process and on the development of LEPECVD technique can be found in Ref. [119].

B.2 Ge-on-Si

In this thesis were studied a set of Ge films grown on <001> Si substrates whose characteristic are reported in Tab.4.1 of Chapter 4.

The 1.5-2 μm thick Ge layers were deposited at 500°C at a rate of 4.2 nm/s and doped *in situ*: 9223-F5 and 9261-F5, dubbed n-Ge and p-Ge, respectively, have the same doping content of $4.5 \cdot 10^{17}$cm^{-3}. The additional 9173-F6 sample is unintentionally doped with an estimated impurity concentration in the low 10^{15}cm^{-3} range, due to the p-type background doping of the reactor. To ensure a tensile strain in the epilayers,

all the Ge-on-Si heterostructures were annealed *in situ* for six cycles between 600°C and 780°C after growth. We also deposited and annealed a set of four samples with p-type doping (B concentration: $3{\cdot}10^{16}$, $2{\cdot}10^{17}$, $5{\cdot}10^{17}$ and $9{\cdot}10^{17}\mathrm{cm}^{-3}$) under the same conditions. The doping level of the samples has been estimated by room temperature resistivity measurements.

B.3 Ge/SiGe MQWs

The MQWs samples studied in this thesis are characterized by the same general structure schematically sketched in Fig. 5.1a in Chapter 5. On a 4-inch Si wafer (100) a graded virtual substrate (GVS) is grown, whose composition varies from Si to $Si_{0.10}Ge_{0.90}$ with a rate of about 7 % μm^{-1}. The GVS is capped with a 2 μm thick relaxed $Si_{0.10}Ge_{0.90}$ layer. The total thickness of this buffer layer is about 15 μm. The active part of the structure is then deposited, alternating $Si_{0.15}Ge_{0.85}$ barriers and pure Ge wells for 500 periods. At the end a 40 nm $Si_{0.10}Ge_{0.90}$ layer and a ~ 10 nm Si cap are grown in order to guarantee that the same strain conditions are experienced at both the edges of the active part of the heterostructure. The actual thickness of the deposited layers is highly non uniform across the 4-inch wafer, due to inhomogeneity

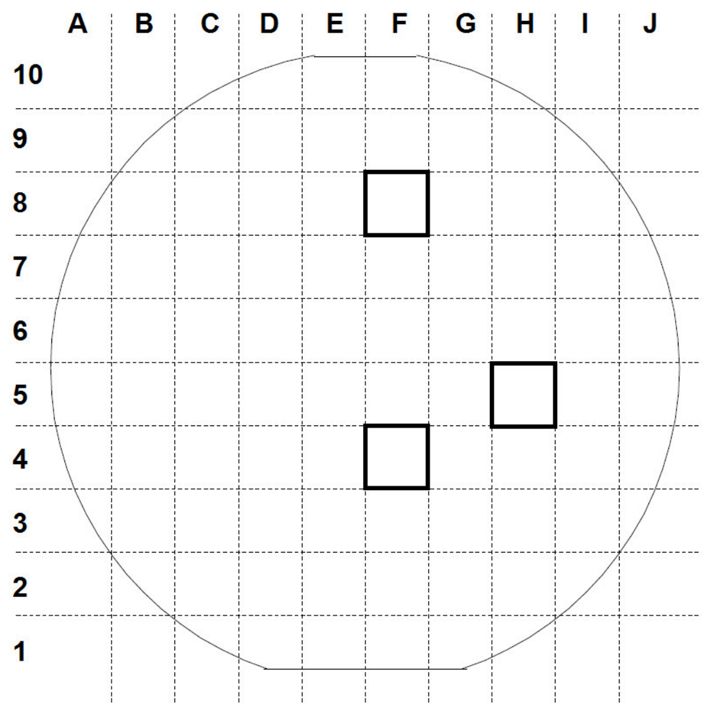

Figure B.2: Typical plan of a wafer that allows one to identify the position of a sample across the wafer. The positions of the analyzed samples (F8, F4 and H5) are also underlined.

in the intensity of the plasma. This inhomogeneity provides samples with identical structure and composition, but with different well thickness. Each sample is thus identified with two numbers: the first refers to the wafer, and the second indicates the position of the sample across the wafer, as schematically illustrated in Figure B.2. The number of periods is 500 and the deposition rates used is 4 - 6 nm/s.

High resolution XRD measurement have confirmed the pseudomorphic growth of the active part of the structure on top of the $Si_{0.10}Ge_{0.90}$, the constant composition layer and the effectiveness of strain balancement in the heterostructure [31]. Moreover, thanks to the strain balance generation of dislocation is inhibited in the active part of the structure.

The samples used for the ESR study are modulation doped samples [133]. Modulation n-doped (n-mod) QWs were obtained by depositing one layer of P atoms in all the $Si_{0.15}Ge_{0.85}$ barrier layers, at the centre of the barrier. The sheet density of P atoms in each barrier is about $10^{11}cm^{-2}$. According to the energy position of the donor states (Figure 5.2 in Chapter 5) at cryogenic temperatures all the donor electrons reside in the QWs. Since the QWs widths are from 16 to 20 nm, the concentration of extrinsic electrons in each QW is $\sim 5-6\cdot 10^{16}cm^{-3}$, as listed in Table 5.1 of Chapter 5.

Stokes analysis

In this chapter we provide details about polarimetry Stokes analysis [109], which was exploited to determine the polarization state of the direct-gap PL of Ge-on-Si (Chapter 4). To introduce the Stokes parameters, we consider a monochromatic optical beam propagating along the z direction and having the following components at $z = 0$:

$$\begin{aligned} E_x(t) &= E_{0x} \cdot cos(\omega t + \delta_x) \\ E_y(t) &= E_{0y} \cdot cos(\omega t + \delta_y) \end{aligned} \tag{C.1}$$

where t is the time, ω the angular frequency, while E_{0x} and E_{0y} are the field amplitudes.

From Eq.C.1 we can describe the optical wave by means of an ellipse (Figure C.1)[65]:

$$\left(\frac{E_y}{E_{0y}}\right)^2 - \left(\frac{E_x}{E_{0x}}\right)^2 - 2\frac{E_x}{E_{0x}}\frac{E_y}{E_{0y}}\cos\delta = sin^2\delta \tag{C.2}$$

where $\delta = \delta_x + \delta_y$ is the total phase displacement between the two components. It is possible to define the ellipse orientation angle ψ with respect the x direction:

$$\tan 2\psi = \frac{2E_{0x}\, E_{0y}\, \cos\delta}{E_{0x}^2 - E_{0y}^2}, \tag{C.3}$$

and the ellipticity angle χ:

$$\sin 2\chi = \frac{2E_{0x}\, E_{0y}\, \sin\delta}{E_{0x}^2 + E_{0y}^2}. \tag{C.4}$$

The Stokes polarization parameters S_i, with i = 0, 1, 2, 3, are measurable observ-

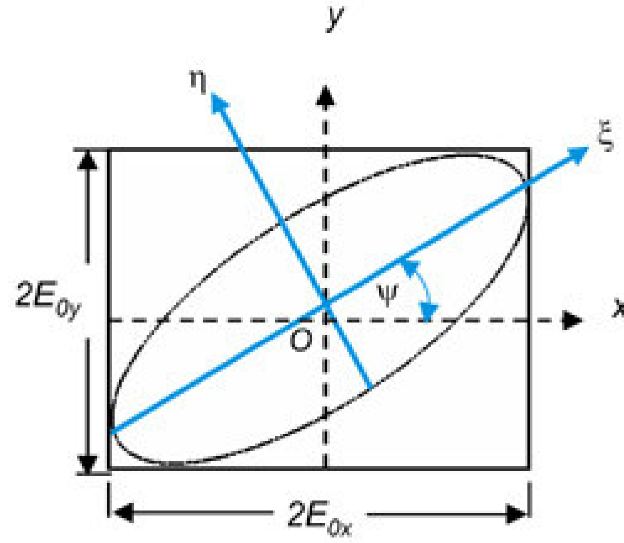

Figure C.1: Polar ellipse.

ables that completely characterize the polarization state of the light field. If we now write the wave equations in the complex form, we get:

$$\begin{aligned} E_x(t) &= E_x \cdot exp(i\omega t) \\ E_y(t) &= E_y \cdot exp(i\omega t) \end{aligned} \tag{C.5}$$

where

$$\begin{aligned} E_x &= E_{0x} \cdot exp(i\delta_x) \\ E_y &= E_{0y} \cdot exp(i\delta_y) \end{aligned} \tag{C.6}$$

are the complex amplitudes. It can be shown that Stokes parameters can be defined as [149]:

$$\begin{aligned} S_0 &= E_x E_x^\dagger + E_y E_y^\dagger \\ S_1 &= E_x E_x^\dagger - E_y E_y^\dagger \\ S_2 &= E_x E_y^\dagger + E_y E_x^\dagger \\ S_3 &= i(E_x E_y^\dagger - E_y E_x^\dagger) \end{aligned} \tag{C.7}$$

where the † indicates the complex conjugate and

$$S_0^2 = S_1^2 + S_2^2 + S_3^2 \tag{C.8}$$

which holds for completely polarized light. S_0 represents the total intensity of the optical field, while S_1, S_2 and S_3 determine the degree of linear (horizontal or vertical)

polarization, linear (+45°or -45°) polarization and circular (right or left) polarization, respectively.

Stokes parameters can be also combined into a vector, called Stokes vector, defined as:

$$\vec{S} = \begin{pmatrix} S_0 \\ S_1 \\ S_2 \\ S_3 \end{pmatrix} = \begin{pmatrix} E_{0x}^2 + E_{0y}^2 \\ E_{0x}^2 - E_{0y}^2 \\ 2E_{0x}E_{0y}cos\delta \\ 2E_{0x}E_{0y}sin\delta \end{pmatrix} \tag{C.9}$$

It is also possible to write the polarization ellipse parameters as a function of the Stokes's parameters:

$$\begin{aligned} \tan 2\psi &= \frac{2E_{0x}\, E_{0y}\, \cos\delta}{E_{0x}^2 - E_{0y}^2} = \frac{S_3}{S_0} \\ \sin 2\chi &= \frac{2E_{0x}\, E_{0y}\, \sin\delta}{E_{0x}^2 + E_{0y}^2} = \frac{S_2}{S_1} \end{aligned} \tag{C.10}$$

Starting from Equation C.9 it is possible to obtain all states of light polarization and, in particular:

– Linear horizontal polarization:

$$\begin{aligned} S_0 = S_1 = E_{0x}^2 \\ S_2 = S_3 = 0 \end{aligned} \tag{C.11}$$

– Linear vertical polarization:

$$\begin{aligned} S_0 = -S_1 = E_{0y}^2 \\ S_2 = S_3 = 0 \end{aligned} \tag{C.12}$$

– Right circular polarization:

$$\begin{aligned} S_0 = S_3 = 2E_{0x}^2 = 2E_{0y}^2 \\ S_1 = S_2 = 0 \end{aligned} \tag{C.13}$$

– Left circular polarization:

$$\begin{aligned} S_0 = -S_3 = 2E_{0x}^2 = 2E_{0y}^2 \\ S_1 = S_2 = 0 \end{aligned} \tag{C.14}$$

Partially polarized light can be considered as a superposition of unpolarized and

completely polarized light. In this case, the Stokes parameters satisfy the following relation [150]:

$$S_0^2 > S_1^2 + S_2^2 + S_3^2 \tag{C.15}$$

and the polarization degree (ρ) can be defined as [150]:

$$\rho = \frac{I_{pol}}{I_{TOT}} = \frac{\sqrt{S_1^2 + S_2^2 + S_3^2}}{S_0} \tag{C.16}$$

where $0 \leq \rho \leq 1$, while I_{TOT} and I_{pol} are the total intensity and the intensity of the polarized component, respectively.

The Stokes vector can be now written as [149]:

$$\vec{S} = \begin{pmatrix} S_0 \\ S_1 \\ S_2 \\ S_3 \end{pmatrix} = (1-\rho)\begin{pmatrix} S_0 \\ 0 \\ 0 \\ 0 \end{pmatrix} + \rho \begin{pmatrix} S_0 \\ S_1 \\ S_2 \\ S_3 \end{pmatrix} = \begin{pmatrix} 1 \\ S_1/\rho S_0 \\ S_2/\rho S_0 \\ S_3/\rho S_0 \end{pmatrix} \tag{C.17}$$

as a representation of the polarized component of the light.

The Stokes vector defines a point on a surface of a sphere of unit radius: the Poincaré sphere, where (x, y, z)=(S_1,S_2,S_3). We can define also polar coordinates $\rho(\psi,\chi)$ by defining the Stokes's vector as follow:

$$S = \begin{pmatrix} S_0 \\ \cos 2\chi\ \cos 2\psi \\ \cos 2\chi\ \sin 2\psi \\ \sin 2\chi \end{pmatrix}$$

The Poincaré sphere (Figure C.2) is a convenient graphical method to visualize the light polarization: complete right- (left-) handed circular polarization σ_+ (σ_-) is localized on the north (south) pole of the sphere; a linear polarization state is localized on the equator sphere; while elliptically polarized states are represented everywhere else on the sphere surface, as sketched in Figure C.2, and, in case of partially polarized light, in the sphere volume ($\rho < 1$).

In this thesis, the Stokes polarization parameters are measured by an optical retarder followed by a linear polarizer. The retarder rotates at an angular frequency whereas the polarizer is kept fixed, as described in Appendix A. The Ge-on-Si direct gap PL intensity, studied in Chapter 4, is then probed by means of a multichannel detector at each angle θ of the rotating optical element. A Fourier analysis of the peak amplitude modulation (I(θ)) allows us to obtain Stokes parameters *via* the determin-

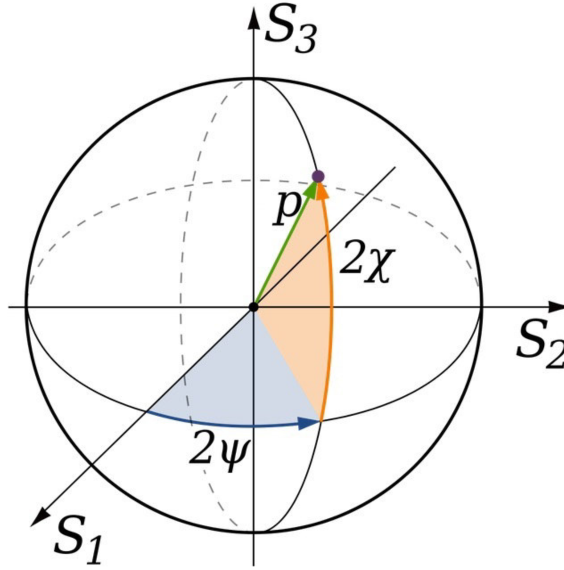

Figure C.2: Poincaré sphere defined by the Stokes parameters (S_1,S_2,S_3). The polar coordinate $\rho(2\psi,2\chi)$ is also shown.

ation of the Fourier coefficients [149, 150]. In particular, the Stokes parameters were found by a least square fit of I(θ) with a function containing the sum of trigonometric functions. The function is defined by:

$$F_{Fit}(\theta) = \frac{1}{2}[A - Bsin(\pi\theta/90) + Ccos(\pi\theta/45) + Dsin(\pi\theta/45)] \tag{C.18}$$

The Stokes parameters are then calculated from the values of F_{Fit} as follows:

$$\begin{aligned} S_0 &= A - C \\ S_1 &= 2C \\ S_2 &= 2D \\ S_3 &= B \end{aligned} \tag{C.19}$$

Moreover, since in our case the PL is always partially polarized, we employed the normalized Stokes parameters described above (Equation C.17) to plot our data through the polarized component of the Poincaré sphere. The modulation intensity as a function of the quarter waveplate angle thus allows us to determine the polarization type of the PL. In particular, the polarization type is defined by the θ position of the maximum intensity (I_{Max}) of the PL peak: a sinusoidal behaviour with period π is the feature of circular polarization (Figure C.3). The phase of the sinusoidal profile ($\pi/4$ or $3\pi/4$) is directly related to the circularly polarized light helicity: if we have I_{Max} at θ = 135°, 315°, the emitted photons helicity is right-handed circularly polarized (σ_+

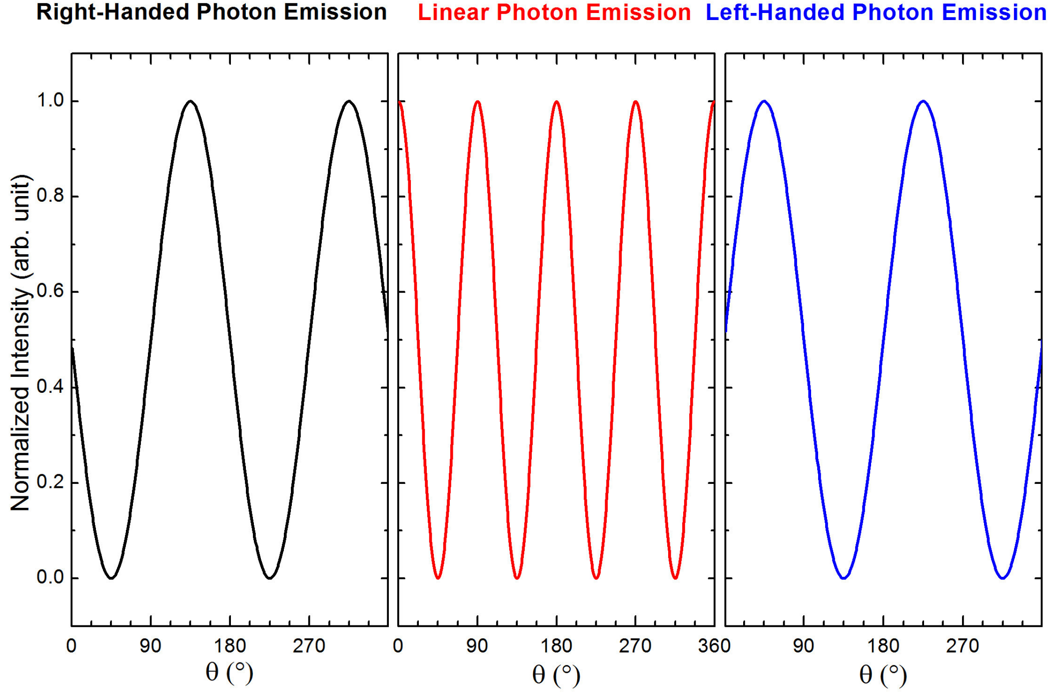

Figure C.3: Intensity modulation as a function of the $\lambda/4$ retarder angle (θ). A phase period of $\pi/2$ stems from circularly polarized light, while a period of $\pi/4$ indicates that helicity of emitted photons is linear.

), while for I_{Max} at θ = 45°, 225°, the emission is left-handed circularly polarized (σ_-). On the other hand, linear polarization is as a superposition of σ_+ and σ_- polarization, and result in a sinusoidal profile with half of the period ($\pi/2$). In this case there are four values of θ for I_{Max} which depend on the linear polarization axis. It is worth noticing that, in the case of σ_+ laser excitation described in this work, I_{Max} at θ = 135° means co-polarized emission, while for I_{Max} at θ = 45° the photon helicity is counter-polarized.

In the measurements presented in Chapter 5, TRPL measurement are performed at fixed wavelength and CWPL signal was probed by means of a single channel detector. As a consequence, the spectra were obtained by acquiring the PL intensity at each wavelength. In these measurements, instead of performing full Stokes's analysis, we utilized a fixed retarder angle θ at 45° and 135°, to measure the intensity of the σ_- and σ_+ PL component, respectively. In this configuration, the polarization degree of the emitted light ρ can be obtained through the classical formula as defined in Chapter 2.4 [66]:

$$\rho = \frac{I_+ - I_-}{I_+ + I_-} \tag{C.20}$$

where I_+ is the peak intensity at θ = 135° and I_- is the peak intensity at θ = 45°. According to Equation C.20, $\rho > 0$ for emission copolarized with respect the σ_+ excitation.

ACKNOWLEDGMENTS

I am very grateful to all the people who shared with me these years and that helped me in writing this work. In particular, I want to spend a special mention for my Supervisor, Dr. Fabio Pezzoli, for his trust on me, for the possibility of growing on the professional as well as on the human side, and for his attention and support in all the aspects of my work. From the very beginning he helped and encouraged me with patience, competence and friendship, taking care of me step by step. I want also to thank my Tutor, Prof. Emanuele Grilli, who provided me an invaluable help both in experimental and physics problems and who has been a great example of hard-working and professionalism.

I thank Sebastiano De Cesari for the many working hours spent side by side, sharing with me joyful and distress times of this years, and for the very nice and pleasant moments we enjoyed outside the university. Thanks also to the other people of the research group: Prof. Mario Guzzi, Prof. Emiliano Bonera, Anna Giorgioni, Michael Barget, Francesco Basso Basset and Eleonora Gatti. This group is renowned for its capability of providing an environment in which students and workers can grow in their professional skills and experience a unique atmosphere of friendship and collaboration. It has been a pleasure to share every working day with them.

All the samples analyzed in this work have been grown at the L-NESS centre of Como by Prof. Giovanni Isella, Jacopo Frigerio and Stefano Cecchi. I thank Anna Giorgioni and Stefano Paleari for the ESR measurements at Milano-Bicocca. I also thank Eleonora Gatti for her help in the PL measurement of Ge on Si samples and for her friendly company at the very beginning of my PhD. I am also grateful to Michele Virgilio of the University of Pisa for tight binding calculations on Ge on Si.

I thank the dean of the PhD course in Science and Nanotechnology of Materials,

Prof. Marco Bernasconi, and Mrs. Maria Cristina Fassina, whose help in bureaucratic business was very precious.

During my PhD I have spent ten months working at the Institut für Halbleiter- und Festkörperphysik of the Johannes Kepler Universität in Linz (Austria), under the supervision of Prof. Armando Rastelli. I sincerely acknowledge him for the very valuable opportunity he has given to me. I would like to thank Javier Martín-Sánchez for sharing with me his knowledge about semiconductor processing in a very friendly and expert way.

I would like to thank all the people I met in Austria. Thanks to Stefano, Giulia, Luciano, Rinaldo, Futura, Giulia and Alessandro for our dinners together, they helped me feeling home in a foreign country.

I thank Donata, who shared with me the university path from the very first day of Bachelor course. I cannot ask to meet a better friend than her, and we've supported each other for so many years that it looks like a lifetime.

I am very grateful to my teammates of CSD, who shared with me plenty of evenings in volley training sessions: even after the hardest working days, it's always pleasant to struggle together and, after that, to share relaxing and funny moments.

I would spend a special thank for all my family and, in particular, for my parents. They always supported me and each of my goals is also their merit.

Last, but actually first, it is impossible to express with few words how grateful I am to Stefano: the pleasure of sharing with him the important steps as well as everyday life is gorgeous and priceless for me.

For all these reasons, my PhD has been one of the most important experiences of my life, from every point of view. Thank you.

Bibliography

[1] V. M. Pereira and A. H. Castro Neto, "Strain engineering of graphene's electronic structure," *Phys. Rev. Lett.*, vol. 103, p. 046801, 2009.

[2] S. Bedell, A. Khakifirooz, and D. Sadana, "Strain scaling for CMOS," *MRS Bulletin*, vol. 39, pp. 131–137, 2 2014.

[3] Y. Sun, T. Nishida, and S. E. Thompson, *Overview: The Age of Strained Devices*, pp. 1–6. Boston, MA: Springer US, 2010.

[4] M. Lee, E. Fitzgerald, M. Bulsara, M. Currie, and A. Lochtefeld, "Strained Si, SiGe, and Ge channels for high-mobility metal-oxide-semiconductor field-effect transistors," *Journal of Applied Physics*, vol. 97, no. 1, 2005.

[5] M. Chu, Y. K. Sun, U. Aghoram, and S. E. Thompson, "Strain: A solution for higher carrier mobility in nanoscale MOSFETs," *Annu. Rev. Mater. Res.*, vol. 39, p. 203, 2009.

[6] J. Liu, R. E. Camacho-Aguilera, J. T. Bessette, X. Sun, X. Wang, Y. Cai, L. C. Kimerling, and J. Michel, "Ge-on-Si optoelectronics," *Thin Solid Films*, vol. 520, p. 3354, 2012.

[7] J. Michel, J. Liu, and L. C. Kimerling, "High-performance Ge-on-Si photodetectors," *Nat. Photonics*, vol. 4, p. 527, 2010.

[8] P. Boucaud, M. Kurdi, S. Sauvage, M. De Kersauson, A. Ghrib, and X. Checoury, "Light emission from strained germanium," *Nature Photonics*, vol. 7, no. 3, p. 162, 2013.

[9] J. Liu, R. E. Camacho-Aguilera, L. C. Kimerling, and J. Michel, "Ge-on-Si laser operating at room temperature," *Opt. Lett.*, vol. 35, p. 679, 2010.

[10] R. Soref and L. Friedman, "Direct-gap Ge/GeSn/Si and GeSn/Ge/Si heterostructures," *Superlattices and Microstructures*, vol. 14, no. 2-3, p. 189, 1993.

[11] J. Liu, X. Sun, D. Pan, X. Wang, L. C. Kimerling, T. L. Koch, and J. Michel, "Tensile-strained, n-type Ge as a gain medium for monolithic laser integration on Si," *Opt. Express*, vol. 15, p. 7114, 2007.

[12] M. El Kurdi, G. Fishman, S. Sauvage, and P. Boucaud, "Band structure and optical gain of tensile-strained germanium based on a 30 band kp formalism," *J. Appl. Phys.*, vol. 107, p. 013710, 2010.

[13] M. Virgilio, C. L. Manganelli, G. Grosso, G. Pizzi, and G. Capellini, "Radiative recombination and optical gain spectra in biaxially strained n-type germanium," *Phys. Rev. B*,

vol. 87, p. 235313, 2013.

[14] M. Schmid, M. Oehme, M. Gollhofer, R. Körner, M. Kaschel, E. Kasper, and J. Schulze, "Effect of heavy doping and strain on the electroluminescence of Ge-on-Si light emitting diodes," *Thin Solid Films*, vol. 557, pp. 351–354, 2014.

[15] B. Schwartz, A. Klossek, M. Kittler, M. Oehme, E. Kasper, and J. Schulze, "Electroluminescence of germanium leds on silicon: Influence of antimony doping," *Physica Status Solidi (C) Current Topics in Solid State Physics*, vol. 11, no. 11-12, pp. 1686–1691, 2014.

[16] M. Oehme, J. Werner, E. Kasper, M. Jutzi, and M. Berroth, "High bandwidth Ge p-i-n photodetector integrated on Si," *Applied Physics Letters*, vol. 89, no. 7, 2006.

[17] T. Arguirov, M. Kittler, M. Oehme, N. Abrosimov, E. Kasper, and J. Schulze, "Room temperature direct band-gap emission from an unstrained Ge p-i-n LED on Si," *Solid State Phenomena*, vol. 178-179, pp. 25–30, 2011.

[18] R. E. Camacho-Aguilera, N. Cai, Y. andl Patel, J. T. Bessette, M. Romagnoli, L. C. Kimerling, and J. Michel, "An electrically pumped germanium laser," *Opt. Express*, vol. 20, p. 11316, 2012.

[19] M. Virgilio, C. L. Manganelli, G. Grosso, G. Pizzi, and G. Capellini, "Radiative recombination and optical gain spectra in biaxially strained n-type germanium," *Phys. Rev. B*, vol. 87, p. 235313, Jun 2013.

[20] S. A. Wolf, D. Awschalom, R. Buhrman, J. Daughton, S. von Molnar, M. Roukes, A. Chtchelkanova, and D. Treger, "Spintronics: A Spin-Based Electronics Vision for the Future," *Science*, vol. 294, p. 1488, 2001.

[21] R. Jansen, "Silicon spintronics," *Nature Materials*, vol. 11, no. 5, pp. 400–408, 2012.

[22] M. I. D'yakonov, *Spin Physics in Semiconductors*. Spinger-Verlag (Berlin), 2004.

[23] I. Zutic, J. Fabian, and S. Das Sarma, "Spintronics: Fundamentals and applications," *Rev. Mod. Phys.*, vol. 76, p. 323, 2004.

[24] A. Sigillito, R. Jock, A. Tyryshkin, J. Beeman, E. Haller, K. Itoh, and S. Lyon, "Electron spin coherence of shallow donors in natural and isotopically enriched germanium," *Physical Review Letters*, vol. 115, no. 24, 2015.

[25] F. Pezzoli, L. Qing, A. Giorgioni, G. Isella, E. Grilli, M. Guzzi, and H. Dery, "Spin and energy relaxation in germanium studied by spin-polarized direct-gap photoluminescence," *Phys. Rev. B*, vol. 88, p. 045204, 2013.

[26] G. W. Ludwig and H. H. Woodbury, *Solid state physics*, vol. 13. Academic Press, New York, 1962.

[27] M. I. D'yakonov and V. I. Perel, *Optical Orientation*. North Holland, Amsterdam, 1984.

[28] P. Li, D. Trivedi, and H. Dery, "Spin-dependent optical properties in strained silicon and germanium," *Phys. Rev. B*, vol. 87, p. 115203, 2013.

[29] L. R. Tessler, C. Hermann, G. Lampel, Y. Lassailly, C. Fontaine, E. Daran, and A. Muñoz Yagüe, "Highly polarized photoluminescence from 2μm thick strained GaAs grown on CaF_2," *Appl. Phys. Lett.*, vol. 64, p. 895, 1994.

[30] Y. Zhou, W. Han, L.-T. Chang, F. Xiu, M. Wang, M. Oehme, I. A. Fischer, J. Schulze, R. K. Kawakami, and K. L. Wang, "Electrical spin injection and transport in germanium," *Phys. Rev. B*, vol. 84, p. 125323, Sep 2011.

[31] M. Bonfanti, E. Grilli, M. Guzzi, M. Virgilio, G. Grosso, D. Chrastina, G. Isella, H. von

Känel, and A. Neels, “Optical transitions in Ge/SiGe multiple quantum wells in Ge-rich barriers,” *Phys. Rev. B*, vol. 78, p. 041407(R), 2008.

[32] C. Lange, N. S. Köster, S. Chatterjee, H. Sigg, D. Chrastina, G. Isella, H. von Känel, M. Schäfer, M. Kira, and S. W. Koch, “Ultrafast nonlinear optical response of photoexcited Ge/SiGe quantum wells: Evidence for a femtosecond transient population inversion,” *Phys. Rev. B*, vol. 79, p. 201306(R), 2009.

[33] E. Vitiello, M. Virgilio, A. Giorgioni, J. Frigerio, E. Gatti, S. De Cesari, E. Bonera, E. Grilli, G. Isella, and F. Pezzoli, “Spin-dependent direct gap emission in tensile-strained Ge films on Si substrates,” *Phys. Rev. B*, vol. 92, p. 201203(R), 2015.

[34] A. Giorgioni, S. Paleari, S. Cecchi, E. Vitiello, E. Grilli, G. Isella, W. Jantsch, M. Fanciulli, and F. Pezzoli, “Strong confinement-induced engineering of the g factor and lifetime of conduction electron spins in Ge quantum wells,” *Nat. Commun.*, vol. 50, no. 8, pp. 5226–5230, 2016.

[35] N. W. Ashcroft and N. D. Mermin, *Solid-State Physics*. Harcourt College Publishers, 1976.

[36] S. M. Sze, *Physics of Semiconductor Devices, 2nd Edition*. Wiley, New York, 1981.

[37] Y. P. Varshni, “Temperature dependence of the energy gap in semiconductors,” *Physica*, vol. 34, p. 149, 1967.

[38] R. K. Schaevitz, D. S. Ly-Gagnon, J. E. Roth, E. H. Edwards, and D. A. B. Miller, “Indirect absorption in germanium quantum wells,” *AIP Advances*, vol. 1, no. 3, p. 032164, 2011.

[39] P. Y. Yu and M. Cardona, *Fundamentals of semiconductors*. Springer, 1996.

[40] L. Liu, “Effects of spin-orbit coupling in Si and Ge,” *Phys. Rev.*, vol. 126, p. 1317, 1962.

[41] J. I. Pankove, *Optical processes in semiconductors*. Nick Holonyak Jr., 1971.

[42] A. Giorgioni, E. Vitiello, E. Grilli, M. Guzzi, and F. Pezzoli, “Valley-dependent spin polarization and long-lived electron spins in germanium,” *Appl. Phys. Lett.*, vol. 105, p. 152404, 2014.

[43] F. Wooten, *Optical Properties of solids*. Academic Press, New York, 1972.

[44] G. Mak and H. M. Van Driel, “Femtosecond transmission spectroscopy at the direct band-edge of germanium,” *Phys. Rev. B*, vol. 49, no. 23, pp. 16817–16820, 1994.

[45] X. Q. Zhou, H. M. Van Driel, and G. Mak, “Femtosecond kinetics of photoexcited carriers in germanium,” *Phys. Rev. B*, vol. 50, no. 8, pp. 5226–5230, 1994.

[46] R. R. Lieten, K. Bustillo, T. Smets, E. Simoen, J. W. Ager III, E. E. Haller, and J.-P. Locquet, “Photoluminescence of bulk germanium,” *Phys. Rev. B*, vol. 86, p. 035204, 2012.

[47] M. B. Prince, “Drift Mobilities in Semiconductors. I. Germanium,” *Phys. Rev.*, vol. 92, pp. 681–687, Nov 1953.

[48] L. Pavesi and M. Guzzi, “Photoluminescence of $Al_xGa_{1-x}As$ alloys,” *J. Appl. Phys.*, vol. 75, p. 4779, 1994.

[49] P. Li, Y. Song, and H. Dery, “Intrinsic spin lifetime of conduction electrons in germanium,” *Phys. Rev. B*, vol. 86, p. 085202, 2012.

[50] R. J. Elliott, “Theory of the effect of spin-orbit coupling on magnetic resonance in some semiconductors,” *Phys. Rev.*, vol. 96, pp. 266–279, 1954.

[51] Y. Yafet, *Solid state physics*, vol. 14. Academic Press, New York, 1963.

[52] M. I. D'yakonov and V. I. Perel, "Spin relaxation of conduction electrons in non centrosymetric semiconductors," *Sov. Phys. Solid State*, vol. 13, pp. 3023–3026, 1971.

[53] G. L. Bir, A. G. Aronov, and G. E. Pikus, "Spin relaxation of electrons due to scattering by holes," *Sov. Phys. JETP*, vol. 42, pp. 705–712, 1976.

[54] M. I. D'yakonov and V. I. Perel, "Optical orientation in a system of electrons and lattice nuclei in semiconductors: Theory," *Sov. Phys. JETP*, vol. 38, pp. 177–183, 1973.

[55] J.-M. Tang, B. T. Collins, and M. E. Flatté, "Electron spin-phonon interaction symmetries and tunable spin relaxation in silicon and germanium," *Phys. Rev. B*, vol. 85, p. 045202, 2012.

[56] A. Jain, J.-C. Rojas-Sanchez, M. Cubukcu, J. Peiro, J. C. Le Breton, E. Prestat, C. Vergnaud, L. Louahadj, C. Portemont, C. Ducruet, V. Baltz, A. Barski, P. Bayle-Guillemaud, L. Vila, J.-P. Attané, E. Augendre, G. Desfonds, S. Gambarelli, H. Jaffrès, J.-M. George, and M. Jamet, "Crossover from spin accumulation into interface states to spin injection in the germanium conduction band," *Phys. Rev. Lett.*, vol. 109, p. 106603, Sep 2012.

[57] K. Hamaya, Y. Baba, G. Takemoto, K. Kasahara, S. Yamada, K. Sawano, and M. Miyao, "Qualitative study of temperature-dependent spin signals in n-Ge-based lateral devices with Fe_3Si/n^+-Ge Schottky-tunnel contacts," *J. Appl. Phys.*, vol. 113, no. 18, p. 183713, 2013.

[58] A. Jain, L. Louahadj, J. Peiro, J. C. L. Breton, C. Vergnaud, A. Barski, C. Beigné, L. Notin, A. Marty, V. Baltz, S. Auffret, E. Augendre, H. Jaffrés, J. M. George, and M. Jamet, "Electrical spin injection and detection at Al_2O_3/n-type germanium interface using three terminal geometry," *Appl. Phys. Lett.*, vol. 99, no. 16, p. 162102, 2011.

[59] P. Li, J. Li, L. Qing, H. Dery, and I. Appelbaum, "Anisotropy-driven spin relaxation in germanium," *Phys. Rev. Lett.*, vol. 111, p. 257204, Dec 2013.

[60] C. Guite and V. Venkataraman, "Temperature dependence of spin lifetime of conduction electrons in bulk germanium," *Applied Physics Letters*, vol. 101, no. 25, p. 252404, 2012.

[61] J. Lohrenz, T. Paschen, and M. Betz, "Resonant spin amplification in intrinsic bulk germanium. Evidence for electron spin lifetime exceeding 50 ns," *Phys. Rev. B*, vol. 89, p. 121201(R), 2014.

[62] L. M. Roth and B. Lax, "g factor of electrons in germanium," *Phys. Rev. Lett.*, vol. 3, p. 217, 1959.

[63] D. J. Paul, "Si/SiGe heterostructures: from material and physics to devices and circuits," *Semicnd. Sci. Technol.*, vol. 19, p. R75, 2004.

[64] G. Grzybowski, R. Roucka, J. Mathews, L. Jiang, R. T. Beeler, J. Kouvetakis, and J. Menendez, "Direct versus indirect optical recombination in Ge films grown on Si substrates," *Phys. Rev. B*, vol. 84, p. 205307, 2011.

[65] E. Hecht, *Optics*. Addison-Wesley, 2002.

[66] M. Fox, *Optical properties of solids*. Oxford University Press, 2010.

[67] E. J. Loren, J. Rioux, C. Lange, J. E. Sipe, H. M. van Driel, and A. L. Smirl, "Hole spin relaxation and intervalley electron scattering in germanium," *Phys. Rev. B*, vol. 84, p. 214307, 2011.

[68] P. Li and H. Dery, "Theory of spin-dependent phonon-assisted optical transitions in sil-

icon," *Phys. Rev. Lett.*, vol. 105, p. 037204, 2010.

[69] L. C. Lew Yan Voon and M. Willatzen, *The kp method*. Spinger, 2009.

[70] Y. Ishikawa, K. Wada, J. Liu, D. D. Cannon, H. Luan, and L. C. Michel, J. andi Kimerling, "Strain-induced enhancement of near-infrared absorption in Ge epitaxial layers grown on Si substrate," *J. Appl. Phys.*, vol. 98, p. 013501, 2005.

[71] C. G. Van de Walle, "Band lineups and deformation potentials in the model-solid theory," *Phys. Rev. B*, vol. 39, p. 1871, 1989.

[72] D. Liang and J. Bowers, "Recent progress in lasers on silicon," *Nature Photonics*, vol. 4, no. 8, pp. 511–517, 2010.

[73] Z. Zhou, B. Yin, and J. Michel, "On-chip light sources for silicon photonics," *Light: Science and Applications*, vol. 4, no. 11, 2015.

[74] R. Soref, "The past, present, and future of silicon photonics," *IEEE Journal on Selected Topics in Quantum Electronics*, vol. 12, no. 6, pp. 1678–1687, 2006.

[75] Z. Liu, W. Hu, C. Li, Y. Li, C. Xue, C. Li, Y. Zuo, B. Cheng, and Q. Wang, "Room temperature direct-bandgap electroluminescence from n-type strain-compensated Ge/SiGe multiple quantum wells," *Applied Physics Letters*, vol. 101, no. 23, 2012.

[76] J. Jain, A. Hryciw, T. Baer, D. Miller, M. Brongersma, and R. Howe, "A micromachining-based technology for enhancing germanium light emission via tensile strain," *Nature Photonics*, vol. 6, no. 6, pp. 398–405, 2012. cited By 99.

[77] T.-H. Cheng, K.-L. Peng, C.-Y. Ko, C.-Y. Chen, H.-S. Lan, Y.-R. Wu, C. W. Liu, and H.-H. Tseng, "Strain-enhanced photoluminescence from Ge direct transition," *Appl. Phys. Lett.*, vol. 96, p. 211108, 2010.

[78] X. Sun, J. Liu, L. C. Kimerling, and J. Michel, "Direct gap photoluminescence of n-type tensile-strained Ge-on-Si," *Appl. Phys. Lett.*, vol. 95, p. 011911, 2009.

[79] J. Liu, X. Sun, L. Kimerling, and J. Michel, "Direct-gap optical gain of Ge on Si at room temperature," *Optics Letters*, vol. 34, no. 11, pp. 1738–1740, 2009.

[80] R. Soref, "Group IV photonics: Enabling 2 μm communications," *Nature Photonics*, vol. 9, no. 6, pp. 358–359, 2015.

[81] S. De Cesari, E. Vitiello, A. Giorgioni, and F. Pezzoli, "Progress towards spin-based light emission in group iv semiconductors," *Electronics*, vol. 6, no. 19, 2017.

[82] Y. Huo, H. Lin, R. Chen, M. Makarova, Y. Rong, M. Li, T. Kamins, J. Vuckovic, and J. Harris, "Strong enhancement of direct transition photoluminescence with highly tensile-strained Ge grown by molecular beam epitaxy," *Applied Physics Letters*, vol. 98, no. 1, 2011.

[83] R. Jakomin, M. De Kersauson, M. El Kurdi, L. Largeau, O. Mauguin, G. Beaudoin, S. Sauvage, R. Ossikovski, G. Ndong, M. Chaigneau, I. Sagnes, and P. Boucaud, "High quality tensile-strained n -doped germanium thin films grown on InGaAs buffer layers by metal-organic chemical vapor deposition," *Applied Physics Letters*, vol. 98, no. 9, 2011.

[84] G. Capellini, C. Reich, S. Guha, Y. Yamamoto, M. Lisker, M. Virgilio, A. Ghrib, M. El Kurdi, P. Boucaud, B. Tillack, and T. Schroeder, "Tensile Ge microstructures for lasing fabricated by means of a silicon complementary metal-oxide-semiconductor process," *Optics Express*, vol. 22, no. 1, pp. 399–410, 2014.

[85] A. Ghrib, M. El Kurdi, M. Prost, S. Sauvage, X. Checoury, G. Beaudoin, M. Chaigneau,

R. Ossikovski, I. Sagnes, and P. Boucaud, "All-around SiN stressor for high and homogeneous tensile strain in germanium microdisk cavities," *Advanced Optical Materials*, vol. 3, no. 3, pp. 353–358, 2015.

[86] M. El Kurdi, M. Prost, A. Ghrib, S. Sauvage, X. Checoury, G. Beaudoin, I. Sagnes, G. Picardi, R. Ossikovski, and P. Boucaud, "Direct band gap germanium microdisks obtained with silicon nitride stressor layers," *ACS Photonics*, vol. 3, no. 3, pp. 443–448, 2016.

[87] D. Nam, D. Sukhdeo, A. Roy, K. Balram, S.-L. Cheng, K.-Y. Huang, Z. Yuan, M. Brongersma, Y. Nishi, D. Miller, and K. Saraswat, "Strained germanium thin film membrane on silicon substrate for optoelectronics," *Optics Express*, vol. 19, no. 27, pp. 25866–25872, 2011.

[88] D. Nam, D. Sukhdeo, S.-L. Cheng, A. Roy, K. Chih-Yao Huang, M. Brongersma, Y. Nishi, and K. Saraswat, "Electroluminescence from strained germanium membranes and implications for an efficient Si-compatible laser," *Applied Physics Letters*, vol. 100, no. 13, 2012.

[89] M. Bollani, D. Chrastina, L. Gagliano, L. Rossetto, D. Scopece, M. Barget, V. Mondiali, J. Frigerio, M. Lodari, F. Pezzoli, F. Montalenti, and E. Bonera, "Local uniaxial tensile strain in germanium of up to 4% induced by SiGe epitaxial nanostructures," *Applied Physics Letters*, vol. 107, no. 8, 2015.

[90] M. Süess, R. Geiger, R. Minamisawa, G. Schiefler, J. Frigerio, D. Chrastina, G. Isella, R. Spolenak, J. Faist, and H. Sigg, "Analysis of enhanced light emission from highly strained germanium microbridges," *Nature Photonics*, vol. 7, no. 6, pp. 466–472, 2013.

[91] M. El Kurdi, H. Bertin, M. De Kersauson, G. Fishman, S. Sauvage, A. Bosseboeuf, and P. Boucaud, "Control of direct band gap emission of bulk germanium by mechanical tensile strain," *Appl. Phys. Lett.*, vol. 96, p. 041909, 2010.

[92] C. Boztug, J. R. Sánchez-Peréz, F. Cavallo, M. G. Lagally, and R. Paiella, "Strained-Germanium Nanostructures for Infrared Photonics," *ACS Nano*, vol. 8, p. 3136, 2014.

[93] C. Boztug, J. Sánchez-Pérez, F. Sudradjat, R. Jacobson, D. Paskiewicz, M. Lagally, and R. Paiella, "Tensilely strained germanium nanomembranes as infrared optical gain media," *Small*, vol. 9, no. 4, pp. 622–630, 2013.

[94] K. Brunner, "Si/Ge nanostructures," *Rep. Prog. Phys.*, vol. 65, p. 27, 2002.

[95] R. People and J. C. Bean, "Calculation of critical layer thickness versus lattice mismatch for GeSi/Si strained-layer heterostructure," *Appl. Phys. Lett.*, vol. 47, p. 322, 1985.

[96] J. Matthews and A. Blakeslee, "Defects in epitaxial multilayers: I. misfit dislocations," *Journal of Crystal Growth*, vol. 27, no. Supplement C, pp. 118 – 125, 1974.

[97] J. H. van der Merwe, "Structure of epitaxial crystal interfaces," *Surf. Science*, vol. 31, p. 198, 1972.

[98] L. D. Landau and E. M. Lifshitz, *Theory of elasticity, 3rd edition*, vol. 7. Oxford University Press, 1986.

[99] J. Hirth and J. Lothe, *Theory of Dislocations*. Mc Graw-Hill, New York, 1982.

[100] R. Hull and J. C. Bean, *Germanium Silicon: Physics and Materials*. Academic Press, New York, 1998.

[101] G. A. Slack and S. F. Bartram, "Termal expansion of some diamondlike crystals," *J. Appl. Phys.*, vol. 46, p. 89, 1975.

[102] H. P. Singh, “Determination of thermal expansion of germanium, rhodium and iridium by x-rays,” *Acta Crystallogr.*, vol. 24, p. 469, 1968.

[103] M. Fischetti and S. Laux, “Band structure, deformation potentials, and carrier mobility in strained Si Ge, and SiGe alloys,” *Journal of Applied Physics*, vol. 80, no. 4, pp. 2234–2252, 1996.

[104] F. Zhang, V. Crespi, and P. Zhang, “Prediction that uniaxial tension along (111) produces a direct band gap in germanium,” *Physical Review Letters*, vol. 102, no. 15, 2009.

[105] M. El Kurdi, G. Fishman, S. Sauvage, and P. Boucaud, “Band structure and optical gain of tensile-strained germanium based on a 30 band kp formalism,” *Journal of Applied Physics*, vol. 107, no. 1, 2010.

[106] G. Pizzi, M. Virgilio, and G. Grosso, “Tight-binding calculation of optical gain in tensile strained (001)-Ge/SiGe quantum wells,” *Nanotechnology*, vol. 21, no. 5, 2010.

[107] H.-S. Lan, S.-T. Chan, T.-H. Cheng, C.-Y. Chen, S.-R. Jan, and C. W. Liu, “Biaxial tensile strain effects on photoluminescence of different orientated Ge wafers,” *Appl. Phys. Lett.*, vol. 98, p. 101106, 2011.

[108] M. Virgilio and G. Grosso, “Optical spin orientation in strained Ge/SiGe quantum wells: A tight-binding approach,” *Phys. Rev. B*, vol. 80, p. 205309, Nov 2009.

[109] F. Pezzoli, F. Bottegoni, D. Trivedi, F. Ciccacci, A. Giorgioni, P. Li, S. Cecchi, E. Grilli, Y. Song, M. Guzzi, H. Dery, and G. Isella, “Optical spin injection and spin lifetime in Ge heterostructure,” *Phys. Rev. Lett.*, vol. 108, p. 156603, 2012.

[110] C. Lange, G. Isella, D. Chrastina, F. Pezzoli, N. S. Koester, R. Woscholski, and S. Chatterjee, “Spin band-gap renormalization and hole spin dynamics in Ge/SiGe quantum wells,” *Phys. Rev. B*, vol. 85, p. 241303(R), 2012.

[111] A. Giorgioni, F. Pezzoli, E. Gatti, S. Cecchi, C. K. Inoki, C. Deneke, E. Grilli, G. Isella, and M. Guzzi, “Optical tailoring of carrier spin polarization in Ge/SiGe multiple quantum wells,” *Appl. Phys. Lett.*, vol. 102, p. 012408, 2013.

[112] J. Christen, D. Bimberg, A. Steckenborn, and G. Weimann, “Localization induced electron-transition rate enhancement in GaAs quantum wells,” *Appl. Phys. Lett.*, vol. 44, p. 88, 1984.

[113] Y.-H. Kuo, Y. K. Lee, Y. Ge, S. Ren, J. E. Roth, T. I. Kamins, D. A. B. Miller, and J. S. Harris, “Strong quantum-confined stark effect in germanium quantum-well structures on silicon,” *Nature*, vol. 437, p. 1334, 2005.

[114] A. Giorgioni, E. Gatti, E. Grilli, A. Chernikov, S. Chatterjee, D. Chrastina, G. Isella, and M. Guzzi, “Photoluminescence decay of direct and indirect transitions in Ge/SiGe multiple quantum wells,” *Journal of Applied Physics*, vol. 111, no. 1, p. 013501, 2012.

[115] J. Weber and M. Alonso, “Near-band-gap photoluminescence of SiGe alloys,” *Phys. Rev. B*, vol. 40, p. 5683, 1989.

[116] A. R. Denton and N. W. Ashcroft, “Vegard’s Law,” *Phys. Rev. A*, vol. 43, p. 3161, 1991.

[117] M. Virgilio and G. Grosso, “Type-I alignment and direct fundamental gap in sige based heterostructures,” *Journal of Physics: Condensed Matter*, vol. 18, no. 3, p. 1021, 2006.

[118] R. Ferreira and G. Bastard, “Spin-flip scattering of holes in semiconductor quantum wells,” *Phys. Rev. B*, vol. 43, pp. 9687–9691, 1991.

[119] M. Kummer, C. Rosenblad, A. Domman, T. Hackbarth, G. Hock, M. Zeuner, E. Muller,

and H. von Känel, “Low energy plasma enhanced chemical vapor deposition,” *Mat. Sci. Eng. B*, vol. 89, p. 288, 2002.

[120] F. Pezzoli, E. Grilli, M. Guzzi, S. Sanguinetti, D. Chrastina, G. Isella, H. von Känel, E. Wintersberger, J. Stangl, and G. Bauer, “Strain-induced shift of phonon modes in SiGe alloys,” *Mat. Sci. Semicon. Proc.*, vol. 9, p. 541, 2006.

[121] S. A. Shevchenko and A. N. Tereshchenko, “Photoluminescence in germanium with a quasi-equilibrium dislocation structure,” *Physics of the Solid State*, vol. 49, no. 1, pp. 28–33, 2007.

[122] T. Arguirov, O. Vyvenko, M. Oehme, J. Schulze, and M. Kittler, “Dislocation luminescence in highly doped degenerated germanium at room temperature,” *Physica Status Solidi C*, vol. 10, no. 1, p. 56, 2013.

[123] E. Loren, B. Ruzicka, L. Werake, H. Zhao, H. Van Driel, and A. Smirl, “Optical injection and detection of ballistic pure spin currents in Ge,” *Applied Physics Letters*, vol. 95, no. 9, 2009.

[124] F. Pezzoli, A. Giorgioni, K. Gallacher, F. Isa, P. Biagioni, R. W. Millar, E. Gatti, E. Grilli, E. Bonera, G. Isella, D. J. Paul, and L. Miglio, “Disentangling nonradiative recombination processes in Ge micro-crystals on Si substrates,” *Applied Physics Letters*, vol. 108, no. 26, p. 262103, 2016.

[125] J.-M. Jancu and P. Voisin, “Tetragonal and trigonal deformations in zinc-blende semiconductors: A tight-binding point of view,” *Phys. Rev. B*, vol. 76, p. 115202, 2007.

[126] F. Pezzoli, A. Balocchi, E. Vitiello, T. Amand, and X. Marie, “Optical orientation of electron spins and valence-band spectroscopy in germanium,” *Phys. Rev. B*, vol. 91, p. 201201, May 2015.

[127] C. Jain and D. J. Roulston, “A simple expression for band gap narrowing (BGN) in heavily doped Si, Ge GaAs and GeSi strained layers,” *Solid State Electron.*, vol. 34, p. 453, 1991.

[128] T. R. Harris, Y. K. Yeo, M.-Y. Ryu, R. T. Beeler, and J. Kouvetakis, “Observation of heavy- and light-hole split direct bandgap photoluminescence from tensile-strained GeSn (0.03% Sn),” *J. Appl. Phys.*, vol. 116, p. 103502, 2014.

[129] S. Marchionna, A. Virtuani, M. Acciarri, G. Isella, and H. von Känel, “Defect imaging of SiGe strain relaxed buffers grown by lepecvd,” *Materials Science in Semiconductor Processing*, vol. 9, no. 4, p. 802, 2006. Proceedings of Symposium T E-MRS 2006 Spring Meeting on Germanium based semiconductors from materials to devices.

[130] E. A. Fitzgerarld, Y.-H. Xie, M. L. Green, D. Brasen, A. R. Kortan, J. Michel, Y.-J. Mii, and B. E. Weir, “Totally relaxed Ge_xSi_{1-x} layers with low threading dislocation densities grown on Si substrates,” *Appl. Phys. Lett.*, vol. 59, p. 811, 1991.

[131] D. K. Wilson, “Electron spin resonance experiments on shallow donors in germanium,” *Phys. Rev.*, vol. 134, pp. A265–A286, Apr 1964.

[132] G. L. Pearson and J. Bardeen, “Electrical properties of pure silicon and silicon alloys containing boron and phosphorus,” *Phys. Rev.*, vol. 75, pp. 865–883, Mar 1949.

[133] F. Schäffler, “High-mobility Si and Ge structures,” *Semicond. Sci. Technol.*, vol. 12, p. 1515, 1997.

[134] Y.-H. Kuo, Y. Ge, S. Ren, E. Roth, T. Kamins, D. A. B. Miller, and J. S. Harris, “Quantum-confined stark effect in Ge/SiGe quantum wells on Si for optical modulators,” *IEEE Journal of Selected Topics in Quantum Electronics*, vol. 12, p. 1503, 2006.

[135] V. Härle, H. Bolay, E. Lux, P. Michler, A. Moritz, T. Forner, A. Hangleiter, and F. Scholz, "Indirect-bandgap transition in strained GaInAs/InP quantum well structures," *J. Appl. Phys*, vol. 75, p. 5067, 1994.

[136] S. Fukatsu, H. Akiyama, Y. Shiraki, and K. Sakaki, "Quantitative analysis of light emission from SiGe quantum wells," *J. Cryst. Growth*, vol. 1, p. 157, 1995.

[137] C. Hu, Y. H., G. Wang, H. Tian, W. Wang, W. Wang, B. Liu, and X. Marie, "Room temperature spin diffusion in (110) GaAs/AlGaAs quantum wells," *Nanoscale Res. Lett.*, vol. 6, p. 149, 2011.

[138] Y. Ohno, R. Terauchi, T. Adachi, F. Matsukura, and H. Ohno, "Spin relaxation in GaAs(110) quantum wells," *Phys. Rev. Lett.*, vol. 20, p. 4196, 1999.

[139] C. Hautmann and M. Betz, "Magneto-optical analysis of the effective g tensor and electron spin decoherence in the multivalley conduction band of bulk germanium," *Phys. Rev. B*, vol. 85, p. 121203, Mar 2012.

[140] C. P. J. Poole, *Electron Spin Resonance: a comprehensive treatise on experimental technique*. Dover Pubblications, 1996.

[141] Y. Song, O. Chalaev, and H. Dery, "Donor-driven spin relaxation in multivalley semiconductors," *Phys. Rev. Lett.*, vol. 113, p. 167201, Oct 2014.

[142] L. Qing, J. Li, I. Appelbaum, and H. Dery, "Spin relaxation via exchange with donor impurity-bound electrons," *Phys. Rev. B*, vol. 91, p. 241405, Jun 2015.

[143] F. A. Baron, A. A. Kiselev, H. D. Robinson, K. W. Kim, K. L. Wang, and E. Yablonovitch, "Manupilating the L-valley electron g factor in SiGe heterostructures," *Phys. Rev. B*, vol. 68, p. 195306, 2003.

[144] M. Waldrop, "More than Moore," *Nature*, vol. 530, no. 7589, pp. 144–147, 2016.

[145] M. Oestreich, J. Hubner, D. Hagele, M. Bender, N. Gerhardt, M. Hofmann, W. Ruhle, H. Kalt, T. Hartmann, and P. Klar, "Spintronics: Spin electronics and optoelectronics in semiconductors," *Adv. Solid State Phys*, vol. 41, pp. 173–186, 2001.

[146] Hamamatsu, "http://www.hamamatsu.com."

[147] Z. Wilamowski and W. Jantsch, "Suppression of spin relaxation of conduction electron by cyclotron motion," *Phys. Rev. B*, vol. 69, p. 035328, 2004.

[148] L-NESS, "http://lness.como.polimi.it/lepecvd.php."

[149] E. Collett, *Field guide to polarization*. SPIE Press, 2005.

[150] D. H. Goldstein, *Polarized light*. CRC Press, 2010.